Mechanics of Cancer Cells in 3D Microenvironments

by

Jack Rory Staunton

A Dissertation Presented in Partial Fulfillment
of the Requirements for the Degree
Doctor of Philosophy

Approved December 2014 by the
Graduate Supervisory Committee

Robert Ros, Chair
Stuart Lindsay
Paul Davies
Sara Vaiana

ARIZONA STATE UNIVERSITY

December 2014

ABSTRACT

Mechanical properties (e.g. deformability or stiffness) are critical to a cancer cell's ability to maneuver through and exert forces upon the extracellular matrix, and thus affect its ability to metastasize. §3.1 introduces the experimental method combining atomic force microscope (AFM) based indentation and confocal laser scanning microscopy (CLSM). §3.2 presents a method combining AFM and confocal microscopy (AFM stiffness nanotomography), and results on normal and pre-cancerous esophageal cells which indicate that even in the earliest stages, cancer cells exhibit increased deformability. §3.3 presents experimental results on weakly metastatic breast cancer cells that compare well with values obtained from other experimental methods and demonstrates that the mechanical response of cells to sharp and mesoscale probes differ significantly. §3.4 presents experimental results indicating that metastatic breast cancer cells are more deformable than normal counterparts, and demonstrates that indentation measurements with sharp probes are capable of identifying mechanical differences between cytoplasmic, nuclear and nucleolar regions of the cell. §3.5 presents results on weakly metastatic breast cancer cells sensitive and resistant to tamoxifen (an estrogen antagonist), and demonstrate that estrogen has a significant effect on cell stiffness. §3.6 applies stiffness nanotomography to study metastatic breast cancer cells allowed to invade 3D collagen gels, demonstrating the ability to use AFM indentation on heterogeneous samples, and shows that cell stiffness increases during the invasion process for partially and fully embedded metastatic breast cancer cells.

Dedicated to my sister, mom, and dad.

ACKNOWLEDGMENTS

This work would never have been done without help from many co-workers, collaborators, and colleagues. My sincere thanks go foremost to my advisor, Robert Ros for his kindness and patience, and to Bryant Doss who diligently worked with me every step of the way; and also to Alexander Fuhrmann and Olaf Schulz who very helpfully got me started in the lab; to Nathan Banyai and Vivek Nandakumar for their work on the Barrett's cells; especially to Nethmi Ariyasinghe, Mark Linhart, Elizabeth Meyer, and Patti Senechal-Willis for the too-often thankless task of culturing cells; to Bill Grady and Shelli Morris for hands-on training; to Tim Newman, Stuart Lindsay, and Paul Davies for giving me so many opportunities to participate in workshops, meetings and conferences; to Otto Sankey and the Center for Biological Physics for nominating me for the GAANN fellowship; to Jerry Lee, Nas Kuhn and Nicole Moore for their mentorship; and to so many more. This work was funded primarily through ASU Physical Sciences – Oncology Center grant U54CA143862.

TABLE OF CONTENTS

Page

LIST OF TABLES vii

LIST OF FIGURES viii

LIST OF SYMBOLS / NOMENCLATURE xi

CHAPTER

1 INTRODUCTION 1

1.1 Overview 1

1.2 Organization 3

2 BACKGROUND 5

2.1 Cancer 5

2.2 Cell Mechanobiology 8

2.2.1 The Eukaryotic Cytoskeleton 8

2.2.2 The Extracellular Matrix 20

2.2.3 Mechanotransduction 25

2.3 Cell Mechanics Measurement Techniques 37

2.4 Atomic Force Microscope Based Indentation 46

2.4.1 Principles of Atomic Force Microscopy 47

2.4.2 Indentation Force-Depth Curves 51

2.4.3 Elastic Contact Models 53

2.4.4 Modeling with Finite Element Simulation 57

2.4.5 Confocal Microscopy and Fluorescence Lifetime Imaging 58

CHAPTER Page

3 RESULTS AND DISCUSSION 60

3.1 Combined AFM-CLSM Measurements 60

3.2 AFM Stiffness Nanotomography Study of EPC2, CPA, and CPD Cells 63

3.2.1 Contributions 63

3.2.2 Overview 63

3.2.3 Results 64

3.2.4 Conclusions 78

3.2.5 Materials and Methods 80

3.3 AFM Nanoindentation Study of MDA-MB-231 and MCF-10A Cells 84

3.3.1 Contributions 84

3.3.2 Overview 84

3.3.3 Results 84

3.3.4 Conclusions 86

3.3.5 Materials and Methods 87

3.4 AFM Indentation Study of MCF7 Cells 89

3.4.1 Contributions 89

3.4.2 Overview 89

3.4.3 Results 90

3.4.4 Conclusions 91

3.4.5 Materials and Methods 91

3.5 AFM Indentation Study of MCF7-B7 and MCF7-G11 Cells 94

CHAPTER Page

3.5.1 Contributions 94

3.5.2 Overview 94

3.5.3 Results 96

3.5.4 Discussion and Conclusions 111

3.5.5 Materials and Methods 117

3.6 MDA-MB-231 Cells in 3D Collagen Matrices 121

3.5.1 Contributions 121

3.5.2 Overview 121

3.5.3 Results 123

3.5.4 Conclusions 138

3.5.5 Materials and Methods 139

4 OUTLOOK 144

REFERENCES 146

APPENDIX

A DETAILED PROTOCOL FOR INDENTATION OF CELLS IN COLLAGEN 164

B MICROARRAY DATA TABLES 192

LIST OF TABLES

Table Page

3.1. Kernel Smoothing Density Estimates of Modal Young's Moduli and Distribution Full Widths at Half Maxima....69

3.2. Young's Moduli of MCF7 Cells....91

3.3. Young's Moduli of MCF7-B7 and MCF-G11 Cells with and without Estrogen and Tamoxifen....105

3.4. Differential Regulation of Genes of Interest in Tamoxifen Resistant Cells....106

3.5. Collagen Pore Size, Pore Area, and Areal Porosity....127

3.6. Young's Moduli of MDA-MB-231 Cells Partially Embedded in Collagen I Matrices, by Pericellular Collagen Stiffness and Degree of Embedding, with and without ROCK Inhibition....133

.

LIST OF FIGURES

Figure Page

2.1. Causes of Death in Cancer Patients 9

2.2. Web of Science Bibliometric Data 38

2.3. Anatomy of an Indentation Force-Depth Curve 52

2.4. Indenter Geomtery 54

3.1. Experimental AFM-CLSM Setup 60

3.2. Alignment of AFM Tip in Laser Focus. 61

3.3. Spatially Co-registered Indentation Force-Depth Curves. 62

3.4. Adherent Dysplastic CP-D Esophageal Cell Analyzed with Combined Fluorescence Lifetime Imaging and AFM-based Nanoindentation 65

3.5. Distributions of Young's Moduli of EPC2, CP-A, and CP-D Esophageal Cell Nuclei 67

3.6. Histograms and Kernel Smoothing Density Estimate of Unstained EPC2 Cells 68

3.7. 3D Elasticity Maps and Corresponding Elastic Tomograms of CP-A and CP-D Cells 70

3.8. 2D Elasticity Histograms of Young's Modulus vs. Indentation Depth 72

3.9. Nanoscale Cytoskeletal Instability Quantified by Frequency of Incidence of Breakthrough Events 76

3.10. Kernel Smoothing Density Estimates of Total Breakthrough Forces ... 78

3.11. Histograms of Total Indentation Depth 85

Figure Page

3.12. Young's Moduli (Mean ± Standard Error) of MCF-10A and MDA-MB-231 Cells as a Function of Indentation Depth in Different Subcellular Regions 86

3.13. Young's Moduli of MCF7 Cells 90

3.14. Experimental Design 97

3.15. Fluorescence Lifetime Intensity Micrographs 99

3.16. Phase Contrast Micrographs 99

3.17. Young's Moduli of MCF7-B7 and MCF7-G11 Cells with and without Estrogen and Tamoxifen 101

3.18. Histograms of Young's Moduli of MCF7-B7 and MCF7-G11 Cells with and without Estrogen and Tamoxifen 102

3.19. 2D Histograms of Young's Modulus vs. Indentation Depth of MCF7-B7 and MCF7-G11 Cells with and without Estrogen and Tamoxifen 103

3.20. Combined AFM Indentation and Confocal Fluorescence Microscopy for Elasticity Measurements on Embedded Cells 122

3.21. Scanning Electron Microscope Image of an LRCH-750 Tip (Team Nanotec) 124

3.22. Histograms of Young's Moduli of Pericellular Collagen from Hydrogels Formed at Different Initial Collagen Concentrations 125

3.23. Collagen Pore Size Distribution 126

3.24. Confocal Fluorescence Lifetime Images with Superposed Elasticity Tomograms 128

Figure Page

3.25. Young's Moduli of Cells on Glass and Partially Embedded in Collagen, Binned According to Underlying Collagen Stiffness....129

3.26. Young's Moduli of MDA-MB-231 Cells on Glass and Partially Embedded in Collagen I Hydrogels....131

3.27. Finite Element Simulations of Partially Embedded Spheres....134

3.28 MDA-MB-231 Cell Fully Embedded in Collagen I Matrix....135

3.29. Determining the Young's Modulus of a Fully Embedded Cell by Finite Element Simulation....135

3.30. Mechanical Contrast....136

3.31. Young's Moduli of Fully Embedded Cells in Collagen....138

LIST OF SYMBOLS

Symbol Page

1. DNA: Deoxyribonucleic Acid 1
2. 3D: Three-dimensional 2
3. CIS: Carcinoma *in situ* 8
4. NE: Nuclear Envelope 10
5. INM: Inner Nuclear Membrane 11
6. ONM: Outer Nuclear Membrane 11
7. NPC: Nuclear Pore Complex 11
8. IF: Intermediate Filament 11
9. LINC: Linker of Nucleus and Cytoskeleton 11
10. MT: Microtubule 11
11. MPA: Micropipette Aspiration 12
12. AFM: Atomic Force Microscope, Atomic Force Microscopy 12
13. γ-TuRC: γ-tubulin Ring Complex 13
14. MTOC: Microtubule Organizing Center 13
15. GTP: Guanosine Triphosphate 13
16. GDP: Guanosine Diphosphate 13
17. NTP: Nucleotide Triphosphate 15
18. G-actin: Globular (Monomeric) Actin 16
19. F-actin: Filamentous (Polymeric) Actin 16
20. ATP: Adenosine Triphosphate 16
21. ADP: Adenosine Diphophate 16

Symbol Page

22. Pi: Inorganic Phosphate 16

23. ABP: Actin Binding Protein 17

24. ARP: Actin Related Protein 17

25. ERM: Ezrin Radixin Moesin Family 18

26. PIP_2: Phosphatidylinositol 4,5-biphosphate 18

27. PCC: Pericellular Coat 19

28. eGFP: Enhanced Green Fluorescent Protein 20

29. GFPn: eGFP-labelled Neurocan Binding Domain 20

30. BM: Basement Membrane 20

31. ECM: Extracellular Matrix 21

32. CAF: Cancer Associated Fibroblast 22

33. EGF: Epidermal Growth Factor 22

34. TC: Tropocollagen 23

35. LOX: Lysyl Oxidase 23

36. CSK: Cytoskeleton, Cytoskeletal 24

37. integrin: Integral Transmembrane Protein 17

38. FA: Focal Adhesion 26

39. FAC: Focal Adhesion Complex 26

40. GTPase: Guanosine Triphophatase 26

41. FAK: Focal Adhesion Kinase 26

42. ROCK: Rho-associated Protein Kinase 26

43. SMFS: Single Molecule Force Spectroscopy 27

Symbol Page

44. SCFS: Single Cell Force Spectroscopy 27

45. aa: Amino Acid 28

46. FRET: Förster Resonance Energy Transfer 28

47. LIMK: LIM Kinase 29

48. PI(4)P5K: Phosphotidylinositide 4P-5 Kinase 29

49. mDia: Mammalian Homolog of *Drosophila diaphonous* 29

50. WASp: Wiskott-Aldrich Syndrome Protein 29

51. EMT: Epithelial-mesenchymal Transition 30

52. MET: Mesenchymal-epithelial Transition 30

53. cAMP: Cyclic Adenosine Monophosphate 32

54. GEF: Guanine Nucletide Exchange Factor 32

55. ERK: Extracellular Signal-regulated Kinase 32

56. PF: Proteolytic Factor 33

57. MLC: Myosin Light Chain 33

58. MMP: Matrix Metalloprotease 33

59. GM6001: A Particular Broad Spectrum MMP Inhibiting Drug 33

60. 2D: Two-dimensional 37

61. MSD: Mean Square Displacement 37

62. DLS: Dynamic Light Scattering 39

63. DWS: Diffusing Wave Spectroscopy 39

64. PWS: Partial Wave Spectroscopy 39

65. MTC: Magnetic Twisting Cytometry 40

Symbol Page

66. HASM: Human Airway Smooth Muscle 41

67. USR: Uniaxial Stretch Rheometer (Parallel Plates) 43

68. SPM: Scanning Probe Microscope 44

69. STM: Scanning Tunneling Microscope 44

70. Si: Silicon 44

71. Si_xN_y: A Silicon Nitride 44

72. deflVolts: AFM Cantilever Deflection Measured in Volts 45

73. InvOLS: Inverse Optical Lever Sensitivity 45

74. Z-position: Vertical Displacement of Cantilever's Fixed End 45

75. JKR: Johnson-Kendall-Roberts 54

76. DMT: Derjaguin-Muller-Toporov 54

77. MFP3D-BIO: AFM from Asylum Research 55

78. NPS: Nano-positioning System 55

79. SPAD: Single Photon Avalanche Detector 56

80. RNA: Ribonucleic Acid 59

81. dsDNA: Double Stranded DNA 60

82. FLIM: Fluorescence Lifetime Imaging Microscopy 69

83. CLSM: Confocal Laser Scanning Microscope 69

84. AFM-CLSM: Combined AFM and CLSM Setup 69

85. TCSPC: Time Correlated Single Photon Counting 71

86. NCI: National Cancer Institute 74

87. UN: A Poorly Named Cell Mechanics Consortium 75

Symbol Page

88. EMCCD: Electron Multiplying Charge Coupled Device 76

89. KSD: Kernel Smoothing Density 83

90. BE: Barrett's Esophagus 94

91. ER+: Estrogen Receptor Positive 98

92. E2: 17β-estradiol 98

93. 4-OHT: 4-hydroxytamoxifen 98

94. ERα, ERβ: Canonical Estrogen Receptors 99

95. PR: Progesterone Receptor 99

96. HER1, HER2: Epidermal Growth Factor Receptors 99

97. IDC: Invasive Ductal Carcinoma 100

98. NHE1: Sodium Hydrogen Ion Exchanger 1 115

99. 2ME2: 2-methoxyestradiol 116

100. PKC: Protein Kinase C 118

101. ER-: Estrogen Receptor Negative 118

102. GPR30: G-protein-coupled Membrae Estrogen Receptor 1 122

103. DMEM: Dulbecco's Modified Eagle's Medium 125

104. CDT-FBS: Charcoal Dextran Treated Fetal Bovine Serum 125

105. HEPES: (4-(2-hydroxyethyl)-1-piperazineethanesulfonic Acid 125

106. FWHM: Full Width at Half Maximum 126

107. RMA: Robust Multi-array Averaging 127

108. NCPH: Normalized Cell Protrusion Height 130

109. Y-27632: A Particular ROCK Inhibiting Drug 131

Symbol Page

110. DPBS: Dulbecco's Phosphate Buffered Saline....131

111. APTES: (3-aminopropyl)triethyoxysilane....143

112. GA: Glutaraldehyde....143

113. DMSO: Dimethyl Sulfoxide....144

114. HBSS: Hank's Buffered Salt Solution....144

1. INTRODUCTION

1.1 Overview

Cancer has afflicted humans since at least the time of the earliest extant writings on medicine from ancient Egypt. Technology has since enabled modern scientists to greatly increase their knowledge of physiology and the nature of cancer. In the last half century, the discovery of DNA and the central dogma of molecular biology transformed our understanding of organisms as a complex hierarchy, from molecules to organelles, cells to organs. Physics has underlied this progress, in part through the application of physical principles to biological theory (such as Schrödinger's hypotheses about the nature of the unknown genetic material[1]), as well as the application of physical methods to biological problems (such as Crick *et al.*'s use of X-ray diffraction to elucidate the helical structure of DNA[2]).

In spite of our developing knowledge of cancer, our attempts to cure, treat, and control the disease have not been much improved. In the past 4 decades, the age-adjusted mortality has not decreased[3]. This may be due in part to an overwhelming emphasis on genetics and biochemistry, with some critical physical principles falling to the wayside. Researchers too readily view the cell as a mixed bag of enzymes and chemical reactions, or as a computer encoding and processing genetic information, without accounting for the cell foremost as a complex physical object with specialized material properties. Fortunately, physical aspects of cells and the microenvironment of tumors and tissues are lately coming into sharper focus in multidisciplinary views of cancer initiation, tumor growth, and metastasis.

In the last decade, two important notions have been realized: that cancer cells of many types have abnormal mechanical properties (which may potentially be exploited therapeutically); and that the three-dimensional microenvironment has a profound influence on cell phenotype and behaviour. Yet the former realization has been made almost entirely through mechanical measurements of cells in less physiologically relevant microenvironments (such as on cells adherent to polystyrene Petri dishes). This motivates a reassessment of cancer cells' mechanical properties in physiologically relevant three-dimensional microenvironments.

Perhaps the mechanical property most investigated to date is cell stiffness or elasticity. The mechanical stiffness of individual cells is important in tissue homeostasis[4], cell growth, division, and motility[5,6], and the epithelial-mesenchymal transition in the initiation of cancer[7]. At the bulk tissue level, abnormally high stiffness has been indicative of a tumor since ancient times. At the single cell level, cancer cells have been reported to be less stiff (or alternatively "softer", "more compliant", "more deformable", "more elastic") than their normal counterparts[8,9,10]. This has been observed in cancers of the bladder[11,12] and breast[13,9,10,14], leukemia[15,16], melanoma[17], and in transformed fibroblasts[13,18,19]. For a comprehensive overview see[20]. These observations may prove useful in developing clinical prognostic and diagnostic methods based on mechanical phenotyping to supplement biochemical markers in the identification of malignant cells from pleural effusions, lymph or blood samples. Moreover, understanding the fundamental causes of increased elasticity in cancer cells may be instrumental in inhibiting tumor growth and impeding metastasis. The main aim of my work presented in this thesis is the

development and application of a quantitative experimental method for the determination of the elasticity of cells embedded in 3D matrices.

1.2 Organization

In Chapter 2 of this thesis, I review essential background material. §2.1 begins with the basics of cancer. §2.2 covers the mechanobiology of the eukaryotic cell cytoskeleton (§2.2.1), extracellular matrix (§2.2.2), and mechanotransduction (§2.2.3). §2.3 introduces a variety of experimental techniques applied in the measurement of cell mechanical properties. §2.4 treats in detail atomic force microscope based indentation, with subsections covering the principles of the technique, indentation force-depth curves, and the models used to interpret the raw data. In Chapter 3, I present my results from 5 research projects, with a section for each. Each section is divided into subsections for an overview, the results, and the methods used. §3.1 briefly covers common experimental methods. §3.2 presents a comparative study of EPC2 normal squamous columnar esophageal cells, CP-A metaplastic Barrett's esophageal cells, and CP-D high-grade dysplastic Barrett's esophageal cells. This work resulted in publication of a research article in *Physical Biology*, of which I am a first author[21]. §3.3 briefly presents measurements on MCF7 non-metastatic breast adenocarcinoma cells. This work was done as part of another collaboration (the National Cancer Institute "United Nations" of Cell Modulus Measurements) and is in preparation for publication. Some of these results are included in another research article published in *Biophysical Journal*[14], of which I am third author. §3.4 is a comparative study on the mechanical properties of MDA-MB-231 metastatic breast adenocarcinoma cells and MCF-10A non-tumorigenic mammary epithelial cells in a

conventional two-dimensional microenvironment. My experimental work on this project was part of a greater network collaboration (the Physical Sciences-Oncology Centers Network Cell Line Exercise), resulting in publication of a research article in *Nature Scientific Reports*[22]; in addition to my experimental work, I was also responsible for handling the data, preparing the figures, and assisting in writing the manuscript, and I am the 'first authorship leader' of the article. §3.5 presents a study on the influence of the steroid sex hormone estrogen and the endocrine therapeutic drug tamoxifen on the mechanical properties and gene expression of tamoxifen-resistant and tamoxifen-sensitive subclones of the MCF7 cell line. This work was part of a collaborative pilot project, and is in preparation for publication. §3.6 presents novel methods developed to quantify the mechanical properties of single cells partially and fully embedded in physiologically relevant 3D extracellular matrices, and the findings from a study applying these methods to MDA-MB-231 cells invading 3D collagen I hydrogels. This work has resulted in the completion of a manuscript currently submitted for publication, of which I am a first author. Finally, chapter 4 is devoted to an outlook on future work.

2. BACKGROUND

2.1. Cancer

Cancer is a class of diseases which occur at the cellular level in multicellular organisms. Cancer is characterized by some cells in a tissue or other part of the body failing to cooperate. These cells stop sending and receiving important biochemical and biomechanical signals to and from other cells around them which normally regulate their activities and responses to the microenvironment. In the absence of this cellular communication, cancer cells are liable to undergo uncontrolled division, abstain from apoptosis, initiate angiogenesis, and reprogram their microenvironment. One interesting and promising new perspective on cancer is to think of it as a reversion of cells in a multicellular organism to a pre-multicellular *modus operandi*, concomitant with the recovery of an ancient gene expression profile[23].

Hallmarks of cancer include self sufficiency in growth signals; evasion of growth suppressors and insensitivity to anti-growth signals; evasion of immune cells that would otherwise destroy them; activation of tissue invasion and metastasis; limitless replicative potential (immortality); eliciting of tumor-promoting inflammation and sustained angiogenesis; genome mutation, and chromosome instability and polyploidy; deregulation of cellular energetics and metabolism; and evading apoptosis and cell death[24,25]. These activities and traits often result in the growth of macroscopic tumors that impinge on the normal functioning of the healthy tissues around them.

The development of cancer can be viewed as a progressive series of stages. While cancerous tissue itself is disorganized, the program of cancer development, like

embryogenesis or wound healing, follows an organized and highly regulated sequence of events[26]. Cancers of epithelial tissues (carcinomas) begin with initiation and promotion. In initiation, a carcinogen or mutagen induces a mutation in a gene or genes in the genome of a cell or small number of cells. Cancer is typically understood as being monoclonal (i.e. beginning with only a single cell, from which all other malignant cells originate thereafter) though there are some polyclonal exceptions, and there is very little chance of making this determination in any case. In the absence of environmental or other contributing factors, an initiated cell is latent and cancer will not progress. Inflammation, fibrosis, promoting agents or further exposure to carcinogens can cause such a cell to progress.

After initiation, the tissue begins to exhibit neoplasia. Hyperplasia is the uncontrolled proliferation of normal cells, which may be hypertrophic, and may lead to benign tumors, but not cancer. In contrast, proliferation of genetically abnormal (pre-cancerous) cells is known as neoplasia. In metaplasia, cells undergo a transformation by which they take on an ectopic gene expression profile and phenotype. This can be viewed as a de-differentiation event, increase in stemness, and a re-differentiation event. For example, in the pre-cancerous state known as Barrett's esophagus, normal columnar squamous epithelial cells of the esophageal lining adopt the phenotype of cells from the intestine. Metaplasia may occur before, after, or concurrently with neoplasia. Dysplasia is characterized by a disorganization of the epithelium, in which proliferative cells grow in an uncoordinated manner. Pathologists classify dysplasias as either "low grade" or "high grade" based on the degree of tissue disorganization and heterogeneity, cell, nuclear and nucleolar size, morphology, and other

histological features (a.k.a the degree of anaplasia). Dysplasias may occur when epithelial cells de-differentiate and remain in a phenotypically ambiguous state. Dysplasia may occur before, after, or concurrently with metaplasia or neoplasia, and sometimes does not progress to a carcinoma.

The next stage is carcinoma *in situ* (CIS) or *in situ* neoplasm. There is disagreement whether this should be classified as cancer proper, as CIS has no metastatic potential unless it progresses to cancer, or rather, that it is cancer just in case it metastasizes. The designation CIS is reserved for malignancies that are confined to the epithelium of origin, with no breaking of the basement membrane or invasion into the stroma. Tumors are graded on a scale of 1-4 (4 being most malignant) based on their degree of anaplasia.

The remaining stages are steps in the process of metastasis, i.e. the spreading of cancer from one part of the body to another. This process is thought to occur by circulating tumor cells, which have left the tumor from which they originated. In the case of epithelial tumors, cells are thought to leave the epithelium by breaking through the basement membrane and undergoing an epithelial-mesenchymal transition, during which they adopt a motile phenotype like mesenchymal cells such as fibroblasts. These cells grow or migrate into the adjacent stroma. Intravasation, the entry of a cell or cell cluster into the lymphatics or vasculature, occurs next. Cells may enter by forcing their way between endothelial cells or even by moving through a single endothelial cell. In the vasculature, the cells are moved by fluid flow, typically ending up jammed in a distant capillary bed. At this point, the cell(s) may extravasate across the endothelium and re-enter the stroma. Finally, they establish a new site of

growth and proliferation in the ectopic tissue, forming a metastatic secondary tumor. From either the primary tumor or the new metastatic site, cells may metastasize further to other sites in the body[27]. Metastasis eventually causes catastrophic systemic failure, resulting in death from a number of different causes, including infection (from compromised immune function) respiratory, cardiovascular or liver failure,as shown in Figure 2.1[28].

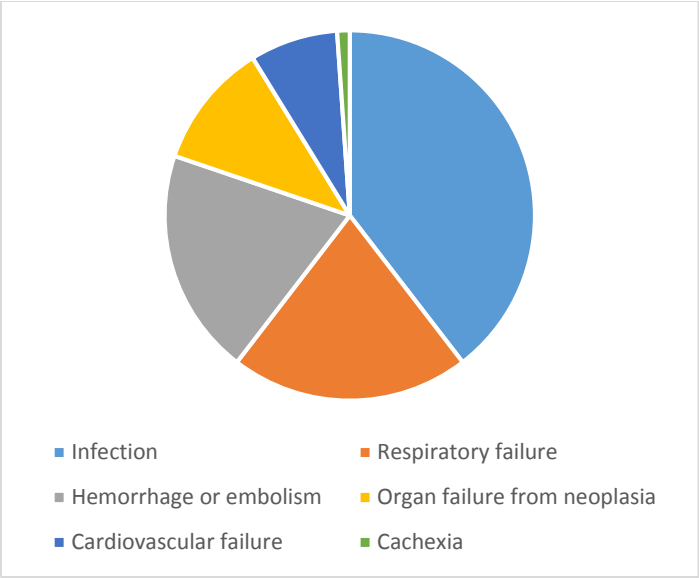


Figure 2.1: Causes of Death in Cancer Patients. Data from a retrospective study[28].

As evident in the following sections, cell mechanics and mechanobiology play a number of roles in the processes described above[20].

2.2 Cell Mechanibiology

2.2.1 The Eukaryotic Cytoskeleton

The cell is the fundamental unit of life. Multicellular organisms are unimaginably complicated systems of single cells, proteins, and matrices that are organized into

organs, tissues, bones, and a variety of other structures with special functions. In order for a multicellular organism to thrive, the cells that comprise it must cooperate as if in a vast and complex society. In this context, the mechanical properties of eukaryotic cells are important in tissue homeostasis[4], cell growth, cell division, and cell motility[5,6], and these properties are primarily governed by the cell cytoskeleton (CSK).

The primary function of the CSK is to provide mechanical strength and structural integrity to cells and the tissues they comprise. In addition, the microtubule (MT) network of the CSK functions as a "highway" for intracellular transport of mitochondria, vesicles, other organelles, and a wide variety of macromolecules. This transport is enabled by molecular motor proteins such as dynein (+ end to − end) and kinesin (− end to + end), which are capable of moving cargo throughout the cell at superdiffusive rates via hydrolysis of nucleoside triphosphates[29].

The cytoskeleton also plays an essential role in mitosis. During cytokinesis, actin and myosin form a contractile ring around the cell equator and ingress to form a cleavage furrow and midbody, which abscisses the membrane, resulting in the division of one cell into two. Furthermore, microtubules and associated motor proteins are required to form the mitotic spindle, which attaches to the kinetochores of sister chromatids during cytokinesis[29].

Nuclear Space and Nuclear Envelope

The nuclear space is filled with nucleoplasm, as well as euchromatin (i.e. lightly packed or decondensed chromatin, available for transcription), nucleoli and other nuclear bodies. Nuclear filaments co-localized with nuclear actin form a framework

in which nucleoli are enmeshed[30]. The form and function of actin and actin related proteins in the nucleus is not yet well understood, but nuclear β-actin may be involved in transcriptional regulation and quiescence[31].

At the periphery of the nucleoplasm, condensed or tightly-packed heterochromatin aggregates near and docks at the nuclear envelope (NE), which consists of the nuclear lamina, inner nuclear membrane (INM), outer nuclear membrane (ONM), and the nuclear pore complexes (NPCs)[32]. The lamina, contained within and anchored to the inner nuclear membrane, is composed of lamins, which form coiled-coil dimers like intermediate filaments (IFs), but unlike cytoplasmic IFs, tend to form paracrystals rather than filaments[32]. Lamins are known to provide shape and structural integrity to the nucleus and provide a link between the nucleoskeleton and cytoskeleton; lamin deficiency has been shown to weaken the cytoskeleton and impair cell migration[33], but little is known about the structures formed by lamins at the envelope or deeper within the nucleoplasm[32]. The nuclear membranes form a pair of phospholipid bilayers, between which is the perinuclear space[29]. The outer membrane is contiguous with the endoplasmic reticulum, and the nuclear pore complexes form channels through the space linking the cytoplasm and nucleoplasm. The membranes contain integral proteins such as nesprins and Sun proteins. These cluster into organized LINC (linker of nucleus and cytoskeleton) complexes that link the cytoskeletal actin, IFs, and microtubules (MTs) to the NE[34]. This enables mechanotransduction between the extracellular environment and the chromatin, and thus mechanoregulation (which is as yet poorly understood)[35,36]. Furthermore, hydrophobic forces dependent on DNA methylation may influence chromatin

condensation and thus gene expression[37]. Intermediate filaments (IFs) directly link the NE to the cell membrane, so physical forces may also play a direct role in opening or closing nuclear pore complexes, allowing entry of soluble factors regulating transcription. The cytoskeleton may therefore modify itself via regulation of its own gene expression[38].

As a whole, the nucleus is in mechanical equilibrium. Histone tail-tail interactions stabilized by other proteins are thought to generate inward-directed chromatin condensation forces on the nucleus, which are balanced by outward-directed forces generated from the outside by cytoskeletal structures under tensile pre-stress[39].

A variety of nuclear stiffness measurements have been conducted to date. Meister *et al.* used glass microplate compression to find the elastic moduli of bovine aorta endothelial cells (0.5 kPa) and their nuclei (5 kPa in the intact cell, and 8 kPa when isolated with Igepal and citric acid)[40]. Burgkart *et al.* probed chondrocyte nuclei by micropipette aspiration (MPA), finding an equilibrium elastic modulus of ~1 kPa (with mechanically isolated nuclei being somewhat stiffer than chemically isolated nuclei), whereas intact cells were ~3-4 times softer[41]. Lammerding *et al.* used MPA and atomic force microscopy (AFM) to measure creep compliance in isolated TC7 cell nuclei, distinguishing swollen, unswollen, and shrunken nuclei. Unswollen and shrunken nuclei had complex elasticity prefactors ~3 kPa (by AFM) and ~6 kPa (by MPA)[42].

The migration of cells through matrix or between neighboring cells has been shown to depend on the deformability of the nucleus, with the nucleus' deformation and displacement being a rate-limiting step in motility[43,44,45,46,14].

In another study on Swiss 3T3 fibroblasts, application of shear fluid flow induced rigid body displacement and rotation of the nucleus detectable with fluorescence microscopy; latrunculin-induced f-actin depolymerization did not appreciably change these motions, but nocodazole-induced microtubule disruption did[33].

Microtubules

Microtubules (MTs) are dynamic cylindrical structures 25 nm in diameter, that may grow up to several μm in length. They are polymers of heterodimers of two 55 kDa polypeptides, the α-tubulin and β-tubulin monomers. These cylinders are composed of 13 tubulin protofilaments, which consist of linear polymers of alternating α and β monomers. The polymerization of the monomers nucleates in the perinuclear space, at the centrosome, on the γ-tubulin ring complex (γ-TuRC). The centrosome (a specific type of microtubule organizing center, or MTOC) consists of 2 MT aggregates (centrioles) which form at right angles; during cytokinesis MTs originating at this locus are responsible for attaching to and pulling apart the sister chromatids.

Due to the polarity of the monomers, the polymer has different properties on either end; the γ-TuRC side is known as the minus (−) end, and the opposite side is the (+) end. The (−) end is relatively stable due to the γ-TuRC , with nearly all polymerization and depolymerization occuring at the (+) end, which has both a higher on rate (k_{on}) and off rate (k_{off}) for the binding and unbinding of new monomers[47]. The monomers bind more strongly along the protofilament axis than they do laterally, so at its (+) end a microtubule may fray, with the protofilaments dissociated from each other.

The polymerization dynamics are dependent on hydrolysis of GTP bound to β-tubulin monomers. The free concentration of GTP in the cell typically exceeds that of GDP by an order or magnitude, so MT polymerization is nearly always possible, and indeed crucial for the cell's survival. GTP-bound tubulins tend toward polymerization, while GDP-bound tubulins tend toward depolymerization. Furthermore, tubulin-bound GTP tends toward hydrolysis. The slight mismatch of these rates results in a slight delay between the assembly and hydrolysis, yeilding a GTP-tubulin cap that stabilizes growth. When the cap is lost, the microtubule rapidly depolymerizes[48]. This tendency of changing length is called dynamic instability. The half-life of a microtubule polymer is on the order of a few minutes.

There are a number of MT-specific drugs that have been used in e.g. chemotherapy, as well as in scientific studies of microtubule function. Paclitaxel (Taxol®) is a compound found in the bark of a species of Yew tree (*Taxus brevifola*) that binds and stabilizes MTs. Colchicine and colcemid, as well as vinblastine and vincristine, bind MT subunits and prevents their polymerization, as does Nocodazole.

Microtubules have an extreme persistence length of ~6 mm, a bending stiffness of 2.6E-23 $N \cdot m^2$, and Young's modulus of 1.9 Gpa[49]. This makes them particularly strong structural components. In the conceptual framework of cellular tensegrity, microtubules are viewed as load-bearing, compression-resistant struts[50]. The longitudinal elastic resonances of MTs occur at 465, 930, and 1,395 MHz; intriguingly, they can be excited electromagnetically for cancer detection[51].

Various techniques have investigated the mechanical role of microtubules. Stamenović *et al.* found microtubules to support compression and to have a relatively

small (~14%) but significant contribution to balance a cell's contractile prestress[52]. Katoh *et al.* found longitudinal shear stiffness of cardiomyocytes to depend importantly on microtubules[53]. *In vitro* studies of pure F-actin gels by Weitz *et al.* showed the addition of even low concentrations of microtubules to have significant effects on the gel's stress-strain curve[54]. Magnetic twisting cytometry experiments by Wang showed Taxol increased stiffness and viscosity of bovine capillary endothelial cells by 10%[55]. Harris and Charras found nocodazole reduced MDCK-II cell elasticity by 25% in AFM indentation experiments[56]. In contrast, Rotsch and Radmacher observed no changes due to treatments with colchicines, colcemide, or Taxol in NRK fibroblast elasticity probed by relatively shallow AFM indentations, but this may be because shallow indentations cannot detect the influence of the microtubule network, which radiates outward from microtubule organizing center at the nucleus[57].

Intermediate Filaments

Another important family of structural elements are the intermediate filaments (IFs). The nuclear lamins of the A, B, and C subtypes (see §2.1.1.1) are intermediate filaments (though they assemble differently). Vimentin is an IF abundant in mesenchymal cells. The keratins are abundant in epithelial cells.

The constituent monomers feature a 300 residue central α-helical domain that forms a coiled coil. Pairs of coiled coils dimerize, and dimers dimerize to form tetramers. These tetramers are stable protofilaments, with staggered ends. The IF itself is then a rope-like structure made of a bundle of 8 protofilaments. This hierarchical self-assembly of monomers is an energetically favorable process and does not require

NTP hydrolysis to proceed. IFs are stable over long time periods, have low solubility in salts, and are not dynamic, unlike actin and MT structures.

IFs have a diameter of 10 nm, persistence length of ~1 μm, bending stiffness of $4 \cdot 10^{-27}$ $N \cdot m^2$, and Young's modulus of 1 GPa[49]. Vimentin deficiency in fibroblasts was found to result in lower endogenous contractile forces[49]. IFs contribute to cell stiffness, and may also serve to prevent the buckling of MTs under compression; Like actin stress fibers, IFs are thought to carry tensile pre-stress[49].

Actin Cortex, Microfibrils and Stress Fibers

Actin structures have perhaps the greatest influence on the mechanical properties of the cytoskeleton. Monomeric or globular actin (G-actin) (MW 43 kDa, 375 aa) polymerizes into a polarized strand of filamentous actin (F-actin) that is ~6-9 nm in diameter and variable in length (up to several μms) with one "barbed" (+) end and one "pointed" (−) end. G-actin binds one Ca^{2+} and one ATP. This activated G-actin binds the (+) end upon hydrolysis of its ATP to ADP + Pi, whereupon the ADP remains bound in the F-actin filament.

Polymerization takes places more favorably at the (+) end, while depolymerization occurs primarily at the (−) end. As monomers are removed from the (−) end and added to the (+) end, a particular monomer traverses the length of the filament, ending up at the (−) end. This dynamic process is called treadmilling. The lifetime of an actin filament varies in vivo. Confluent bovine aortic endothelial cells had a mean lifetime of ~40 min, with ~70% of actin being filamentous; subconfluent cells had a mean F-actin lifetime of ~8 min, with only 40% of actin filamentous[58,59].

Over the cytoplasmic pH range (6.8-8.0) actin self-assembly is also pH dependent. While the kinetics are highly sensitive to cation identities and concentrations, in vitro actin self-assembly has been shown to be substantially accelerated at lower pH; for example, at pH 6.6 in 2 mM Mg^{2+} the kinetic half-time of an actin filament in an in vitro gel is 1 min, whereas at pH 8.0 in 0.5 mM Mg^{2+} the lifetime is 310 min[60].

Polymerization and depolymerization are tightly regulated by a wide variety of actin binding proteins (ABPs) that can bind, cap or sever the filament, or produce branches. The activity of ABPs is sensitive to ATP/ADP, GTP/GDP, Ca^{2+} and other ion concentrations, as well as GTPases and growth factors.

Some ABPs specialize in the construction of linear assemblies. Profilin recruits G-actin subunits, speeding elongation of filaments. Profilin activation is regulated at the membrane by external signals and can result in formation of motile structures (filopodia, lamellipodia etc.). Large parallel bundles of unbranched actin filaments are produced by formins, which is associated with the (+) end, allowing the filament to extend rapidly. Fimbrin has actin binding sites 14 nm apart, and thus constructs tight parallel bundles, which also exclude myosin.

Filaments can bundle into stress fibers, with the help of plastin, α-actinin (which has F-actin binding sites 30 nm apart), and other ABPs. Fibers reinforce the actin cortex and are important for organelle transport and cell motility. In muscle cells, actin forms thick contractile fiber bundles and complexes with myosin filaments which specialize in generating contractile forces.

Some ABPs specialize in forming highly branched, gel-like structures. Filamin forms a junction between filaments, allowing the assembly of a 3D lattice. Some malignant

melanomas lack filamin, preventing lamellipodia and normal crawling. They exhibit blebbing and bleb-based motility[29]. In the cortex just beneath the plasma membrane, actin related proteins (ARPs) form complexes such as Arp2/3 complex which catalyze the nucleation of filaments from the (−) end. The complexes can then anchor the (−) end of the nucleated filament to another filament, resulting in a dense and highly branched meshwork of filaments known as the actin cortex[29].

Other ABPs are responsible for dismantling actin structures. Thymosin binds subunits, preventing assembly of filaments. Cofilin binds ADP-actin filaments, accelerating depolymerization. Cofilin acts in a pH-dependent manner, resulting in a higher ratio of monomer:polymer at elevated pH[61]. Gelsolin severs filaments and binds to (+) ends. Capping proteins prevent assembly and disassembly at the (+) end.

Yet other ABPs serve to anchor actin to the cell membrane or nuclear membrane. Ezrin, radixin and moesin (ERM family proteins) anchor actin to the cell membrane. They also interact with other mechanosignalling molecules and influence cell shape and size, as well as exo- and endocytosis. ERMs bind integral membrane proteins like CD44 and actin filaments and are regulated (via phosphorylation and PIP_2 binding) by several kinases and signals. Spectrin tetramers form a hexagonal lattice under the phospholipid bilayer, anchoring to it via integral membrane proteins. The spectrin cortex serves as an important scaffold for proteins in the cell membrane, as well as an anchoring point for other cytoskeletal proteins. Spectrin has F-actin binding sites 200 nm apart.

Actin specific drugs are found in nature and are used to modulate the cytoskeleton. Phalloidin (from the deathcap mushroom *Amanita phalloides*, and responsible for its toxicity) binds and stabilizes actin filaments. Cytochalasins are a class of fungal metabolites that cap the (+) ends of filaments, blocking their polymerization and elongation. The marine sponge *Theonella swinhoei* produces a metabolite (swinholide) that sequesters actin dimers, preventing them from assembling into filaments or fibers. Sponges from the geni *Latrunculia* and *Negombata* produce latrunculins, which bind subunits and prevent their polymerization.

Actin filaments have a persistence length of ~15 μm, bending stiffness of $7 \cdot 10^{-26}$ $N \cdot m^2$, and Young's modulus of ~1-3 GPa (c.f. polystyrene, ~3 GPa; bone, ~9 GPa)[49]. Much work has been done on the mechanical properties of the actin cytoskeleton *in vivo* as well as *in vitro* active gels composed of actin and various ABPs[62,63].

Plasma Membrane

The phosopholipid bilayer is about 6 nm thick. According to the fluid mosaic model, it can be thought of as a two-dimensional fluid in which proteins like transmembrane receptors, cholesterols, and focal adhesion complexes are free to laterally diffuse, unless otherwise anchored to the cytoskeleton.

The area-expansion modulus of the membrane (defined as the in-plane biaxial tension divided by the fractional area change) is in the 0.1-1.0 N/m range for pure bilayers, and 0.45 N/m for red blood cells[64,49]. The bending stiffness of the cell membrane is $\sim 2\text{–}4 \cdot 10^{-19}$ N·m for red blood cell membranes, and $1\text{–}2 \cdot 10^{-18}$ N·m for neutrophils. The shear modulus of red blood cells is $\sim 1 \cdot 10^{-6}$ N·s/m. The

phospholipid bilayer contributes negligibly to the membrane's mechanical properties, which are dominated by its protein and carbohydrate composition, as well as its anchorage to the underlying cortex of spectrin and actin.

Pericellular Coat

Many mammalian cells exhibit a layer of polysaccharides known as the pericellular coat (PCC). Details about the mechanics and structure of the PCC are lacking due to its alteration by most methods of investigation. Transfection of cells with eGFP-labelled neurocan-binding domain (GFPn) can reveal the PCC[65]. When present, the PCC can be modelled mechanically as a polymer brush composed of entropic springs with a characteristic brush density and brush length[66,65].

Tensegrity

As described in[67,68], the tensegrity model is based on the architectural concept of tension integrity. In tensegrity structures, mechanical equilibrium is a balance between cables in tension and struts under compression. Each strut is supported on either end by several cables, and each cable is connected to a strut on either end. In the cell, microtubules are treated as struts, while actin filaments, intermediate filaments and stress fibers are treated as cables. One of the main tenets of this model is that the cables are pre-stressed; i.e., when a load is applied to a cable, it responds with a restoring force. Usually the restoring force comes about by geometrical rearrangement of the cables.

Some attempts have been made to quantitatively assess cell mechanics in this context by incorporating the material properties of the constituent cytoskeletal components[52]. However, due to the sheer complexity of the cell, and the active and

dynamic characteristics of the cytoskeleton, it is primarily evoked as a broad, qualitative conceptual framework to which many researchers in the field subscribe.

2.2.2 The Extracellular Matrix

Basement Membrane

The basement membrane (BM) is a dense mat of fibers, typically 40-120 nm thick, underlying epithelia. All epithelial cell types have basement membrane at the basal surface, as well as some non-epithelial cells. The BM functions as a boundary between the epithelium and the stroma (interstitial connective tissue), and serves as a barrier preventing the migration of fibroblasts into the epithelium, or migration of early stage cancer cells into the stroma (as in carcinoma *in situ*). BM is comprised of various fibrous proteins (e.g. collagen IV, laminin, and nidogen) and polysaccharides (proteoglycans and glycosaminoglycans like perlecan and syndecan) secreted by both the epithelial (parenchymal) and stromal (mesenchymal) cells. Collagen IV is less rigid than the fibrillar collagens, and therefore it imparts tensile strength to the BM[29]. Chemical and mechanical cues from the BM contribute to the establishment of epithelial cell apical-basal polarity, which is important for the specialized organ-specific functions of epithelial tissues.

Stroma

The stroma is the extrafibrillar matrix (located outside the fibrillar BM) or "ground substance" filling the interstitial space between the epithelial or parenchymal tissues responsible for the specialized functions of the organs. Stromata are composed of water, glycosaminoglycans (especially hyaluronans), proteoglycans and glycoproteins.

This connective tissue is occupied by mesenchymal cells such as fibroblasts and fibrocytes, which are unpolarized and motile.

Fibroblast phenotype is organ specific and may change in response to external cues. Fibroblasts and inflammatory cells in the stroma can actively alter its composition and density[69]. Fibroblasts secrete the precursors of molecules that form the matrix, and also actively remodel it through adhesion, endogenous force generation, and secretion of proteoyltic factors that break down extracellular matrix (ECM). They also produce soluble paracrine growth factors that regulate epithelial cells' proliferation, morphology, survival and programmed cell death[26]. Importantly, the stroma functions as a repository for these secreted growth factors[70]. Furthermore in CIS, the balance of soluble and insoluble factors promoting or inhibiting angiogenesis in the stroma determines tumor vascularization. The conditions in the stroma therefore heavily influence the adjacent epithelium.

In addition to changes in the epithelium, carcinoma *in situ* is associated with an altered, "reactive" tumor stroma. Tumor stroma is similar to stromata observed in wound healing, featuring increased capillary density, fibrin and collagen I. Cancer associated fibroblasts (CAFs) have been shown to be highly proliferative, and exhibit upregulated production of hyaluronate, collagen I, and epidermal growth factor (EGF). CAFs therefore alter the stroma, providing environmental cues that contribute to the priming of the epithelium such that any initiated cells may progress to malignancy[26]. CAFs can also align the matrix by modulating cross-linking and fiber orientation. This enables contact guidance in 3D matrices that promotes the migration of metastatic cells[69].

Collagen I

The collagens are the most abundant proteins in the body. They can be assembled into a variety of hierarchical structures of different forms and functions (fibers, networks, or transmembrane collagenous domains). The gene encodes a polypeptide, protocollagen. Three parallel left-handed polypeptide helices coil with a one-residue stagger into a right-handed helix, which has propeptides at its N and C termini that are non-triple helical domains, which direct triple-helix folding prior to fibrillogenesis.

The propeptides are essential for the formation of triple-helices, but prevent fibrillogenesis. Once secreted into the extracellular space the propeptides are cleaved, and the resulting molecule is known as tropocollagen (TC). TC is mechanically strong and thermally stable. The triple helix is ~2 nm wide and ~300 nm long. TC monomers are thought to self-assemble into a super-twisted right-handed helix with one another, forming a microfibril. These microfibrils interdigitate with one another to form a spiral shaped fibril. The telopeptides of helices comprising TC monomers are also super-twisted. Lysyl oxidase (LOX) crosslinks the telopeptides within and between microfibrils, forming covalent bonds with each other that stabilize and strengthen the fibrils and microfibrils[71]. While crosslinking via LOX is not required for fibrillogenesis, it provides the fibrils with stability and strength. Due to the staggering of interdigitated microfibrils, the fibrils have characteristic "D-bands" with 67 nm periodicity. D-bands are apparent in TEM and AFM imaging studies of collagen fibrils. Fibrils can aggregate to form larger structures called fibers, and can grow up to 1 cm in length and 500 nm in diameter.

Collagen at many levels of self-assembly is mechanically strong. The tropocollagen monomer has a Young's modulus of ~6-7 GPa and a fracture strength of 11 GPa. Fibrils are only slightly weaker: dehydrated fibrils from bovine Achilles' tendon have a Young's modulus ~5 GPa (which is about half that of rat tail tendon) and a fracture strength of ~0.5 GPa, with a shear modulus of ~33 Mpa and a tensile strength of ~100 MPa[49]. Excessive cross-linking (e.g. as occurs in aging) results in brittle fibrils[72].

Synthetic and Reconstituted Matrices and Microenvironments

A number of engineered materials can be used as platforms for cell culture in 3D, 2D, or in "two-and-a-half" dimensions (2.5D). Some common polymer hydrogels on which cells do not grow can be modified by functionalization with ECM ligands like fibronectin. Polyacrylamide (PA) gels can be selectively functionalized with ECM proteins by micropatterning; since the cells will not adhere on the unfunctionalized regions, cell geometry and mechanics can be controlled on these surfaces[73]. Since the PA stiffness can be tuned, these gels can also be used to study the influence of ECM stiffness on cell physiology. Micropatterning is also used to make elastic pillars out of bioadhesive materials like polydimethylsiloxane (PDMS). Micropatterned PDMS pillar arrays can be used e.g. for characterizing FA distribution and contact stresses of fibroblasts (found to be 5.5 nN/m^2) [74].

ECM scaffolding proteins can be purified from biological sources and polymerized to make biomimetic hydrogels. Fibronectin, laminin, vitronectin, osteopontin, and synthetic scaffolds are now commercially available, but the most widely used matrix is collagen. Collagen I from cow or rat is frequently purified to make collagen

solutions with concentrations up to ~10 mg/ml. Different extraction procedures yield either telocollagen (which crosslinks into thicker fiber bundles) or atelocollagen (which produces a randomly entangled polymer network) solutions which polymerize into hydrogels spontaneously upon pH neutralization. Temperature, humidity and pH during polymerization can be used to tune the gel properties (stiffness, volume, fibrillogenesis)[75]. Ion concentrations and pH are also known to influence the density and swelling of hydrogels[76,77]. Because the ligands in ECM have both structural and chemical-signalling roles, it is sometimes desirable to separately tune stiffness and ligand density. For example, collagen-agarose gels of varying stiffness but constant collagen concentration can be produced, with agarose forming a dense mesh between the collagen fibers, whose organization remains relatively unchanged[78]. Collagen gels covalently bound to a substrate are stiffer than the same gels "floating" or unrestrained, resulting in different cell behaviors during migration[79]. ECM matrices such as fortified collagen scaffolds can also be formed by electrospinning[80].

More complex matrices can also be used for organotypic 3D cell culture. Perhaps not surprisingly, egg white can be used as an inexpensive ECM matrix for 3D cell culture[81]. Reconstituted solutions of murine basement membrane (e.g. Matrigel®) are widely used as a 3D ECM for mammary epithelial cell culture; normal cells in this matrix proceed to form multicellular organotypic structures somewhat resembling the lumen of a milk duct (acini). Reconstituted matrices are complex and contain a wide range of proteins, proteoglycans, and growth factors; this makes them more physiologically realistic than simpler hydrogels but their exact composition is unknown and varies from lot to lot, rendering experiments more difficult to control.

2.2.3 Mechanotransduction

Cell-Cell Adhesion

Epithelial tissue homeostasis requires individual cells to be in mechanical equilibrium with their neighbors. This equilibrium is maintained by cell-cell adhesion (and is disrupted by neoplastic growth and metastasis, which often features distinctive loss of adhesion, such as during the E- to N-cadherin switch). Through adhesive junctions, cells can push and pull on their neighbors, transferring and distributing loads and forces. The extracellular contacts are mediated by transmembrane proteins called cadherins, which comprise a large family of Ca^{2+}-dependent adhesion molecules (cadherins) which exhibit homophilic binding. Removing Ca^{2+} from the extracellular medium disrupts cadherin adhesion[29].

Adherens junctions anchor on the outside of one cell anchor to those of an adjacent cell, and each anchors to actin filaments on the cytoplasmic side, thus connecting the two actin cytoskeletons. E-cadherins bind to one another on their extracellular domains, and to their cytoplasmic domains, they bind the head domains of vinculins. The tail domains of the vinculins then bind to both plasma membrane and F-actin[29]. Catenins reinforce these connections, further linking the cadherins to the CSK. In desmosomes, other cadherins (desmogelin and desmocollin) are used; they bind homophilically on the extracellular domain and on the intracellular domain they bind desmoplakins, which form a dense plaque that connects to keratins.

Additional cell-cell junctions such as tight junctions and gap junctions (i.e. plasmodesmata) provide channels from cytoplasm to cytoplasm, resulting in electrical and metabolic coupling. Tight junctions are important for maintaining

apical-basal polarity; by "sealing" the epithelium, they enable the maintenance of distinct chemical milieu in the apical and basal extracellular medium[29].

Cell-Matrix Adhesion

Epithelial tissue homeostasis also requires cell-matrix adhesion; loss of adhesions can result in apoptotic signaling[82]. Cell-matrix adhesion is accomplished by the binding of integral transmembrane proteins (integrins), which form a class of at least 24 different proteins. The functional form of an integrin is a heterodimer composed of α and β subunits. Specific integrins are expressed for distinct functions; e.g., β_6 integrin is only present during wound healing[70]. A large number of cytoplasmic proteins interact with integrins at their intracellular domain, and a large number of molecules and proteins interact at their extracellular domains. ECM ligands such as collagen, fibronectin, and laminin, growth factor receptors, proteases and protease receptors bind the extracellular domains of various integrins, which in turn anchor intracellularly to different parts of structural proteins of the CSK via scaffolding proteins such as talin, paxilin, vinculin, filamin, and α-actinin[70]. Hemidesmosomes link intermediate filaments to the ECM. For example, keratin can bind to a plaque of plectin which is connected to collagen XVII via $\alpha_6\beta_4$ integrin.

Integrins bind their ligands with lower affinity, at 10-100 fold higher concentrations than other transmembrane adhesion molecules. Integrin activation involves changes in binding affinity and avidity (i.e. the potential to diffuse or aggregate in the membrane). Upon activation, large numbers of integrins cluster, forming a plaque that connects the CSK to the ECM at a locus known as a focal adhesion (FA). Nascent FAs under certain conditions may increase in size and in the number and

complexity of intracellular linkages to various CSK anchoring proteins and to various ECM ligands, thus maturing into a focal adhesion complex (FAC), sometimes exceeding 100 different types of molecules.

Both the clustering of integrins into stable FAs, and FA turnover or destabilization depend on the guanosine triphosphatases (GTPases) Rac and Cdc42[83]. ECM components and growth factors control the activation state of Rac1 and Cdc42, and thus regulate FA assembly[84]. Integrins in turn regulate Rho via intermediate signalling proteins such as Src (a proto-oncogenic tyrosine-protein kinase), Rac, and RhoGAP proteins[85]. FA maturation and FAC formation requires Rho activation for recruitment of integrins, scaffolding proteins, and actin filaments to the site. Intracellular calcium, stretch-activated ion channels, Src and focal adhesion kinase (FAK) regulate FA assembly and disassembly. Due to their complexity, the details of all of these mechanisms and dynamics have not yet been fully unravelled.

Focal adhesions are capable of transfering endogenous forces (e.g. those due to the contraction of actomyosin fibers) to the fibers of the ECM. Conversely, they can transfer exogenous forces from ECM fibers into the cell. This is known as mechanoreciprocity. Furthermore, exogenous forces are capable of activating integrins and driving the formation of focal adhesions[86,87]. Riveline et al. showed that ROCK was required for FA assembly in the absence of external forces, but not with a force applied, in which case the formin and Rho effector, mammalian homolog of *Drosophila diaphonous* (mDia1), was required instead[88].

The intracellular tension maintained by FACs in fibroblasts grown on micropatterned elastic surfaces was calculated to be 5.5 $nN/\mu m^2$[2,74]. Vascular

endothelial cells were found to be capable of contracting the luminal matrix by over 50%[89]. Adhesion forces in specific interactions (e.g. integrin-fibronectin binding) can also be probed by AFM with single molecule force spectroscopy (SMFS) and single cell force spectropy (SCFS)[90,91,92].

Tension across a protein in a FA may elicit a conformational change that exposes a cryptic binding site with a high affinity for a signalling molecule; upon binding, the protein may undergo yet another change (e.g. activation via phosphorylation). It is thought that in this fashion, mechanical forces can be transduced into chemical signals, and ultimately induce changes in gene expression and phenotype. The molecular details and the players involved in these processes are not yet understood.

Adhesion strengthening is the related notion that application of mechanical tension across FA molecules such as vinculin and FAK can promote FA assembly. Promotion of FA assembly is known to be associated with increased cytoskeletal tension[93]. Upon recruitment of vinculin (even before the maturation of FACs), integrins are capable of exerting migration forces; tension applied from inside or outside the cell upon fibronectin receptors induces formation of FACs and is correlated to vinculin recruitment, and removal of c-Src enhances connections between vinculin and the CSK[94]. To further investigate the role of vinculin recruitment and force in FA assembly, Schwartz *et al.* developed a single molecule fluorescence force spectroscopy method and applied it to a synthetic vinculin construct. The method requires the insertion of a 40 amino acid (aa) long fragment from a spider silk gene into the vinculin gene sequence between the head and tail domains, that functions like an elastic spring. The spring displacement is probed via

Förster resonance energy transfer (FRET). After calibration, the FRET index reports the force across the vinculin head and tail domains. Interestingly, the authors found that in spite of the correlation between contractility and assembly, vinculin tension is independent of vinculin's FA recruiting activities[95].

Small Rho GTPases

Rho GTPases, belonging to the Ras superfamily, are extremely pleitotropic and important in the regulation of CSK organization, cell motility and invasion. The canonical GTPases RhoA, Rac1, and Cdc42 are currently best understood. Study of GTPases is an area of much recent activity (an entire journal, *Small GTPases*, is devoted to them), and the current understanding of these molecules continues to evolve; for a current overview, see[96].

In the 1990s, Ridley *et al.* showed that lamellae formation was stimulated by Rac and stress fiber formation was stimulated by RhoA[97]. In 1999, Sander *et al.* showed that Rac downregulates Rho activity[98]; In 2000, Zondag *et al.* showed that oncogenic Ras downregulates Rac, leading to increased Rho activity and EMT[99]. The spatial separation of these GTPases at the cell front and rear, and temporal separation of their activation at different points in the process of cell migration, must be highly coordinated in order to elicit coherent motion. Their mutual antagonism also implicates Rho and Rac in the establishment of front-rear polarity during cell motilty[83].

Rho/ROCK signalling is critical to acto-myosin contractility, and also the organization of the actin CSK. RhoA activates ROCK, which then inhibits myosin phosphatase, resulting in the production of myosin light chain, which is essential for

actomyosin contractility. ROCK also activates adducin and LIMK, leading to actin polymerization. Adducin is localized at spectrin-actin junctions and caps actin filaments and promotes their binding to spectrin. LIMK inhibits actin depolymerization by inhibiting cofilin. Furthermore, RhoA leads directly to actin polymerization via phosphotidylinositide 4P-5 kinase (PI(4)P5K) and mammalian homolog of *Drosophila diaphonous* (mDia); mDia also regulates microtubule formation and orientation[96,100]. Currently, it is believed that integrin $\alpha_6\beta_4$ signalling may determine whether RhoA leads to stress fibers or lamellae and membrane ruffling[96].

In 2002, Eden *et al.* showed Rac1 is distributed over the lamellipodium diffusely, and when activated is able to dissemble and thus activate the inactive, trans-inhibited WAVE1 complex; activated WAVE1 activates the Arp2/3 complex, which nucleates actin filaments at the leading edge[101].

Cdc42 interacts with Wiskott-Aldrich Syndrome proteins (WASps) such as N-WASP, which are also capable of activating Arp2/3. Whereas Rac1 is associated with membrane ruffling and lamellae, Cdc42 is associated with the formation of actin-rich surface protrusions called filopodia[102]. Activation of Cdc42 itself is mediated by interactions with integrins.

Epithelial-Mesenchymal Transition

Mesenchymal and epithelial cells have distinct repertoires of adhesion molecules, but by changing their expression levels cells can switch from one phenotype to the other in processes called epithelial-mesenchymal transitions (EMT) and mesenchymal-epithelial transitions (MET). For reviews, see[103,104,105,106].

E-cadherin (expressed highly by epithelial cells), N-cadherin, fibronectin, and vimentin (expressed highly by mesenchymal cells) are often used as biomarkers to identify EMT and MET in epithelial and mesenchymal cells.

EMT occuring in normal embryonic development is classified as Type I EMT. In embryogenesis, formation of the parietal endoderm, the mesoderm and the delamination of the neural crest all require stem cells to undergo EMT; these are called primary EMTs. Thereafter, these stem cells differentiate into a variety of cell types, undergo MET, and form temporary epithelial structures. Some of these cells undergo another, secondary EMT, turning into mesenchymal cells with a more restricted differentiation potential[103]. Formation of the heart requires some cells to undergo a third (tertiary) EMT. Type II EMT occurs during wound healing, menstruation, and organ regeneration. Type III EMT occurs during pathogenesis, e.g. in organ fibrosis and cancer development. Cell mechanical properties are a critical factor in epithelial-mesenchymal transition in the initiation of cancer[7]. Upon successfully metastasizing a distal site, MET is thought to take place.

Slug, Snail, Twist and E-cadherin are some of the proteins critical for these transitions. These processes are also regulated by the GTPases Rac1, Cdc42 and TGFβ (a known tumor promoter), among other factors. EMT is characterized by a loss of cell polarity and cell-cell adhesion (mediated primarily by E-cadherin). Factors like Snail and Zeb which induce EMT also upregulate the expression of matrix metalloproteases (MMPs), that breakdown ECM upon secretion into the extracellular medium[103].

Cell Motility

Epithelial cells are sessile, but other cell types (and cancer cells of epithelial origin) are capable of locomotion through the body by coordinated and directed activities of a wide variety of molecules that regulate the dynamic CSK by mechanosensing, signalling and activation, as well as the disassembly and assembly of actin and microtubule structures. Cytoskeletal signalling is extremely complex, involving crosstalk between a number of molecular cascades. Motility is also influenced by the physical features of both the cell (e.g. volume, deformability, contractility, cortical rigidity, nuclear volume, nuclear deformability) and the ECM (e.g. composition, density, pore size, stiffness, alignment).

The process of locomotion is typically understood in terms of the following 5 discrete steps:

1. Cell polarization and initial protrusion
2. Formation of cell-ECM contacts
3. Cell-surface localized proteolysis
4. Endogenous traction force generation by actomyosin, deforming cell body and ECM
5. Loss of adhesion at the rear and retraction of the trailing edge.

In addition, the nucleus must be displaced in the forward direction, possibly with the aid of pressure exerted on the rearward membrane by the outgrowth of microtubules. In Swiss 3T3 fibroblasts, Cdc42 was demonstrated to regulate microtubule-dependent movement of the nucleus[107]. These processes result in a net forward motion of the entire cell body[108].

Polarization is the acquisition by a motile cell of a directional sense of forward and backward, and functional asymmetry between the cell front and rear. Polarization

can be caused by detection of a gradient in the concentration of a chemoattractant (e.g. cAMP or Ca^{2+})[109], or by mechanical stimulation[110]. Cdc42 directs front-rear polarity by influencing the orientation of the MTOC, sending microtubules growing in the forward direction[83]. Cdc42-mediated polarization can be induced by mild mechanical shear stress[107]. Kinesin motors transport vesicles and Golgi apparatus along the MTs to the leading edge, delivering e.g. β-actin mRNAs and the guanine nucletide exchange factors (GEFs) that initiate activation of small Rho GTPases[111]. Importantly, cells in sufficiently confined channels have been shown to migrate on the basis of osmotic forces alone[112].

Integrins are essential players in motility as well as adhesion. Activated integrins tend to localize at the leading edge of motile cells, where actin filament polymerization and fiber formation result in various protrusions. Activated Rac1 and Cdc42 induce reorganization via WAVE and WASp proteins, which activate Arp2/3 complexes, pushing the membrane forward in filopodia and lamellipodia, dorsal ruffles, podosomes, or invadopodia. Simultaneously at the trailing edge, activated Rho promotes myosin-dependent contraction[113].

Single cell motility is typically classified into two principle modes: mesenchymal and amoeboid. It is important to acknowledge that cell motility may fall anywhere on the continuous spectrum between these two modes, depending on cell mechanical properties (size, deformability, and contractility), ECM conditions (pore size, stiffness, and composition), and CSK signalling events[114,114,115]. For example, normal mammary epithelial cells were shown to establish acute, elongated protrusions in collagen I matrix but not in Matrigel[116]. Normal mammary epithelial cells cultured on

stiff (E = 4.5 kPa) matrix exhibit increased proliferation and ERK signalling and altered polarity, adopting a more malignant phenotype[117,5,4].

Mesenchymal motility is exhibited by cells with an elongated morphology, and amoeboid motility is exhibited by cells with a rounded morphology. Mesenchymal migration requires integrin-mediated adhesion, and in 3D, proteolysis. Cells can degrade matrix fibers via proteolysis. Proteolytic factors (PFs) secreted into the ECM degrade diffusively. Other PFs are membrane bound and degrade matrix only in the local vicinity of the leading edge ("contact-dependent proteolysis"). Yet more degradation takes place inside lysosomes in the cell[108].

Amoeboid migration is based on contractility alone and does not depend on proteolysis or adhesion, and occurs in cells lacking mature focal adhesions or stress fibers[114]. Independent of proteolysis, cells traverse ECM by deforming the cell body and nucleus, actomyosin-mediated pushing, or reorientation of protrusions to bypass obstacles. Myosin light chain (MLC) is organized perpendicularly to the direction of movement, behind the leading edge in a ROCK-dependent fashion, enabling migration through dense matrix even when proteolysis is inhibited with a broad spectrum MMP inhibitor (GM6001)[118]. There are 2 subtypes: blebby amoeboid motility and filopodial amoeboid motility (in the latter, cells with actin-rich filopodia at the leading edge engage in poorly defined, weak adhesive interaction with the substrate)[114]. Amoeboid migration is exhibited by normal lymphocytes and neutrophils, as well as cancer cells, which can switch between amoeboid and mesenchymal migration, or collective cell migration[113].

In addition to single cell motility, cancer cells are known to sometimes undergo collective cell migration. MDA-MB-231 cells co-cultured with MCF-10A cells in spheroids embedded in collagen I exhibit collective cell migration; the metastatic cells function as leader cells, remodeling and blazing a trail through the matrix. Intriguingly the non-motile and non-tumorigenic MCF-10A cells followed these leader cells along microtracks through the matrix, but did not invade the matrix in the absence of the MDA-MB-231 cells[119].

This has important implications for the EMT-MET paradigm of metastasis: EMT is often thought to be a necessary condition for metastasis, but perhaps it is essential that only a subpopulation in a tumor undergoes EMT. In another study, transformed cells acted as leader cells and non-EMT cells acted again as follower cells in collective cell migration. After migration, the mesenchymal leaders could not successfully extravasate and metastasize a distal site, but the epithelial follower cells could[120].

Effects of matrix and substrate stiffness on normal and cancer cells

In the last five years or so, many studies have been conducted which reveal that substrate or matrix stiffness have a variety of effects on cell growth, morphology, motility, adhesion, stiffness, differentiation, phenotype in various cell types. Spreading area, stress fiber formation, and focal adhesion complex formation of fibroblasts on soft collagen gels are all modulated by substrate stiffness[121]. The substrate stiffness sensitivity of fibroblasts' spreading, contracility and adhesion depends on growth factors[122]. Human colon carcinoma cells adopt a malignant phenotype on soft PA gels, but not on soft collagen gels[121]. On soft (0.4 kPa) PA gels, Swiss 3T3 fibroblast nuclei are round, while on stiff gels, they are flattened[123].

Fibroblast cell stiffness was shown to increase with PA gel stiffness[124]. Aortic valve interstitial cells (VICs) grown on PA gels ranging from 3-144 kPa were indented with pyramidal and spherical AFM probes; with both probes the apparent Young's moduli of the cells increased monotonically with substrate stiffness[125]. Filamin A-replete A7 melanoma cells match collagen substrate stiffness, whereas filamin A-null M2 melanoma cells do not[126]. In Schwann cells, adhesion, morphology, cytoskeletal architecture and neurotrophic activity are all modulated by substrate stiffness[127]. Human mesenchymal stem cells (HMSCs) exhibit a decrease in ROCK-dependent spontaneous Ca^{2+} oscillations in the cytoplasm on softer substrates[128]. HMSC spreading area and cell stiffness were also shown to increase as a function of substrate stiffness[129]. Undifferentiated mouse embryonic stem cells were shown to exhibit increased traction forces on increasingly stiff collagen I-coated polyacrylamide gels, but the cell stiffness did not vary[130]. Increased beating rate, focal adhesions, and sarcomeric striations were observed in embryonic chicken cardiac myocytes cultured on increasingly stiff laminin-coated PA substrates[131]. Intracellular particle tracking microrhology experiments on PC-3 metastatic prostate cells on 2D and in 3D collagen I matrices revealed that on 2D subtrates, Brownian dynamics of tracer beads (and thus cell stiffness) did not vary with substrate stiffness; in 3D gels, the cell stiffness decreased with increasing gel stiffness[132].

Conferring to normal epithelial cells the ability to invade 3D ECMs

Normal epithelial cells are unable to invade 3D ECMs. However, they can be made to do so under certain conditions. Overexpression of MT1-MMP or MT2-MMP confered MDCK cells the ability to invade collagen matrices[133]. Expression of

gelsolin-GFP promotes invasion into collagen I matrices in MDCK and HEK293T cells in a PI3K-Rac dependent manner[134]. MCF-10A cells with provided with exogenous acitvated MMP2 can cleave and migrate on Laminin 5 surfaces[135]. Knockdown of giant obscurins in MCF10A cells confers increased directional migration and invasion into Matrigel[136]. BMI1 and H-RAS, but not N-RAS, expression in MCF10A induces lung metastases in mouse tail vein xenografts [137,138].

2.3 Cell Mechanics Measurement Techniques

In the context of the sections above, it is clear that mechanical forces in general have great influence on both normal physiology and pathological cancer progression. Dynamic reorganization of the cytoskeleton and generation of endogenous contractile forces are regulated by the mechanosensation of tension transduced through focal adhesions. External mechanical forces can induce front-rear polarization and motility.

In 1702, Leeuwenhoek described the motion of the ciliate *Vorticella*. He and other early researchers (like Hooke) knew it was possible to estimate the viscosity from particle motions but lacked the technology[77]. Since then, many different experimental techniques have been developed to probe mechanical properties of single cells[139,20]. For a historical perspective, see[77].

A number of different experimental methods have been applied to investigate mechanical properties such as traction and especially the elasticity (or viscoelasticity, viscoplasticity, elastoplasticity, etc.) of cancer cells of many types (for a

comprehensive review see[20]). This growing body of experimental studies has associated cancer with aberrant cell mechanics, including active force generation and passive viscoelasticity. This is a rapidly growing research area as evident in the number of publications per year with topic 'cancer stiffness' (Fig. 2.2). The following section introduces some of the current methods, highlighting quantitative measures of cancer cell mechanical properties.

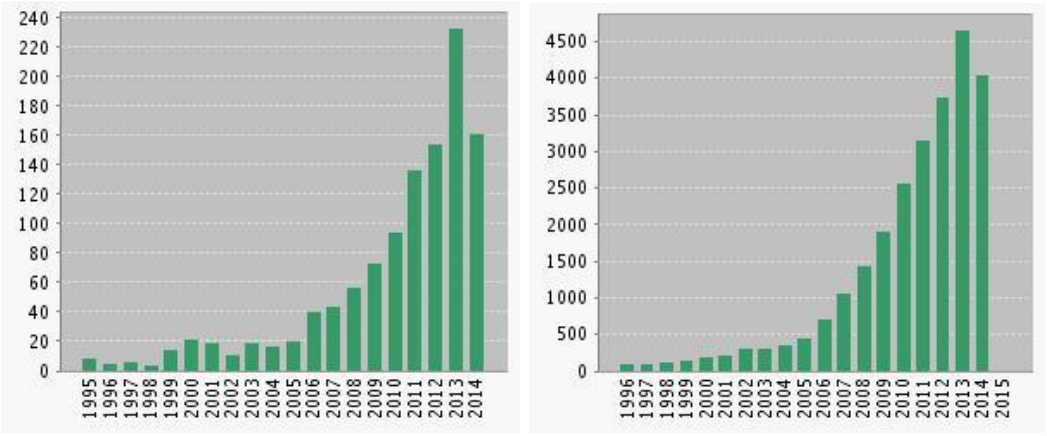


Figure 2.2: Web of Science Bibliometric Data. Accessed Nov. 2014. Number of papers published (left) and cited (right) per year with topic 'cancer stiffness'.

One method of measuring active mechanics is traction force microscopy, which can determine acto-myosin contractility based endogenous traction forces generated by migratory mesenchymal or cancer cells in dense 3D matrices. If the matrix elasticity is known, then these forces can be determined by measuring the displacement of fluorescent beads tightly embedded in the matrix in the local vicinity of migrating cells. Finite element simulations can be used to calculate the strain energy associated with the bead displacements. (These quantifications require treating the ECM as a

continuum- an assumption which may not apply particularly well to gels with relatively large pore size.)

On soft (118 Pa) 3D collagen gels, MDA-MB-231 cells produced strain energies of ~0.75 pJ, while non-invasive MCF7 cells were ~0.3 pJ; cell shape anisotropies were ~1.5 for MCF7 and 10 for MDA-MB-231; strain energy anisotropies were ~1.75 for MCF7 and 2.5 for MDA-MB-231. Therefore in addition to the magnitude of traction forces, cell shape and the directionality of applied forces may be essential for cancer cell invasion[140]. In another work, MDA-MB-231 cells exerted traction forces of 300-400 nN on laminin substrates; MCF-10A cells exerted forces ~20-100 nN[22].

Similarly, cells can be seeded on micropatterned arrays of elastic pillars. This method is suited for measuring tension in epithelial sheets, for example. Traction forces are determined by optically measuring the deflection of pillars in contact with cells. The force is related to the deflection by Hooke's law, with a correction factor incorporating the relative contributions of shear, tilting (i.e. substrate warping) and bending of the pillar deflection, which depend particularly on pillar length[141]. Typical forces for non-cancerous cells are again in the range 0-100 nN. This method has been applied (albeit somewhat qualitatively) to investigate the influence of the cancer therapeutic emodin on MDA-MB-231 cell traction, revealing increased traction at low concentrations and decreased traction at higher doses[142].

The primary non-perturbative method of probing the passive mechanics of the cell is by particle tracking microrheology, introduced by the Wirtz group[143] (for an extensive recent review see[144]). Local viscoelastic properties of a living cell can be probed by the analysis of the movement of sub-micrometer sized fluorescent beads

injected into the cell. This technique allows simultaneous measurement of local mechanical properties with high spatial resolution at different places inside the cell.

The diffusion constant D of a bead undergoing a two-dimensional (2D) random walk is related to its mean square displacement (MSD) $\langle \Delta r^2 \rangle$ and time lag t by[145]:

$$\langle \Delta r^2 \rangle = 4Dt \tag{1}$$

and by the Stokes-Einstein relation (for a sphere), D is equal to[145]:

$$D = \frac{k_B T}{6\pi\eta a} \tag{2}$$

where k_B is Boltzmann's constant, T is the absolute temperature, η is the fluid's viscosity, and a is the bead's radius. Combining Eqs. (1) and (2) yields the viscosity (in a purely viscous liquid):

$$\eta = \frac{2k_B T}{3\pi a} \frac{t}{\langle \Delta r^2(t) \rangle} \tag{3}$$

or the elastic shear modulus G' (in a purely elastic solid, for which the MSD has no time dependence):

$$G' = \frac{2k_B T}{3\pi a \langle \Delta r^2 \rangle} \tag{4}$$

In the case of a viscoelastic medium, the complex shear modulus $G^*(\omega)$ is related by a unilateral Fourier transform of the mean square displacement $F_u[\langle \Delta r^2(t) \rangle]$, with $i = \sqrt{-1}$ and frequency ω:

$$G^*(\omega) = \frac{2k_BT}{3\pi a i \omega F_u[\langle \Delta r^2(t) \rangle]} \quad (5)$$

assuming shear stress relaxation near particles is identical to that of bulk fluid in a perturbing shear strain, which is valid when the length scales of heterogeneity of discrete structures in the fluid are much smaller than the particle[146].

The beads' motions depend on the viscosity of the cytoplasmic medium, the rigidity of cytoskeletal fibers in their immediate vicinity, on the size of the confining "mesh" these fibers form around them, and on whether the beads have any binding affinity to any structures in the cell. Therefore bead size and ligand coating are critical to the measurements. Active processes in the cell mediated by motor proteins may confound the results if bead motion is not truly diffusive.

The average elasticity at 1 Hz calculated by this method for a number of cell types falls in the range of 50-600 dyne/cm^2 (5-60 Pa)[144]. MDA-MB-231 cells have a significantly higher MSD than MCF-10A cells, indicative of a less viscous cytoplasm and/or more compliant cytoskeleton[22].

Other optical methods exploiting diffusive motion of particles in a medium to characterize the medium's material properties include dynamic light scattering (DLS) and diffusing wave spectroscopy (DWS). In DLS, the MSD (and thus material properties of the medium) can be determined from the intensity autocorrelation function if other system properties are known (e.g. the scattering angle, refractive index, and coherence factor). The approach has been used quantitatively to characterize *in vitro* reconstituted F-actin gels, but cannot be used inside cells due to the complex scattering off many heterogeneous surfaces[49]. A quasi-quantitative

method called partial wave spectroscopy (PWS) measures spatial variations of refractive index inside cells; this data then informs a model that describes the degree of disorder in the nanoscale architecture (e.g. the surface roughness of the nucleus). MDA-MB-231 cell nuclei were found to have an average disorder strength 80% greater than MCF-10A cells[22].

Beads can also be used in perturbative or active microrheology to measure viscoelasticity. In this case, the motions of magnetized beads excited by an external magnetic field can be tracked. In fact this may be the oldest quantitative cell mechanics method. Freundlich and Seifriz developed an early apparatus in 1923. Microneedles were used to inject magnetic microparticles into a sol, gel, colloidal substance, or a cell. An electromagnet applied a force on the particle(s), and under the microscope the resulting particle displacement was measured. From the force-displacement relation the material mechanical properties were determined. By 1950, Crick and Hughes improved upon Seifriz' design by magnetizing the particles in a strong field but then perturbing with a weaker, twisting field; additionally they studied cells that could phagocytose the particles, avoiding the cell's alteration or any damage potentially caused by microneedle injection[49].

The modern version known as magnetic twisting cytometry (MTC) was developed by the Ingber group in 1993[147]. In MTC, ferromagnetic beads (ranging in size from ~50 nm to ~5 μm) are coated with a ligand known to bind to the cell membrane[148]. The beads are then attached to the cell surface, and subsequently magnetized with a strong pulse, inducing a magnetic moment at an angle $\sim\pi/4$ from the vertical. A weak sinusoidally oscillating vertical magnetic field is then applied, which exerts a

rotatory torque on each bead. A magnetometer measures the magnetic field, which changes due to the beads' rotation. Correlated and random noise are decoupled from the signal by demodulation. Demodulation is accomplished by spinning the sample about the vertical at a rate that is phase-locked to a reference signal; the reference signal is then multiplied by the magnetometer signal, and the product signal is low-pass filtered[149]. Frequencies can be applied across several decades. The response and drive signals are compared to find the phase angle δ, the shear storage modulus $G'(\omega)$, and the shear loss modulus $G''(\omega)$. The method can be combined with FRET or other optical techniques[150]. Heterogeneities in the details of the attachment of beads to the cell surface can confound measurement of cell mechanical properties[151].

Human airway smooth muscles (HASM) cells measured by this method were shown to obey a weak power law, by which G' increases with increasing frequency f as $G' \sim f^{x-1}$ with x in the range ~1.15-1.35, and f in the range 10^{-2}-10^{3} Hz[152]. This behavior held even for cells treated with CSK modulating drugs; in untreated cells, G' ranged from ~1-10 kPa; cells treated with cytochalasin D were about an order of magnitude softer. G'' behaved similarly below 10 Hz, increasing more rapidly thereafter. For untreated cells, G'' was ~300 Pa at 10^{-2} Hz and 1 kPa at 10 Hz; in cells treated with cytochalasin D, G'' was ~50 Pa at 10^{-2} Hz and ~300 Pa at 10 Hz. Interestingly, above this frequency G'' converged to ~10 kPa at ~10 kHz for all treatment conditions. By invoking a structural damping model, the authors showed that once the data is scaled in a particular way, the data from a number of different

cell types and conditions fall onto master curves[152]. The same structural damping law fits well to data in other MTC studies[149], and also in a dynamic AFM study[153].

Yet another method is the optical stretcher developed by Käs *et al.*, which is based on optical trapping methods[13]. The optical stretcher consists of two opposed, slightly divergent and identical beams with Gaussian intensity profiles. If a cell has a refractive index exceeding that of the medium and is smaller than the beams, it will experience a stable restoring force inside the trap. Momentum transfer occurs mainly at the cell surface; while the total force acting on the center of mass is zero, the forces acting on the surface are additive, and capable of stretching sufficiently elastic objects along the beam axis[154]. Since the refractive indices of different cells are nearly identical, the optical deformability itself can be equated with compliance[155]. Cells can be trapped with power ~10 mW, and deformed with power as much as 500 mW. The forces applied are ~1-50 pN. Stresses can be calculated using a ray optics model and are of order ~1 N/m^2. Calculating the forces and relating them to the optically measured deformation can then yield mechanical moduli.

Incorporated in a microfluidic platform, an optical stretcher measured the optical deformation of MCF-10A, MCF7, and TPA (a phorbol ester known to enhance metastatic invasion) -treated MCF7 cells. The populations were distinct at the 99.9% confidence level, with deformability increasing with malignancy[155]. Recently, Guck *et al.* applied this method to the diagnosis of oral cancer[156]. In another study, MCF7 cells were found to have an elastic modulus ~18 ± 24 Pa, and a viscosity of 181 Pa·s. In the creep compliance model used, $J(t) = J_0(t/\tau)^{\beta}$, the power law exponent β was found to be ~0.87. This value of elastic modulus is in agreement with particle-

tracking results. Importantly, both of these methods give values 1-2 orders of magnitude lower than those measured by other techniques (AFM, rheometer, parallel plates).

Application of such microfluidics-based (opto-fluidic) approaches to single cell mechanical analysis and high throughput mechanical phenotyping has increased rapidly in the past few years. These methods are well suited to probe properties of metastatic tumor cells in the circulation, but not those of cells that have not yet intravasated.

More straightforward methods use direct mechanical perturbation. A conventional rotational rheometer mounted on an optical microscope is capable of applying shear stresses and measuring shear deformations on populations of cells, engineered or explanted tissues. The cells are allowed to adhered to a substrate, typically glass functionalized e.g. with fibronectin. Sinusoidal strain oscillations with amplitude sweeps, frequency sweeps, as well as stress relaxation, recovery and creep experiments can be conducted with this configuration.

This method has the characteristic of averaging over many cells in a population (sub-confluent or confluent; ~50,000 – 10^6 cells); it thus cannot account for interpopulation heterogeneity, but on the other hand it has higher statistical significance with less variation in the data. Rheometers measure engineered or explanted tissues and can even be integrated into a bioreactor[157]. Furthermore, measured cells and other biomaterials can be more readily compared to other materials that are commonly measured by the same instrument. The results depend

on the amount of pre-stress or compression at which the oscillations are performed, as well as the duty cycle of the oscillations.

Other rheometry apparatus specialize in uniaxial stretching or compression. In the uniaxial stretch rheometer (a.k.a parallel plate rheometer), a living cell is stretched between two borosilicate glass microplates, one rigid and one flexible, which is calibrated to get the force-deflection relation. The deflection is determined via optical microscope. This device was used to measure the creep function $J(t)$ (i.e. the strain observed for a step stress, normalized by the constant stress value) of C2-7 mouse myoblasts, which obeyed a power law $J(t) = At^{\alpha}$, with α = 0.24 and A = 2.4 10^{-3} $Pa^{-1} \cdot s^{-\alpha}$ [158]. This is in good agreement with oscillating AFM (α ~0.2 for A549 and BEAS-2B cells[153]) and MTC (α ~0.16 – 0.33 for different cell types and biophysical treatments[152]). The corresponding storage moduli G' at 1 Hz is also in good agreement (660 Pa[158]; ~710 Pa[153]; 300-3000 Pa[152]).

One of the older apparatus is the cell elastimeter, developed by Mitchison and Swann in 1954[159]. The Young's modulus of the sea urchin egg was estimated to be 0.5-1.0 kPa. This method has since evolved into what is now called micropipette aspiration (MPA). MPA was used by Ward *et al.* to show that cells transformed with Ras-T24 oncogene (exhibiting increased tumorigenicity) had increased deformability[18].

2.4 Atomic Force Microscope Based Indentation

McConnaughey and Petersen introduced the cell poker in 1980[160]. This device was later surpassed by the atomic force microscope, which can be used (among very many other things) as an indenter. This section will cover the method in detail.

2.4.1 Principles of Atomic Force Microscopy

The atomic force microscope (AFM) is a scanning probe microscope (SPM) invented by Binnig, Quate and Gerber in 1986[161] as an adaptation of the scanning tunneling microscope (STM) developed by Binnig and Rohrer[162]. AFM allows the application and measurement of forces in the piconewton to micronewton range between a small probe and a substrate, and measurement of the corresponding indentation depth with nanometer accuracy[161].

The AFM probe consists of a cantilever at the end of which is a sharpened tip. The cantilever and tip are typically silicon (Si) or silicon nitride (Si_xN_y). Common probes are made with traditional semiconductor manufacturing techniques such as photolithography, as well as isotropic and anisotropic wet and dry chemical etching, and chemical vapor deposition. More expensive methods such as focussed ion beam milling, electron beam induced deposition, magnetic functionalization and diamond coating are used on tips intended for specialized applications. Standard probes have cantilevers ranging in length ~50-200 μm; high-speed tapping mode probes have ultra-short cantilevers with resonance frequencies in the MHz range.

When the tip is brought into close proximity with a sample surface, various interactions may occur between them, resulting in the tip's attraction to or repulsion from the sample surface. The forces of these interactions result in the tip moving toward or away from the surface. This displacement consequently bends the cantilever through an angle α.

The bending angle is itself measured by aiming a beam of light from a low-power diode laser at the back of the cantilever, which reflects the beam into a

photodetector array. The photodetector array is separated into four quadrants (for both normal and lateral deflection). The intensity incident on each quadrant (measured as deflection in volts, deflVolts) depends on the optical beam angle, which itself depends on the bending angle α. The optical beam angle is related to the bending angle by the inverse optical lever sensitivity (InvOLS), which must be calibrated any time the beam is aligned or moved. This is accomplished by pressing the probe against a rigid substrate such as glass. Since the glass is not deformed, the deflection is directly proportional to the vertical displacement of the fixed end of the cantilever (Z position). The reciprocal of slope of the deflVolts vs. Z position gives the inverse optical lever sensitivity (InvOLS), $\Delta z/\Delta V$ (nm/V). With InvOLS known, the bending angle from indentations on other surfaces can then be found. The cantilever bending angle is low ($\sin\alpha \sim \alpha$); it is used to determined the vertical displacement of the free end of the cantilever, i.e. the deflection in nm. This deflection is then considered to be directly proportional to the force applied to the probe by the sample, with the constant of proportionality being the cantilever's spring constant.

The cantilever can be approximated simply as having a linear response to this perturbation according to Hooke's law of elasticity:

$$F_z = -k_s \Delta z \tag{6}$$

where k_s is the (normal) spring constant, Δz is the displacement of the cantilever's free end from mechanical equilibrium, and F_z is the force applied in the direction z resulting in the displacement. A cantilever undergoing small oscillations can be

(roughly) approximated by a simple (undamped) harmonic oscillator with the Hamiltonian H:

$$H = \frac{p^2}{2m} + \frac{1}{2}m{\omega_o}^2(\Delta z)^2 \tag{7}$$

where m is the cantilever's effective mass, ω_o is its resonance frequency (in vacuum), and p is its momentum. Setting

$$\omega_0 = \sqrt{\frac{k_s}{m}} \tag{8}$$

with k_s the cantilever's spring constant, gives k_s by substitution into the equipartition theorem, which equates the average elastic energy $\frac{1}{2}m{\omega_0}^2\langle(\Delta z)^2\rangle$ to the thermal energy $\frac{1}{2}k_BT$ per degree of freedom:

$$\frac{1}{2}k_BT = \frac{1}{2}m{\omega_0}^2\langle(\Delta z)^2\rangle \tag{9}$$

where k_B is Boltzmann's constant, T is the absolute temperature, and $\langle(\Delta z)^2\rangle$ is the mean square displacement of the free end of the cantilever from mechanical equilibrium, yielding [163]:

$$k_s = \frac{k_BT}{\langle(\Delta z)^2\rangle} \tag{10}$$

This approach is used in the thermal noise method for finding the cantilever spring constant. However the cantilever is not exactly an ideal spring, and the result can be improved by adding correction factors as discussed by Hutter[164,165,166]:

$$k_s = 0.8174 \frac{k_B T}{s^2 P} \left[\frac{1 - \left(\frac{3D}{2L}\right) \tan \phi}{1 - \left(\frac{2D}{L}\right) \tan \phi} \cos \phi \right]^2 \tag{11}$$

where s is the optical lever sensitivity calibration factor (in m/V), P is the positional noise power in the fundamental resonant mode (in V^2), D is the tip height, L is the cantilever length, ϕ is the tilt angle of the cantilever, and the numerical factor is derived from the cantilever's geometry. The power P is measured by recording the cantilever deflection in time as it is perturbed by thermal fluctuations, and Fourier transforming from the time domain to the frequency domain. The resulting power spectrum gives the amplitude of fluctuations as a function of frequency; thermal noise from external sources (e.g. at 60 Hz) can be subtracted, with the integral of the remaining power spectrum equalling the mean square fluctuations $\langle (\Delta z)^2 \rangle$, which is equivalent to the power P of the cantilever fluctuations[164,167]. The resonance frequency ω_0 and the quality factor Q are also determined by fitting the power spectrum.

One alternative approach is Sader's method, in which k_s is determined directly from the resonance frequency and the cantilever mass. The resonance frequency is determined from the power spectrum as in §2.4.4. The mass is determined by multiplying the volumetric mass density by the cantilever's volume (which itself is

determined by multiplying the plan view dimensions of the cantilever). Another approach is to indent a reference material of known stiffness; indenting a set of reference materials provides a more accurate determination of the spring constant[168]. Other methods include obtaining the noise spectrum from forced oscillations, or static loading using one probe to calibrate another; each method has advantages and disadvantages[169].

2.4.2 Indentation Force-Depth Curves

It is possible to extract quantitative information about the mechanical properties of a material by indenting the material with the AFM probe. Sharp tips probe local mechanical properties with high spatial resolution. Larger tips average out local heterogeneities, probing mechanics at a greater length scale, such as the global properties of a cell[170,171]. The atomic force microscope was first applied as an indenter to probe mechanical properties of cells and other biological materials in the 1990s[172,173,174,175]. Since then the method has seen increased use and applications. For reviews of AFM nanoindentation measurements of cell elasticity, see[176,177,178].

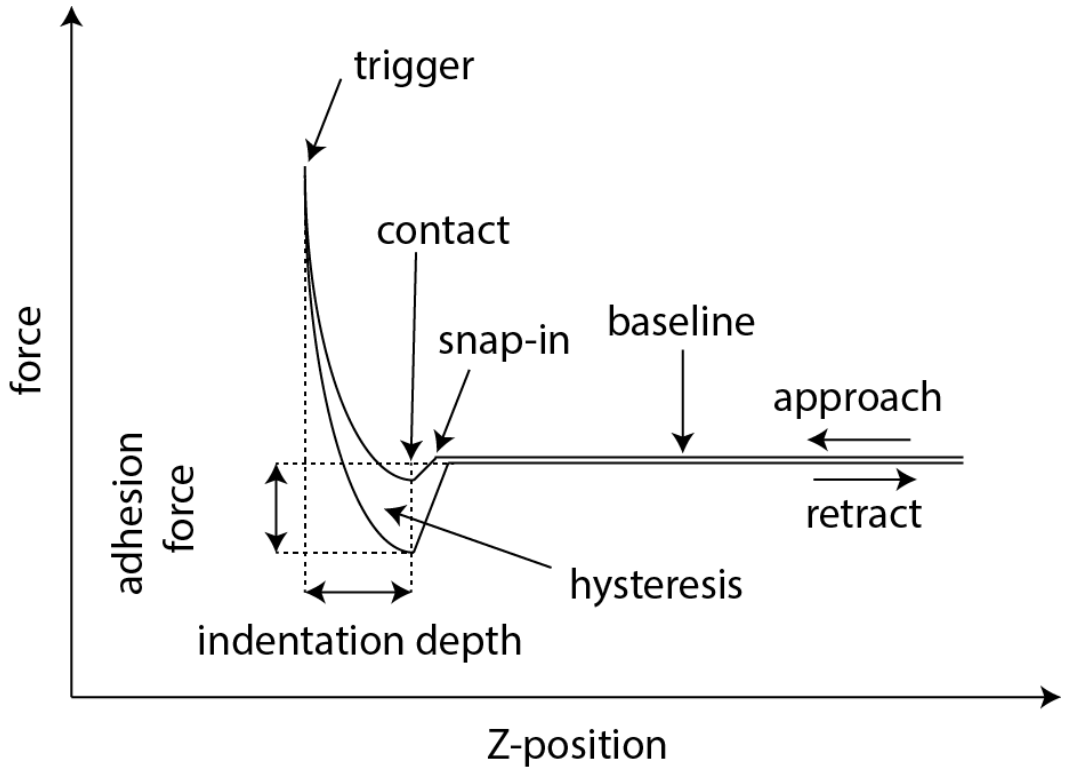


Figure 2.3: Anatomy of an Indentation Force-Depth Curve.

The (relative) depth of the indentation is determined by subtracting the displacement of the free end (deflection) from the displacement of the fixed end (Z-position). To get the absolute value of the indentation depth, the relative value at the point of first contact is subtracted from each data point, so it equals 0 at the undeformed surface. The indentation force is determined by multiplying the deflection by the spring constant. These data can then be plotted as an indentation force-depth curve (force curve).

A typical force curve has a number of features that indicate information about the tip-sample interaction (Figure 2.3). The horizontal section of the curve corresponds to the lowering of the tip from far above the surface, where there is no tip-sample

interaction. The absolute force on the cantilever is nominally zero here. As the tip is brought closer, it eventually gets pulled toward or pushed away from the sample by attractive or repulsive forces. When the tip is brought into direct contact with the sample, it typically "snaps in" as a result of the attractive dipole-dipole van der Waals interactions that dominate at this distance scale. As the cantilever is pushed further down into the sample, the slope of the extension curve typically increases as the tip meets more resistance, until the trigger value is met. After the trigger is met, the cantilever is lifted away from the surface by the z-piezo. Typically, relatively strong adhesive forces between the tip and sample must be overcome before the tip snaps off the surface, resulting in a dip in the curve. After the tip breaks contact with the sample, there are again no interactions, resulting in a horizontal line that moves back to the right until the force-distance is reached.

Together with the indenter geometry, force curves can be used to find the Young's modulus of the material[179]. This requires fitting the data to a theoretical model.

2.4.3 Elastic Contact Models

The simplest theoretical models of such indentations are taken from linear elasticity theory and classical infinitesimal strain theory. In these models, the indented material is treated as a homogeneous, isotropic, and perfectly elastic (i.e. their deformations are perfectly reversible) body approximated by a half-space (i.e. the contact area is small compared to the body's total surface area). The indenter is assumed to be perfectly rigid. The depth of the deformation is assumed to be much less than the size of the bodies (i.e. in the limit of infinitesimally small strains)[180]. The surfaces are also assumed to be continuous, frictionless and non-conforming[181].

For a given axisymmetric indenter, the Poisson's ratio and Young's modulus of the indented material are related to the indentation force and depth by a function that depends on the indenter shape[182]:

$$F = g\frac{E}{(1-\nu^2)}\delta^n \tag{12}$$

with $1 \leq n \leq 2$ and g and n depending on the indenter shape.

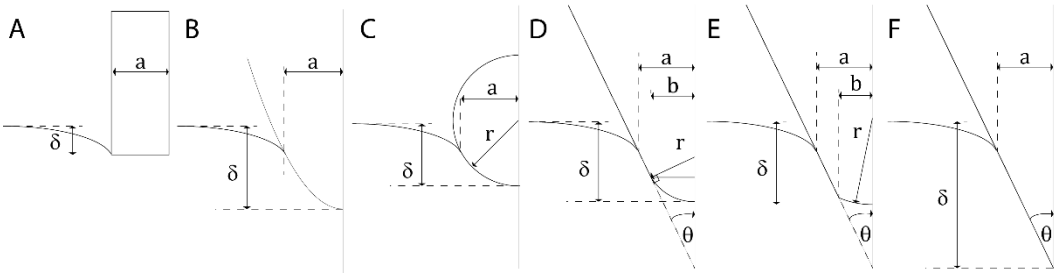


Figure 2.4: Indenter Geometry. A) cylinder; B) paraboloid; C) sphere; D) cone smoothly merging with spherical tip ("spherocone"); E) cone with spherical defect; F) cone.

$$F_{cylinder\ of\ radius\ b} = 2b\frac{E}{(1-\nu^2)}\delta \tag{13}$$

$$F_{Hertz} = \frac{4}{3}r^{1/2}\frac{E}{(1-\nu^2)}\delta^{3/2} \tag{14}$$

$$F_{cone\ of\ semi-vertical\ angle\ \theta} = \frac{2\tan\theta}{\pi}\frac{E}{(1-\nu^2)}\delta^2 \tag{15}$$

The relation for a sphere is written in terms of the contact area, a (which is a function of the indentation depth δ and solved for numerically). The relation for a cone with a spherical defect at the apex is written in terms of the contact area, a, and

the transition radius, b (which is a constant describing the tip geometry). In the special case of a cone with a spherical defect at the apex which merges continuously and smoothly with the cone (i.e. "spherocone"), the transition radius $b = r\cos\theta$.

$$F_{\substack{sphere\ of\ radius\ r,\\ contact\ radius\ a}} = \frac{E}{(1-\nu^2)}\left[\frac{1}{2}(a^2+r^2)\ln\left(\frac{r+a}{r-a}\right) - ar\right] \tag{16}$$

$$F_{\substack{blunted\\ cone}} = \frac{2}{\tan\theta}\frac{E}{(1-\nu^2)}\left\{\delta a\tan\theta - \frac{a^2}{2}\left[\frac{\pi}{2} - \sin^{-1}\frac{b}{a}\right] + \frac{b}{2}(a^2-b^2)^{1/2}\right\} \tag{17}$$

$$F_{spherocone} = \frac{E}{(1-\nu^2)}\left[a^2\cot\theta\cos^{-1}\left(\frac{b}{a}\right) + b\cot\theta\sqrt{a^2-b^2} - ar + \sqrt{(r^2-b^2)(a^2-b^2)} + a^2\ln\left(\frac{r+a}{\sqrt{r^2-b^2}+\sqrt{a^2-b^2}}\right) - \frac{r^2}{2}\ln\left(\frac{a^2r^2 - \left(b^2 - \sqrt{(r^2-b^2)(a^2-b^2)}\right)^2}{b^2(r+a)^2}\right)\right] \tag{18}$$

The force relations given for the blunted cone (Eq. 17)[183] and spherocone (Eq. 18) above are applicable in the regime of indentation in which $a \geq b$ (i.e. beyond the sphere-cone transition point); before this point, the relation for a sphere of radius r (Eq. 16) holds instead. The Hertz model[184] describes the contact for a paraboloid indenter, but due to its simplicity, it is frequently used to model the contact for a

spherical indenter; this is appropriate only for shallow indentations $\delta \leq \sim \frac{r}{6} - \frac{r}{3}$, where the curvature of the sphere is very similar to the paraboloid. The conical indenter model[182] is frequently used for indentations with sharp AFM tips. AFM tips are generally not conical, but rather pyramidal; the model can be used with reasonable accuracy if an effective cone angle is used, for which the contact area of the cone and the pyramid are equivalent (Doss *et al.*, in preparation).

Poisson's ratios for cells have been reported between 0.4-0.5[185]. Most frequently, cells are taken to be purely incompressible ($\nu = 0.5$). Given the Poisson's ratio, these equations can be used to find the Young's modulus from the force-depth curve recorded during the indentation.

The models above apply to a half-space, with no rigid boundary condition corresponding to the attachment of the finitely thick elastic layer to a rigid substrate (such as glass). For thin samples such as areas in cell lamellopodia, there are analytical and computational methods to calculate the effect of an underlying rigid substrate. Mahaffey *et al.* used such a modified Hertz model to get storage and loss moduli of adhered and non-adhered thin regions of cells[170]. Furthermore, the underlying layer need not be rigid; Dhaliwal and Rau derived the equations of contact between an indenter of arbitrary shape and a finitely thick elastic continuum bounded to a second, underlying infinitely thick elastic continuum, each with finite Young's modulus and Poisson's ratio[186]. A two-layer model of this form is applied in §3.6 to find the Young's moduli of cells partially embedded in collagen matrices.

Since adhesion between the sample and indenter affects the contact area and thus the load distribution, it is important to factor this in to get the correct moduli.

Elaborations on the models above that account for adhesion include the Johnson-Kendall-Roberts (JKR), Derjaguin-Muller-Toporov (DMT), and Maugis-Dugdale models[187].

2.4.4 Modeling with Finite Element Simulation

As described in[49], in finite element models, the cell is broken up into a number of small elements, and each element is treated as a continuum with boundary values in agreement with those of its neighbors. Each element can have its own unique geometry, and its own unique stress and strain tensors, so long as the boundary conditions are met. Modern finite element models use computational and numerical methods, and can therefore achieve high resolution. However, the resolution is limited by the length scale at which the mechanical properties of the cell are no longer well-approximated by the stress-strain relations from continuum mechanics. Because the actual macromolecular components of the cytoskeleton are discrete, finite element methods can be applied reasonably only down to length scales in the 100s of nm.

Simulated indentations of materials in finite element models can yield pointwise coordinate solutions of the indentation force-depth curve. The curve can then be fit to an appropriate model to find the Young's modulus. The found modulus can then be compared to the value of the Young's modulus assigned to the material in the simulation. This approach can be used to evaluate different theoretical models in various circumstances, e.g. at high strains, with a modified indenter geometry, or for a substrates with different constitutive equations[180]. In addition, the simulated curve can be compared to experimental curves on a sample with mechanical properties

similar to those of the modeled material. The modeled material can then be modified iteratively until the simulated and experimental indentations match sufficiently well to characterize the sample. This approach is applied in §3.6 to find the Young's moduli of cells fully embedded in collagen matrices.

2.4.5 Confocal Microscopy and Fluorescence Lifetime Imaging

The confocal microscope (patented by Minsky in 1957) uses point illumination (such as the point spread function of a focussed laser beam) and an aperture (the confocal pinhole) to improve the optical contrast beyond that of the widefield illumination microscope. The aperture blocks from the detection path any light not originating in the focal plane, reducing the lateral and axial dimensions of the ellipsoidal intensity point spread function each by ~30%. Lateral resolution $r_{lateral}$ (by Rayleigh's criterion) in ideal the confocal microscope is $r_{lateral} = 0.4\lambda/NA$, where λ is the wavelength and NA is the numerical aperture of the objective. Axial resolution r_{axial} is $r_{axial} = 1.4\lambda\eta/NA^2$ with η the index of refraction of the medium[188]. This improved axial contrast enables optical sectioning and the construction of 3D images.

A fluorophore placed in an excited state by absorption of a photon may lose this energy through a number of radiative and/or non-radiative decay pathways, including spontaneous emission of a photon (fluorescence). Each decay pathway has a characteristic rate k_i. In an ensemble of fluorophores obeying Poisson statistics, the intensity $I(t) = I_0 e^{-t/\tau}$, where $I(t)$ is the intensity at time t, I_0 is the initial intensity, and $\frac{1}{\tau} = \sum k_i$, with τ the fluorescence lifetime, which is independent of the

initial intensity or the intensity of the emitted light[189]. Specialized fluorophores can be used to quantitatively probe e.g. pH or ion concentrations by observing changes in their fluorescence lifetimes[190].

3. RESULTS & DISCUSSION

3.1 Combined AFM-CLSM Measurements

The primary experimental method used in this dissertation is atomic force microscope based indentation combined with confocal fluorescence microscopy. This approach enables the force data to be spatially co-located with the fluorescence data, so that the elasticity values from each part of the imaged sample are known. This section will introduce this method and the experimental apparatus, which is applied in the following sections.

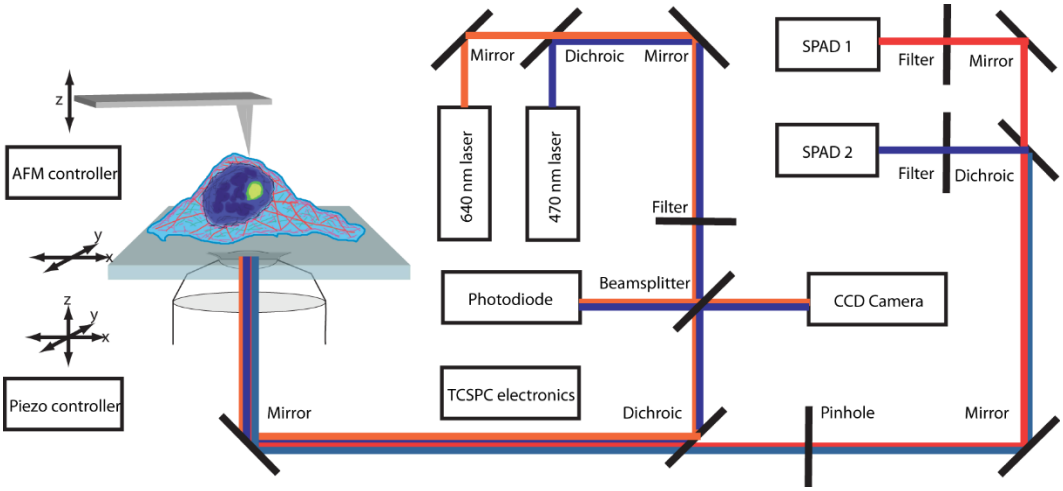


Figure 3.1: Experimental AFM-CLSM Setup. The AFM probe tip is aligned with the laser focus using the diffraction pattern from backscattered laser light on the CCD camera. Once aligned, the probe is retracted and the sample is imaged with multicolor CLSM. The region of interest can then be indented.

The sample and the Asylum Research MFP3D-BIO AFM head are mounted on a micrometer stage. The sample is mounted on a lateral (XY) piezo stage that can move sample with respect to the probe with sub-nm precision. Below this, the optical microscope objective is mounted in a 3D nanopositioning piezo stage such that its 3D position with respect to both the sample and AFM probe can be adjusted

with high accuracy. The general scheme of co-locating the force data in the micrographs depends on aligning the AFM tip in the laser focus.

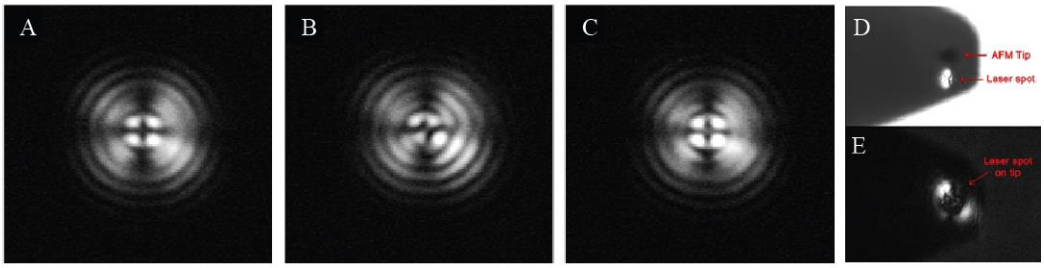


Figure 3.2: Alignment of AFM Tip in Laser Focus. A) Pattern of back-reflected light with tip withdrawn, B) with tip on surface but not aligned, C) with tip on surface and in laser focus. D) Cantilever, tip and laser spot before alignment. E) Laser spot on tip. Adapted from[191].

This is acheived by bringing the tip into contact with a glass surface, turning the laser on, focusing on the glass, and moving the objective until the laser light is focused on the tip[191]. The light then creates a distinct pattern of reflection on the glass surface (Figure 3.2). The tip and objective are thus aligned, and the tip can be withdrawn. The objective can then be rastered to collect a confocal micrograph of the tip and sample. Points of interest determined from the micrograph can then be designated for indentation in the AFM software. In §3.2, square regions from the nuclear areas of the cells are indented in a grid pattern. In §3.4, lateral (XY) micrographs are conducted to identify points of interest in each cell (nuclear, nucleolar, and cytoplasmic regions), which are then indented, as demonstrated in Figure 3.3. In §3.6, axial (YZ) micrographs are conducted to get a cross-section of the sample, and a line of indentations on the surface is conducted in the plane of the image.

The CLSM is equipped with 470 nm and 640 nm lasers for excitation, and two single photon counting modules for detection[191]. With this setup, the fluorescence dynamics can be followed on time scales from picoseconds to seconds, which allows the acquisition of fluorescence lifetime images. In this dissertation, changes in fluorescence lifetimes are only used qualitatively to enhance contrast in images of cells. For example, a nucleic acid dye tends to have a shorter fluorescence lifetime in the mitochondria than in the nucleus, which helps identify different subcellular features.

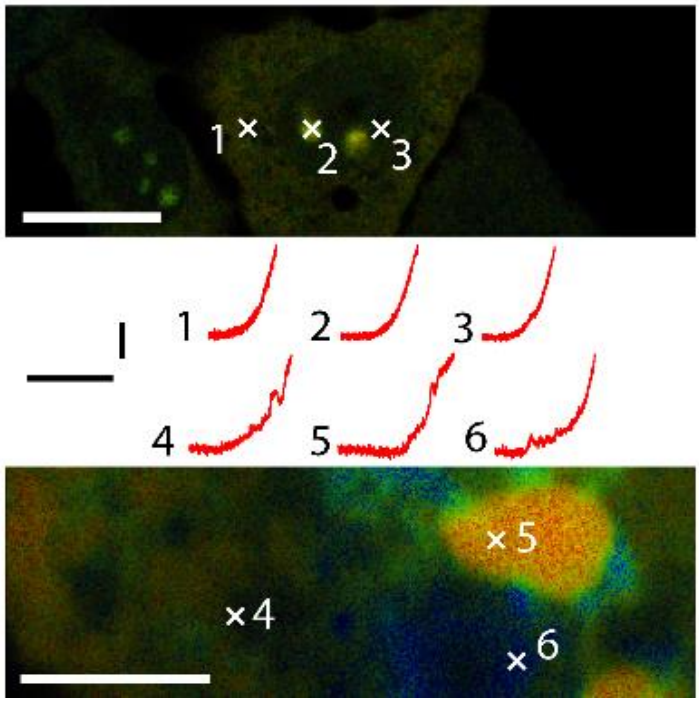


Figure 3.3: Spatially Co-registered Indentation Force-Depth Curves. Top: confocal fluorescence lifetime micrograph of MCF10A cell stained with nuclear and nucleolar dyes. Scale bar: 10 μm. Bottom: MDA-MB-231 cell. Scale Bar: 4 μm. Middle: Indentation force-depth curves taken over the numbered locations. Scale bars: 2 μm (horizontal); 0.2 nN (vertical).

3.2 AFM Stiffness Nanotomography Study of EPC2, CPA, and CPD Cells

3.2.1 Contributions

This work is published in *Physical Biology*[21]. Cells were cultured and seeded on glass dishes by Patti Senechal-Willis. Measurements were conducted by Alexander Fuhrmann, Vivek Nandakumar and myself. I worked closely with Alexander Fuhrmann to develop the analysis methods and to fit the data. The manuscript was written by Robert Ros, Alexander Fuhrmann and myself. Alexander Fuhrmann and myself are listed as first authors.

3.2.2 Overview

In this section, findings from a study of the local mechanical properties of esophageal cells in different phases of premalignancy are presented. Cells from a normal squamous cell line (EPC2)[192] and two Barrett's Esophagus columnar cell lines (CP-A and CP-D) were studied as a model of pre-neoplastic progression in the human esophagus. CP-A was derived from biopsies taken from a region of non-dysplastic metaplasia and CP-D was derived from biopsies taken from regions of high-grade dysplasia[193]. Previous cytogenetic studies have revealed p16 deletion and wild-type p53 in CP-A, and both p16 and p53 deletion in CP-D. The cell lines were shown to be karyotypically similar to *in vivo* counterparts[193,194]. This is the first comparative elasticity study of premalignant cells.

64 force indentation curves were taken over the nucleus of each cell in an 8×8 grid pattern. Analyzing the force indentation curves, indentation depth dependent

Young's moduli were found for all cell lines. Stiffness tomograms demonstrate distinct differences between the mechanical properties of the studied cell lines. Comparing the stiffness for indentation forces of 1 nN, most probable Young's moduli were calculated to 4.7 kPa for EPC2 (n=18 cells), 3.1 kPa for CP-A (n=10), and 2.6 kPa for CP-D (n=19). The influence of nuclei and nucleoli staining organic dyes on the mechanical properties of the cells was also tested. For stained EPC2 cells (n=5), significant stiffening was found (9.9 kPa), while CP-A cells (n=5) showed no clear trend (2.9 kPa) and a slight softening was observed (2.1 kPa) in the case of CP-D cells (n=16). Some force-indentation curves show non-monotonic discontinuities with segments of negative slope, resembling a sawtooth pattern. The incidence of these 'breakthrough events' was highest in the dysplastic CP-D cells, intermediate in the metaplastic CP-A cells, and lowest in the normal EPC2 cells. This observation suggests that the microscopic explanation for the increased compliance of cancerous and pre-cancerous cells may lie in their susceptibility to 'crumble and yield' rather than their ability to 'bend and flex'.

3.2.3 Results

In order to precisely localize the cell nuclei and nucleoli, FLIM was employed rather than regular fluorescence because of its higher contrast. The lifetimes of the fluorophores' excited states depend on the decay pathways available, which are sensitive to any number of highly localized environmental conditions that might influence the cell's mechanical properties[195]. Figure 3.4 shows fluorescence lifetime images of a single CP-D cell stained with nuclear and nucleolar dyes, in its entirety (Figure 3.4A) and in a close-up of the nucleus (Figure 3.4B).

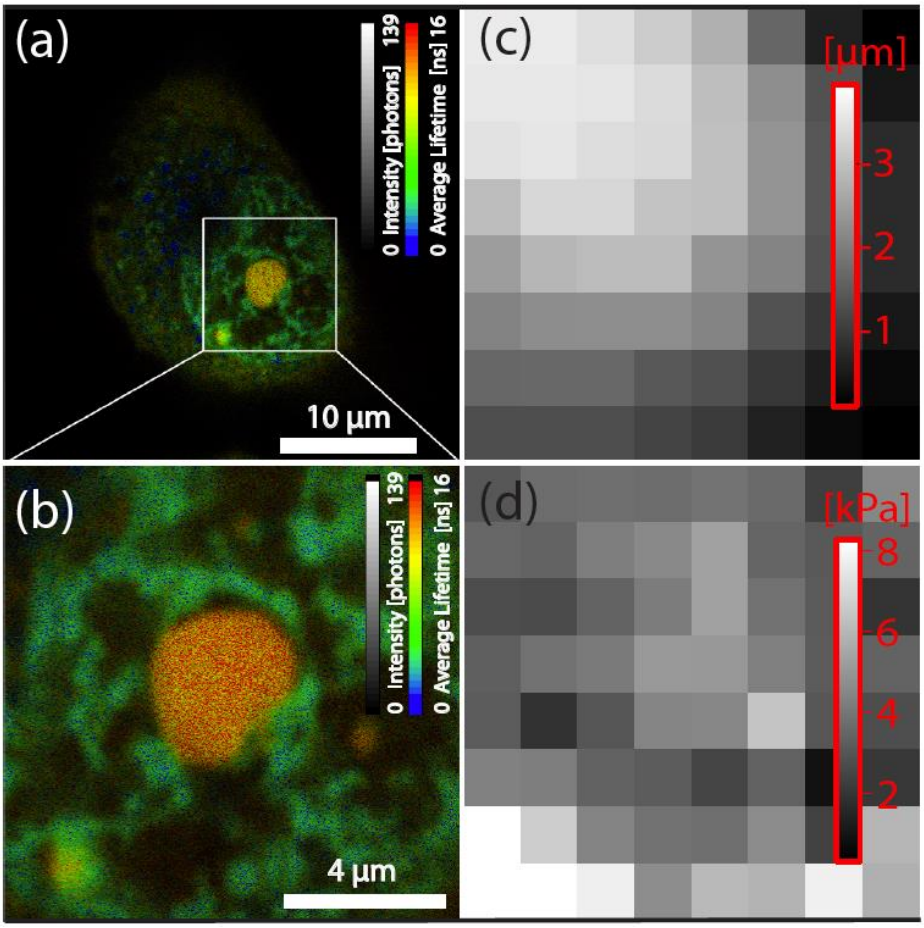


Figure 3.4: Adherent dysplastic CP-D esophageal cell analyzed with combined fluorescence lifetime imaging and AFM-based nanoindentation. Confocal fluorescence lifetime images of the cell labeled with nuclear dye emitting in red and nucleolar dye emitting in green (a) in its entirety and (b) in a close-up of the nucleus. Pixels are color-mapped to average fluorescence lifetime and intensity-mapped to photon count. The AFM tip is aligned with the confocal volume before scanning. Topography (c) and elasticity (d) from 8×8 AFM force map of the same area as (b) with a trigger force of 1 nN. Height is calculated from the AFM cantilever's vertical position at maximal indentation. Young's moduli are calculated with the Hertz model from the final region of each force-indentation curve. Adapted from[196].

The images integrate data from the emission spectra of both dyes. The intensity of photons in each pixel is represented by the brightness of the pixel, and the average lifetime of dye molecules detected in each pixel is represented by the color. Different fluorescence lifetimes of the two dyes allow the superposition of the two

fluorescence channels. In Figure 3.4A, distinct chromatin structures in the nucleus are light blue-green in color. Small blue ellipses in the cytoplasm indicate mitochondrial DNA. The shorter lifetime of mtDNA may be due to lower pH in the mitochondrial matrices. In Figure 3.4B, the nucleoli are yellow-red. A topography map of the same field of view is shown in Figure 3.4C. The cell is indented 64 times in an 8×8 grid. In each indentation, the AFM probe presses into the cell until 1 nN of force is applied, whereupon the tip is retracted. The vertical position of the AFM cantilever at maximum indentation is plotted to visualize a stiffness dependent measure of its height. The Young's modulus of the final fit line in the $F^{2/3}$-δ curve from each indentation in Figure 3.4B is plotted in figure 3.4D. The stiffness of the cell is clearly heterogeneous on length scales of ~1μm. No obvious correlation can be seen between the fluorescence image and the AFM data, perhaps because the nuclear membrane redistributes the load applied by the tip. The central nuclear region exhibits soft spots, while the nuclear membrane in the bottom corners appear stiffer.

Mechanical properties for deep indentations

To investigate and compare the elasticities of the nuclei of EPC2, CP-A and CP-D cells, nuclei from several cells were indented 64 times each in 8×8 grids in $(\sim 5\mu m)^2$ areas. The Young's moduli of the final fit lines were calculated. The six distributions of moduli from the three different cell lines, both unstained (Figure 3.5A) and stained (Figure 3.5B), were assessed with a kernel smoothing density (KSD) algorithm.

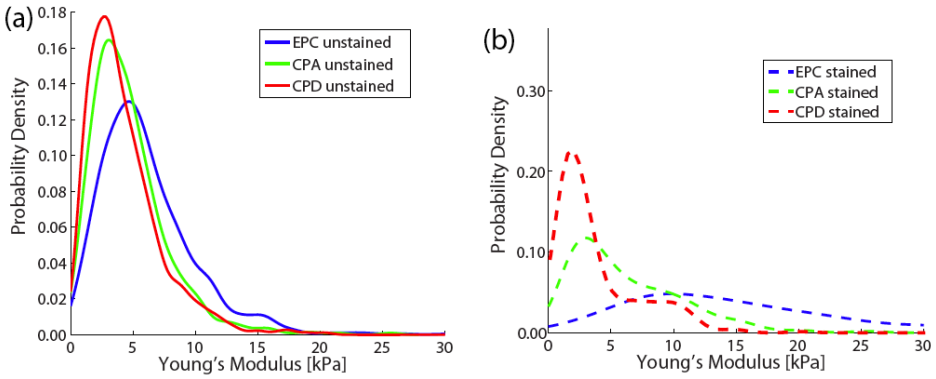


Figure 3.5: Distributions of Young's moduli of EPC2, CP-A, and CP-D esophageal cell nuclei. Kernel smoothing density estimates of Young's moduli calculated from the final region of each (of n) force-indentation curves collected from 8×8 force maps of cell nuclei. FLIM images are taken (before) to identify nuclei and determine scanning region (~5 μm) of the force maps and (after) to verify that cell has not moved appreciably (≤1 μm) during measurement. Data from (a) unstained EPC2 (n=1152), CP-A (n=640), and CP-D (n=1216) cell nucleus indentations. The modal Young's modulus is highest for EPC2, intermediate for CP-A, and lowest for CP-D (see Table 3.1). Data from (b) EPC2 (n=320), CP-A (n=320), and CP-D (n=1024) cells labeled with both nuclear and nucleolar dyes indicates that with these dyes, the modal Young's modulus of EPC2 increases by a factor of 2, that of CP-A is unchanged, and that of CP-D decreases slightly (see Table 3.1). Adapted from[196].

Figure 3.6 demonstrates that the KSD characterizes the distributions very well.

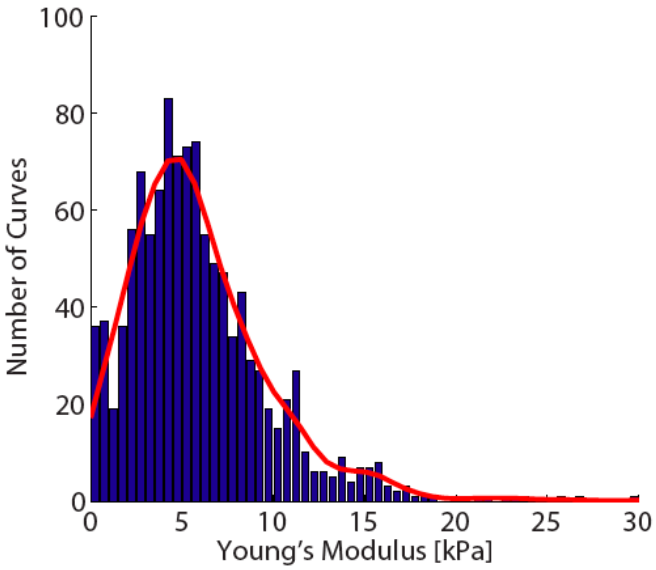


Figure 3.6: Histogram and ernel smoothing density estimate of unstained EPC2 cells. The Young's moduli calculated from the final fit lines of all unstained EPC2 $F^{2/3}$-δ curves are binned into 500 Pa bins and plotted in a histogram to display the accuracy of the kernel smoothing density estimate of the distribution. Adapted from[196].

Because there is yet no specific model for the distribution of Young's moduli at the spatial resolution of AFM-based nanoindentation, we use the KSD as a model-independent statistical estimate of the modal Young's modulus and distribution width (see Table 3.1). The modal Young's modulus of unstained EPC2 was 4.7 kPa. Those of unstained CP-A and CP-D were 3.1 kPa and 2.6 kPa, respectively. The non-dysplastic CP-A cells in this study are thus softer than the normal EPC2 cells by a factor of ~1.5, while the dysplastic CP-D cells are softer by a factor of ~1.8. These noteworthy premalignant variations in stiffness suggest that mechanical compliance increases gradually along with the morphological changes marking the progression from metaplasia to neoplasia. The changes in compliance we found complement previous reports that malignant cells are softer than their normal counterparts by factors ranging from 2-4[9,8,197].

Cell Type	Number of cells	Total number of indentations	Modal Young's Modulus (kPa)	FWHM (kPa)
EPC2 unstained	18	1152	4.72	7.17
CP-A unstained	10	640	3.08	5.64
CP-D unstained	19	1216	2.64	5.49
EPC2 stained	5	320	9.89	17.96
CP-A stained	5	320	2.98	7.04
CP-D stained	16	1024	2.12	5.65

Table 3.1: Kernel Smoothing Density Estimates of Modal Young's Moduli and Distribution Full Widths at Half Maxima. Adapted from[196].

The influence of nuclear and nucleolar dyes on the mechanical properties of the cells was also tested (Figure 3.5B). For EPC2 cells stained with Nuclear ID Red and Nucleolar ID Green, significant stiffening was found (9.9 kPa). This is in accordance with single cell compression experiments on cells stained with various cell tracing dyes[198]. In contrast, the stained CP-A cells showed no clear trend (2.9 kPa) and a slight softening was observed (2.1 kPa) in the case of stained CP-D cells. This effect may reflect systemic differences in the metabolic and regulatory processes that govern cytoskeletal stability in the abnormal cell lines.

Segmental analysis of force-indentation curves

To better understand the nature of the mechanical differences between these cells, the force-indentation curves were anlayzed to get the Young's modulus as a function of the indentation depth. In contrast to curve fitting approaches[199,200] (such as employed in §3.4), the algorithm used here detects Hertzian-like segments and analyzes the Young's modulus, depth and length of these segments. Figures 3.7A and 3.7B depict 3D elasticity maps of CP-A and CP-D cells, respectively.

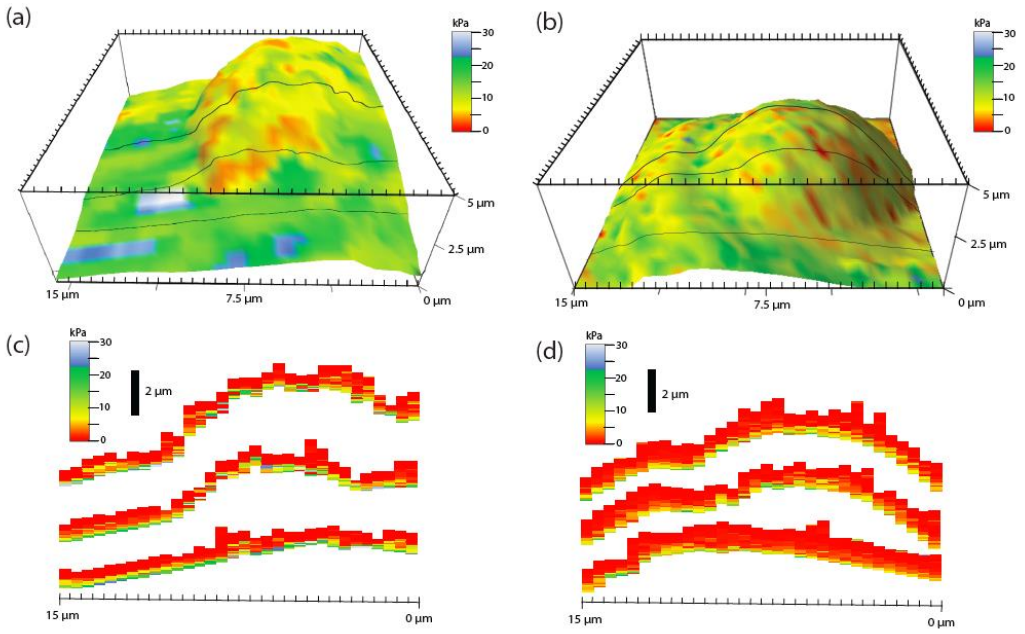


Figure 3.7: 3D elasticity maps and corresponding elastic tomograms of CP-A and CP-D cells. 3D elasticity maps of typical (a) CP-A and (b) CP-D cells. Black lines on surfaces correspond to the elasticity tomograms shown in (c) and (d). Surfaces and tomograms are color-mapped to Young's modulus. In a tomogram, each vertical rectangular stack depicts a single indentation. The AFM tip contacts the cell at the top and retracts at the bottom of each stack. Tall (short) stacks occur at points where the cell is more (less) deformable. White bands in the stack indicate breakthrough events. The CP-D cell not only has a lower Young' modulus toward the end of the indentation, but it is also more homogeneous and more deformable than the CP-A cell. Adapted from[196].

The surface heights and Young's moduli are calculated from force maps as in Figure 3.4. The surface is color-mapped to the Young's modulus. Additionally, three horizontal black lines are projected on the surface of each cell. These lines correspond spatially to the elasticity tomograms in Figures 3.7C and 3.7D. Each tomogram consists of 32 vertical stacks. Each stack contains information about a single indentation. The top of each stack corresponds to the height at which the AFM tip first contacts the cell, as estimated by the linear piecewise fitting algorithm.

Each colored band corresponds to the Young's modulus from a single linear segment fitting a region of the $F^{2/3}$-δ curve. The bottom of the stack corresponds to the depth at which the trigger force is reached, and is therefore the same color as the corresponding position of the surface in Figure 3.7A or 3.7B. The greater heights of the CP-D vertical stacks indicate that the CP-D cell is more deformable than the CP-A cell. The CP-D cell appears to be more laterally mechanically homogeneous than the CP-A cell, as indicated by the nearly uniform distribution of yellow bands beginning at about 80% of the total indentation depth. Neither cell is mechanically homogeneous radially, especially as evidenced by the multitude of extremely narrow white bands, representing negative slopes on the $F^{2/3}$-δ curve (breakthrough events, see below).

Because the $F^{2/3}$-δ curves of living cells are so frequently not simply linear, but rather piecewise linear, a single cited value for the Young's modulus of a cell cannot accurately express the cell's elasticity. Therefore Young's moduli are plotted as a function of indentation depth in the form of 2D histograms in Figure 3.8.

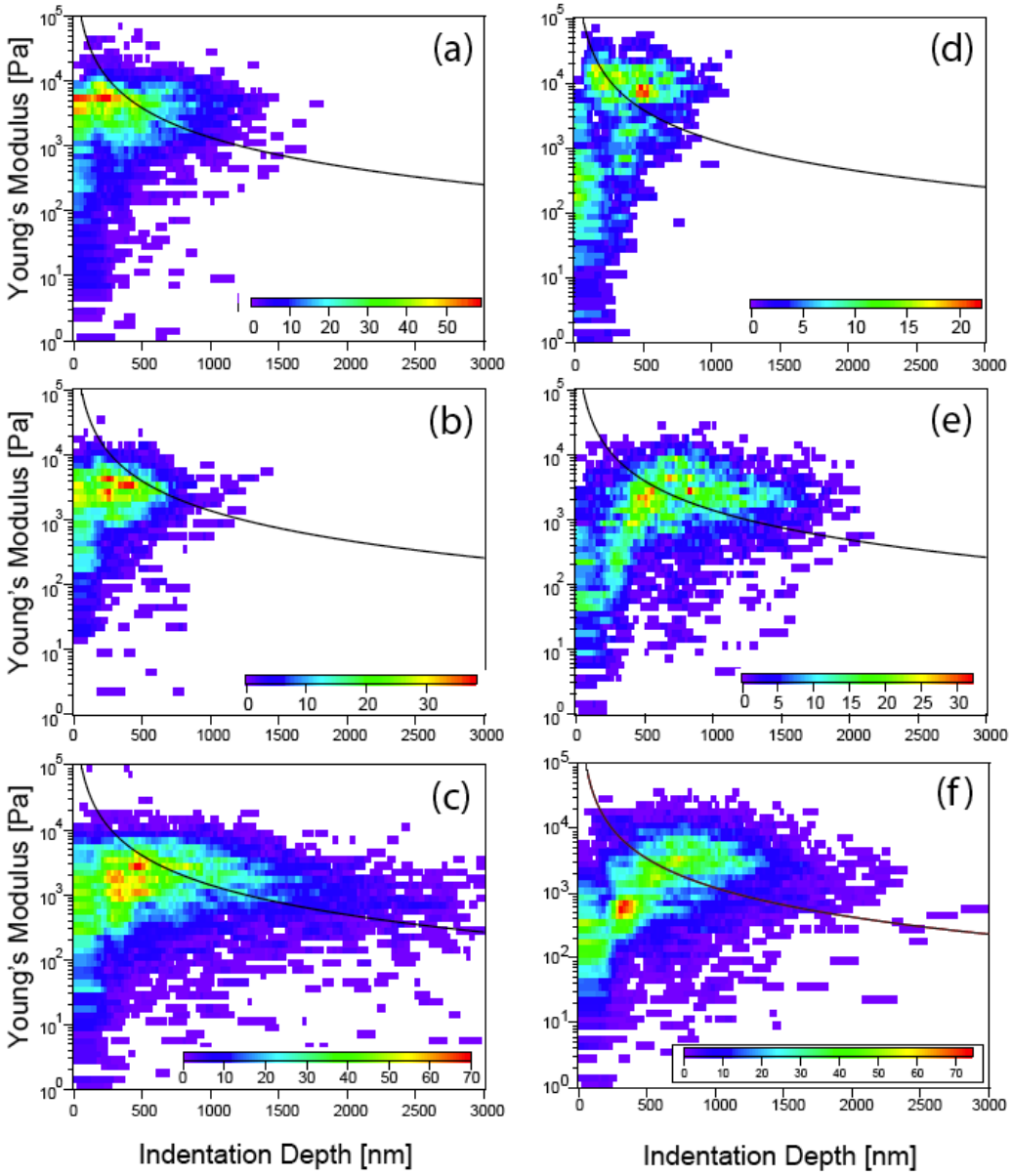

(a)
(b)
(c)
(d)
(e)
(f)
Young's Modulus [Pa]
Indentation Depth [nm]
Indentation Depth [nm]

Figure 3.8: 2D elasticity histograms of Young's modulus vs. indentation depth. $F^{2/3}$-δ curves are reconstructed piecewise with linear segments. The starting depth, stopping depth, and slope of the linear segments are then used to construct a 2D histogram of Young's modulus vs. indentation depth. Each segment is binned horizontally by indentation depth into 25 nm bins and vertically by the Young's modulus calculated from its slope into 50 bins spaced logarithmically over five decades, up to 100 kPa. The histograms are color-mapped by counts per bin. Unstained (a) EPC2 (n=1152), (b) CP-A (n=640), (c) CP-D (n=1216) cells and stained (d) EPC2 (n=320), (e) CP-A (n=320), and (f) CP-D (n=1024) cells are shown. The black curve plotting the (E, δ) coordinate solutions of the Hertz equation for F = 1 nN applied force. Hertzian behavior (i.e. depth-independent moduli) is characterized by horizontal bands of uniformly occupied bins, such as the red peak in (a) at 5 kPa from 0-400 nm. The degree to which the Young's modulus varies with indentation depth differs significantly among the cell lines and with the addition of fluorescent dyes. Adapted from[196].

These histograms quantify the depth dependence of cell stiffness and illustrate important differences between these cell lines that cannot be distinguished by nominal depth-independent values of Young's moduli. The starting depth, stopping depth, and slope of each linear segment from each $F^{2/3}$-δ curve are used to bin the segments horizontally by indentation depth into 25 nm bins and vertically by the Young's modulus calculated from their slopes into 50 bins spaced logarithmically over five decades, up to 100 kPa. Each segment exceeding 25 nm indentation spans multiple bins. The histograms are color-mapped by counts per bin. Segments with negative slopes are excluded.

On each histogram, a black curve is superposed plotting the (E, δ) coordinate solutions of the Hertz equation for F = 1 nN. Because our measurements are performed with a fixed trigger force, an ideal Hertzian cell with constant Young's modulus would occupy a horizontal band of bins spanning from the vertical axis to the Hertz curve. A cell of lower (higher) Young's modulus will be indented more (less). The curve thus provides a point of comparison for the way each cell line

differs from an ideal Hertzian cell. A stress hardening cell with monotonically increasing Young's modulus should occupy bins forming a convex curve on the histogram, contributing to the portion of the distribution near the origin. A cell with non-monotonic changes in Young's modulus occupies bins in a more complicated pattern, contributing to the portion of the distribution to the right of the Hertz curve.

The degree to which the Young's modulus varies with indentation depth differs significantly among the cell lines and with the addition of fluorescent dyes. Data from (n) indentations on (m) cells are shown: unstained (a) EPC2 (n=1152, m=18), (b) CP-A (n=640, m=10), (c) CP-D (n=1216, m=19); and stained (d) EPC2 (n=320, m=5), (e) CP-A (n=320, m=5), and (f) CP-D (n=1024, m=16). In the case of (a) unstained EPC2, the red horizontal band of peaks at ~5 kPa is somewhat Hertzian. However, many EPC2 $F^{2/3}$-δ curves show hardening with depth. Unstained CP-D (c) exhibits an isolated cluster (in contrast to a horizontal band) of peaks from ~1-2 kPa. The CP-D distribution is very broad and extends considerably past the Hertz curve. Characteristic maximum indentation values can be seen by looking at how far to the right the histograms reach. The bright blue region of the CP-D histogram extends to ~1500 nm, whereas the bright blue region of the EPC2 histogram only extends to ~800 nm. Irrespective of the calculated Young's moduli, the CP-D cells are thus much more deformable than the EPC2 cells. Cell height was typically 7-12 μm for those cells whose height was measured, corresponding to strains of ~10%. At such strains, the Hertz model works well for indentations on cell nuclei[170]. Interestingly, the dyes had adverse effects on the different cell lines. The dye apparently caused a

decrease in deformability and increase in stiffness of EPC2, opposite effects on CP-D, and an increase in deformability but no change in stiffness in the case of CP-A.

The strain borne by a cell during indentation is clearly not a simply linear function of the stress. Moreover, the distributions exhibit neither simple strain hardening nor softening, but rather a mixture of the two. These changes in stiffness could possibly reflect either active rearrangement in which stretch-induced membrane stress activates Rho signalling[201], or passive rearrangement in which the applied load causes geometrical changes such as buckling[202]. The nanoscale details of the cytoskeleton's response to nanoindentation remain unknown, but further development of combined fluorescence techniques may shed light on the processes involved.

Discontinuities in the force-indentation curves

In order to further investigate this nonlinearity, segments of the $F^{2/3}$-δ curves that exhibit negative slopes were examined. Linear segments of $F^{2/3}$-δ curves with negative slope occur when the resistance levied by the cell against the AFM tip is suddenly relieved, allowing it to descend further into the cell with less applied force. An example of this is shown in Figure 3.9A.

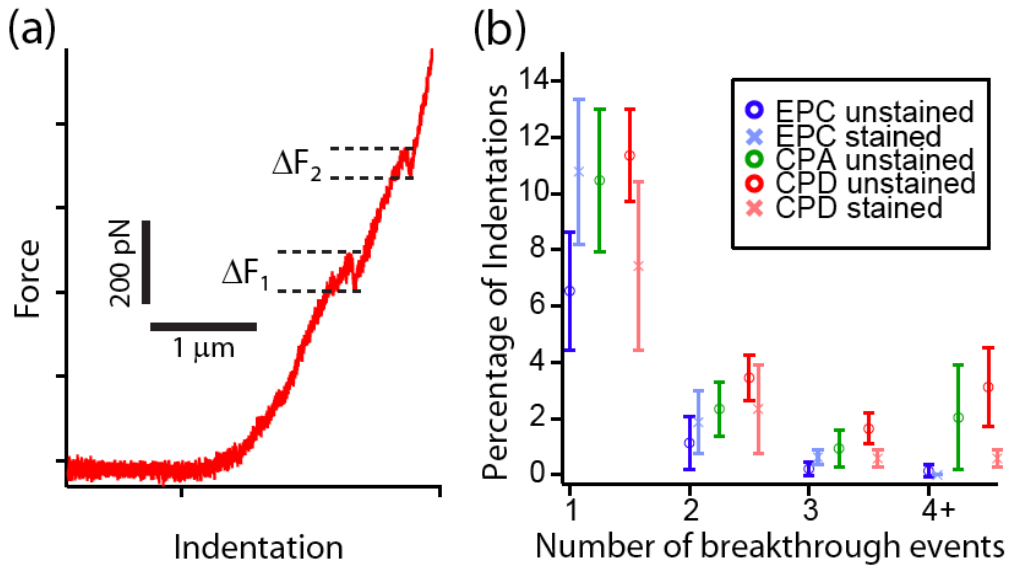


Figure 3.9: Nanoscale cytoskeletal instability quantified by frequency of incidence of breakthrough events. Linear segments of $F^{2/3}$-δ curves with negative slope occur when the resistance levied by the cell against the AFM tip is suddenly relieved, allowing it to descend further into the cell with less applied force. These 'breakthrough events' may correspond to disruptions of pre-stressed tensile structures in the cytoskeletal mesh due to transverse compression by the AFM tip. The percentages of indentations with (exactly) 1, 2, 3, and 4 or more breakthrough events are plotted. Breakthrough events are most frequent in the CP-D cells, as corroborated by the multitude of narrow white bands in the elasticity tomograms. Interestingly, CP-D exhibited more and EPC2 exhibited less breakthroughs with the use of the nuclear and nucleolar dyes. Adapted from[196].

In most cases, the segments of negative slope reflect large changes in applied force over very small distances. These changes may correspond to events in which stresses induced by the AFM tip on cortical structures are transferred by intermediate filaments to stress fibers deeper in the cytoskeleton that break, ultimately allowing superficial material to displace or slip past the disrupted filamentous matrix. Such occurrences are dubbed 'breakthrough events'. The number of breakthrough events can thus be seen as a measure of structural integrity. Breakthrough events should be most frequent in cells with cytoskeletons weakened, for example, by underexpression

of actin-binding proteins (ABPs) such as filamin A, downregulation of which is known to occur following the differentiation of neuronal cells[203], and may likewise occur following metaplastic transformation. Apart from its structural role as an actin crosslinker, filamin has been shown to modulate epidermal growth factor receptors (EGFR)[204], which are known to be deregulated in squamous malignancies[192]. The frequency to observe breakthrough events differs significantly between the normal EPC2, metaplastic CP-A and dysplastic CP-D cells. Figure 3.9B shows the percentages of total indentations exhibiting 1, 2, 3, and 4 or more breakthroughs for stained and unstained cells of each cell type. The probability of observing breakthrough events increases considerably from EPC2 to CP-A to CP-D. The probability of multiple breakthroughs follows the same pattern of increase. This observation suggests that the microscopic explanation for the increased compliance of cancerous and pre-cancerous cells may lie in their susceptibility to 'crumble and yield' rather than their ability to 'bend and flex'.

Cells with greater structural integrity should also require a greater applied force in order for the AFM tip to elicit a breakthrough. When summed, the changes in force ΔF from each breakthrough give the total breakthrough force from a single indentation, $\sum \Delta F$; of those curves exhibiting at least one breakthrough, we found no clear difference in $\sum \Delta F$ between the cell lines (Figure 3.10).

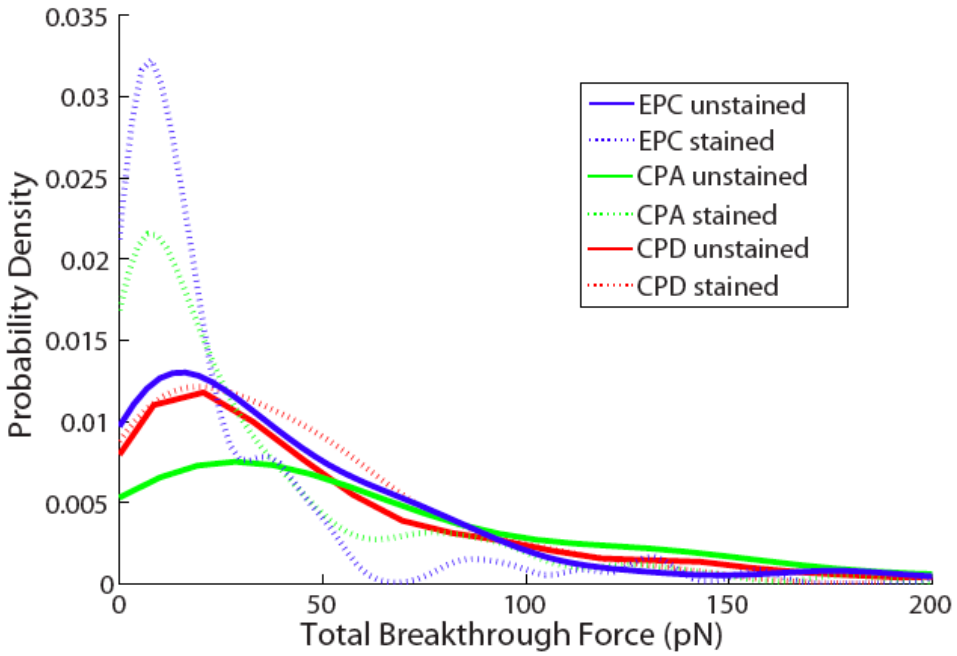


Figure 3.10: Kernel smoothing density estimates of total breakthrough forces. The changes in force ΔF of each breakthrough event on a curve are summed to give the total breakthrough force $\sum \Delta F$ of the curve. The total breakthrough forces of all curves with at least one breakthrough event are collected into distributions and their kernel smoothing density estimates are plotted. The modal total breakthrough force is roughly the same for each cell type, while the distributions differ somewhat. Since the total amount of breakthrough events is rather low, the sample size of breakthroughs is not statistically robust. However, interestingly, there appears to be no connection between the probability for breakthroughs to occur and the total breakthrough force. Adapted from[196].

Since only a modest percentage of the measured curves exhibited breakthroughs, larger sample sizes may be necessary to see a trend in this data.

3.2.4 Conclusions

In §3.2, metaplastic CP-A and dysplastic CP-D precancerous esophageal cells were found to be significantly softer than normal EPC2 cells. Additionally, staining the nuclei and the nucleoli with organic dyes was found to produce adverse effects on the mechanical properties of the different cell lines: EPC2 showed significant

stiffening, while CP-A showed greater deformability and CP-D showed softening. Correlations between stiffness and the spatial arrangement of chromatin or nucleoli in the nucleus were not evident; however, labeling other subcellular structures might reveal correlations in future work.

A robust piecewise linear fitting algorithm was developed and applied to determine indentation depth dependent Young's moduli. Segmental analysis of force-indentation curves was used to clarify distinctions between stiffness and deformability in cells with non-linear strain-hardening. Stiffness tomograms and 2D histograms identified subtle differences in the distributions of the mechanical properties of the cell lines. Divergence from Hertzian behavior was assessed in terms of $F^{2/3}$-δ curves whose slopes increase non-monotonically. The frequency of segments with negative slope ('breakthroughs') in AFM force-indentation curves may also prove to be a useful parameter in the characterization of cytoskeletal stability.

Even in the earliest stages of cancer development, the mechanical properties of the cell are altered. This study, conducted on a cell line model of pre-neoplastic progression in the human esophagus, suggests that the correlation between increased elasticity and malignancy holds even in the early stages of metaplastic transformation. While measurements on explanted cells would strengthen the case, the results are consistent with the growing body of evidence from a variety of different experimental techniques and cell types that cells in later stages of many cancers are abnormally soft.

3.2.5 Materials and Methods

Cell Culture

Immortalized Barrett's Esophagus (BE) cells derived from non-dysplastic metaplasia (CP-A cells) and high-grade dysplasia (CP-D cells) and normal esophageal cells (EPC2 cells) were used for the experiments[193,194]. Cells from all studied cell lines were cultured in Keratinocyte-serum free medium 1× (Invitrogen, Carlsbad, CA). The medium contained L-glutamine and calcium chloride. Additional supplements added to the medium prior to use were bovine pituitary extract (1×25 mg, Invitrogen) and epidermal growth factor- human recombinant (1×2.5 μg, Invitrogen).

Sample preparation

The cultured cells were then seeded at ~30% confluence into 50 mm glass bottom Petri dishes (Fluorodish, World Precision Instruments) and incubated with growth medium at 37°C and 5% CO_2 for a period of 72 hours. The medium was exchanged with 1 ml imaging assay buffer (Enzo Life Sciences) prior to AFM measurements to provide an optically clear medium optimized for fluorescence imaging. HEPES was added to a concentration of 25 mM to maintain CO_2 levels and NaOH was added to ensure a pH of 7.5. For experiments on stained cells, 5 μl of 1:5 diluted stock solution of Nuclear ID Red (Enzo Life Sciences) and 5 μl of 1:5 diluted stock solution of Nucleolar ID Green (Enzo Life Sciences) were added to the medium 30 minutes prior to AFM measurements and allowed to diffuse with gentle swirling.

AFM nanoindentation

Soft silicon AFM probes with nominal spring constants k ≈ 10 pN/nm (MSNL, Veeco Instruments, Santa Barbara, CA) were used for the indentation experiments. The spring constant of each cantilever was determined from the thermal noise

spectrum[164,165]. The AFM tip and the confocal volume were aligned using the pattern of back-scattered light as described in §3.1[191]. After the alignment, the AFM tip is fully retracted and the sample stage is moved until a cell of interest is under the tip. A FLIM image of the cell in two frequency bands (green and deep red) is acquired while the tip is still retracted. In the FLIM image, the cell nucleus is identified and precisely located. The nucleus is brought directly under the AFM tip. In a $(\sim 5\ \mu m)^2$ region, an 8×8 grid of indentations is acquired with 2 μm/s approach and retract speeds in force volume mode with a trigger force of 1 nN. After indentation, a subsequent FLIM image is taken of the cell with exactly the same settings as the preliminary image. The two images are superposed in software (ImageJ[205]) to determine the extent to which the cell moved during the measurements. If the cell moved more than ~1 μm, then the data is discarded and is not further analyzed. The alignment of the tip is then verified as above and another cell can be located and measured. After measurements, the probes were imaged with a scanning electron microscope and the tip radii were determined to be in the range of 50 nm.

Data analysis

Each indentation generates a force-indentation (F-δ) curve to be saved and analyzed with custom written software (Igor Pro, Wavemetrics, Portland, OR). The curves are corrected for cantilever bending. All force data points are incremented by a constant so they are all positive, subsequently raised to the 2/3 power, and then plotted in a $F^{2/3}$-δ curve. According to the Hertz model[184] of a sphere indenting an elastic half-space, the Young's modulus E is directly proportional to the force F and inversely proportional to the 3/2 power of the deformation δ:

$$F_{Hertz} = \frac{4}{3} r^{1/2} \frac{E}{(1-\nu^2)} \delta^{3/2} \tag{14}$$

where F is the load distributed over the contact area, r is the radius of the sphere, ν is the Poisson ratio of the surface, δ is the deformation of the sample, and E is the Young's modulus of the sample. Here, the AFM tip is approximated as a sphere of radius r on a cantilever deflected by a force F. The cell is approximated as a flat, isotropic material with a Poisson ratio of 0.4 that is elastically deformed by the AFM tip in the limit of small strains[185]. Accordingly the $F^{2/3} - \delta$ curve should be linear[206], with a slope directly proportional to $E^{2/3}$:

$$slope = \frac{\Delta {F_{Hertz}}^{2/3}}{\Delta \delta} = \left[\frac{4}{3} r^{1/2} \frac{E}{(1-\nu^2)}\right]^{2/3} \tag{19}$$

$$E(\delta) = \frac{3(1-\nu^2)}{4r^{1/2}} {slope}^{3/2} \tag{20}$$

In practice, however, the $F^{2/3} - \delta$ curves generated by AFM-based nanoindentation are not simply linear. Rather, linear segments corresponding to layers with different stiffness can be seen at different depths. Therefore a robust piecewise linear fitting algorithm is used to reconstruct the curves into segments of constant Young's modulus $E(\delta)$ at different depths. The algorithm works by first fitting a line in a small region of the curve and then iteratively extrapolating it until a parameter-sensitive deviation threshold is exceeded. Then another small line is fit in the adjacent region and the process repeats until the whole curve is fit. The algorithm first fits the baseline and determines the contact point in this manner, and then fits

the indentation region. It is worth noting that determination of the contact point is critical in AFM force-indentation analyses, but this scheme is less sensitive to errors in contact point determination than those that fit power curves from the contact point through the entire indentation.

To characterize statistical distributions, we used a kernel smoothing density estimate function ("ksdensity.m", Matlab, Mathworks, Natick, MA).

3.3 AFM Nanoindentation Study of MDA-MB-231 and MCF-10A Cells

3.3.1 Contributions

This work was published in *Nature Scientific Reports* as part of a large collaboration[22]. Alexander Fuhrmann trained me to use the AFM; Olaf Schulz trained me to use the confocal microscope. Cells were cultured by Patti Senechal-Willis. I conducted the experiments. Alexander Fuhrmann and I worked closely together to develop the force-curve analysis method and to fit the data. In addition to the AFM work presented in this section, I assembled raw data, tables, figures and micrographs from all 94 of the participating authors, helped write the manuscript and am listed as 'first authorship leader'.

3.3.2 Overview

In this work, the local mechanical properties of non-tumorigenic MCF10-A and metastatic MDA-MB-231 human breast cells were studied using the combination of an atomic force microscope (AFM) with a scanning confocal fluorescence lifetime microscope. Cells stained with nuclear and nucleolar dyes were indented at distinct points over the cytoplasmic regions, nucleus, and nucleoli. The Young's modulus was measured and varied considerably from point to point and with the indentation depth.

3.3.3 Results

Young's moduli are calculated from the slope of each linear segment using the Hertz model. Some curves show different linear segments, which reflect depth-dependent

mechanical properties, expected for such heterogeneous materials as live cells. The deformability of the cells is compared in Figure 3.11.

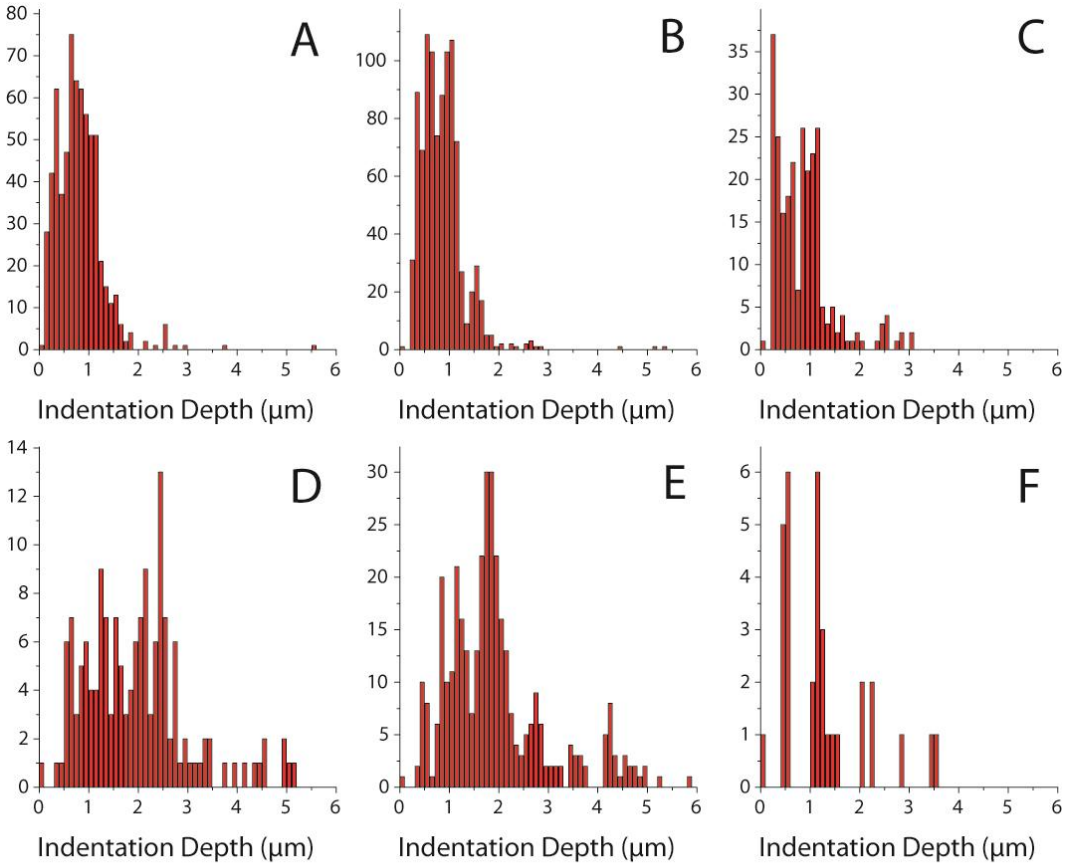


Figure 3.11: Histograms (bin size = 100 nm) of total indentation depth from contact to retraction at 600 pN for MCF10-A cells (A) cytoplasm, (B) nuclei, (C) nucleoli and MDA-MB-231 cells (D) cytoplasm, (E) nuclei, and (F) nucleoli. The MDA-MB-231 cells are more deformable than the MCF10-A cells and have a wider distribution of indentation depths.

Not surprisingly, the softer MDA-MB-231 cells had greater deformations on average and wider distribution. For a force of 600 pN, the average indentation depth is 800 nm.

The resulting force-indentation curves were fitted to a modified Hertz model in 100-nm intervals, yielding depth-dependent elastic moduli (Figure 3.12).

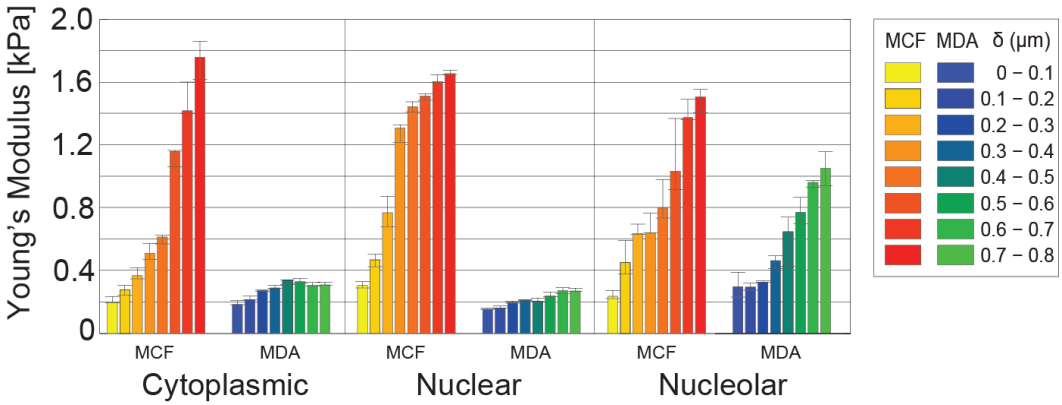


Figure 3.12: Young's Moduli (mean ± standard error) of MCF10A and MDA-MB-231 Cells as a Function of Indentation Depth in Different Subcellular Regions. Adapted from[22].

At shallow indentation depths, the two cell lines had similar elastic moduli (~200 Pa). Cytoplasmic and nuclear stiffness of MDA-MB-231 cells increased only slightly with increasing indentation depth, whereas cytoplasmic and nuclear elastic moduli of MCF-10A cells both increased - though with different strain-hardening profiles - about four-fold to ~1.6 kPa. At indentation points over nucleoli, both cell lines showed stiffening with increasing depth, with MDA-MB-231 and MCF-10A cells rising to elastic moduli of ~1 kPa and ~1.5 kPa, respectively, at 0.8 μm.

3.3.4 Conclusions

In §3.3, AFM nanoindentation and confocal fluorescence microscopy were used to invesitage the elasticity of metastatic breast cancer cells and non-tumorigenic mammary epithelial cells. This equipment configuration allows precise probing of different areas of the cell, such as the nucleus, nucleoli and cytoplasm, and spatial co-registration of the force data with the fluorescence micrographs. At shallow

indentation depths (below ~200 nm), the mechanical response is similar between the two cell lines. For deeper indentations, MCF10-A cells are a factor of up to fourfold stiffer than MDA-MB-231 cells. This is in good agreement with previous reported results[8,9,10]. These findings suggest that mechanical loads are transduced through the cytoskeleton differently in the two cell lines. The decreased elastic moduli and increased deformability of MDA-MB-231 cells is consistent with their ability to traverse narrow matrices in 3D microenvironments. In addition, this approach is capable of distinguishing differences in stiffness between cytoplasmic, nuclear, and nucleolar subcellular regions.

3.3.5 Materials and Methods

Cell Culture

Cells from the two cell lines are cultured according to the Physical Sciences in Oncology Cell Line Protocol Version 1.0[207].

Sample Preparation

Cells are plated onto 50 mm glass-bottom dishes (World Precision Instruments) with growth medium (as designated in the Cell Line Protocol) and incubated for 72 hours prior to experiments. For some experiments, 5 μl of SYTO 9 nucleic acid stain (Invitrogen) of a 5 mM stock solution is pipetted into the dish 30 minutes prior to indentation and allowed to diffuse with gentle swirling. 5 μl of CellMask Deep Red lipid membrane stain (Invitrogen) of a 5 mM stock solution is pipetted into the dish 5 minutes prior to indentation and allowed to diffuse with gentle swirling. For other experiments, 5 μl of 1:5 diluted stock solution of Nuclear ID Red (Enzo Life Sciences) and 5 μl of 1:5 diluted stock solution of Nucleolar ID Green (Enzo Life

Sciences) were both added to the medium 30 minutes prior to indentation and allowed to diffuse with gentle swirling.

AFM Nanoindentation

Soft silicon nitride AFM probes with nominal spring constants k ≈ 10 pN/nm (MSNL, Veeco Instruments) are used for the indentation experiments. The spring constant of each cantilever is determined from the thermal noise spectrum[164,165]. After the experiment, the probes were imaged with an SEM to determine the tip radius. The AFM tip and the confocal volume are aligned using the pattern of back-scattered light as described in §3.1[191].

Approximately 20 curves were taken at each point of interest on the cell. After indentation, a subsequent FLIM image is taken of the cell with exactly the same settings as the preliminary image. The two images are superposed in software (ImageJ) to determine the extent to which the cell moved during the measurements. If the cell has moved more than ~1 μm, then the data is discarded and is not further analyzed. The alignment of the tip is then verified as above and another cell of interest can be located and measured.

Data Analysis

The indentation force-depth curves are linearized and fitted piecewise to a modified Hertz model as in §3.2, but the contact regions are instead uniformly segmented into 100 nm segments from the contact point.

3.4 AFM Indentation Study of MCF7 Cells

3.4.1 Contributions

For indentations with standard sharp tips, Mark L. Linhart cultured the cells and seeded them on polystyrene dishes. For indentations with intermediate sized tips, Nethmi Ariyasinghe cultured the cells and seeded them on polystyrene dishes. Some of the analysis methods and parts of the custom MATLAB programs used for the fitting were contributed by Bryant L. Doss. I conducted the AFM indentation measurements and analyzed the data.

3.4.2 Overview

This work was done as part of a collaboration among several labs. Each lab received MCF7 cells from the National Cancer Institute (NCI) and performed various mechanical measurements on the cells. Each lab processed and cultured the cells according to a standard protocol in order to maintain consistency among the groups. Cells' Young's moduli were measured using both sharp ($r \sim 50$ nm) and intermediate ($r \sim 750$ nm) sized AFM tips as the indenter. The apparent modulus is highly dependent on the length scale of the indenter in relation to the mesh size of the actin cortical cytoskeleton, as reflected in the results. Using a larger probe with a greater tip height allows for deeper indentations, which include contributions from actin cortex, intermediate filaments, nuclear mechanics, as well as the cytoplasm.

3.4.3 Results

Figure 3.13 shows the histograms of the Young's moduli determined from force curves conducted with both a sharp nanoscale tip (r ~ 50 nm, k = 0.016 N/m) (top) and an intermediate sized or mesoscale tip (r = 680 nm, k = 0.214 N/m) (bottom).

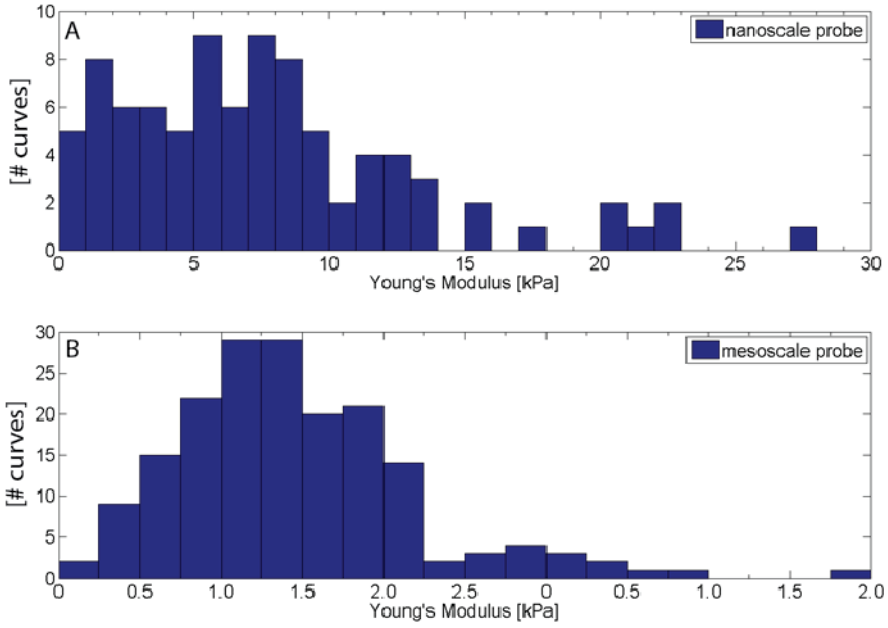


Figure 3.13: Young's Moduli of MCF7 Cells. A) Histogram of values determined with a sharp tip. B) Histogram of values determined with a larger (r = 680 nm, h ~ 14 μm) LRCH tip (bottom).

The nanoscale probe values are much higher than the mesoscale values. The mean, standard deviation, standard error, and median values are listed in Table 3.2.

E [kPa]	Nanoscale probe	Mesoscale probe
Mean	7.67	0.58
Standard Deviation	5.58	0.30
Standard Error	0.59	0.02
Median	6.69	0.55

Table 3.2: Young's moduli of MCF7 Cells. Determined with a sharp tip and a larger (r = 680 nm, h ~ 14 μm) LRCH tip.

3.4.4 Conclusions

In §3.4, AFM nano-indentation and AFM meso-indentation are compared on weakly metastatic breasct cancer cells. The response of the cell to a sharper probe results in a much higher Young's modulus than the probe with a radius on the micrometer scale. The cytoskeletal mesh size (~50-100 nm) is larger or on the order of the sharp tip size, and smaller than the intermediate tip size. Because of this, the sharp tip senses nanoscale heterogeneities in the membrane and actin cortex that are instead averaged over by the larger tip. These heterogeneities are revealed in the long tailed distribution of the Young's moduli determined from indentation force-depth curves, with many stiff outliers. Therefore unless the nanoscale features of the cell are critical to the aim of a cell mechanics study, the data obtained from intermediate or large sized AFM tips is more reliable. Furthermore in most contexts cell mechanics is of most interest at the length scale of the whole cell.

3.4.5 Materials and Methods

Sample preparation and AFM indentation

The UN protocol for cell culturing was followed. The cells were plated on a 50 mm polystyrene dish 48 hr prior to experiments (Fluorodish, World Precision Instruments, Sarasota, FL). AFM nanoindentation was performed by a MFP3D-BIO

AFM (Asylum Research, Santa Barbara, CA) mounted on an IX-71 inverted optical microscope (Olympus America, Center Valley, PA) equipped with an iXon^{+} EMCCD camera (Andor Technology, Belfast, Northern Ireland). Cells were indented with an MLCT probe (Bruker, Santa Barbara, CA) that has a soft (nominal spring constant k = 0.01 N/m) Si_xN_y cantilever with a sharp (nominal radius r = 10 nm) Si_xN_y tip. Measurements were performed in the growth medium at 37°C. Each cell was indented at one location over the cytoplasm chosen to insure that the region was relatively flat and not too close to any neighboring cells. At each location, the cell was indented 10 times, with 1 min between each indentation. The loading rate was 2 μm/s and the trigger force was 600 pN.

The same experiment was conducted using an intermediate sized LRCH-750 probe (Team NanoTec) (r = 680 nm, k = 0.214 N/m) wherein cells were indented 3-4 times over only the nuclear region. The loading rate was 2 μm/s and the trigger force (the applied force at which the probe is retracted) was 8.5 nN.

Data processing method

For all force-indentation curves, virtual deflection was corrected by fitting a line through the non-contact region and subtracting the force value of the fit line from the force value of the curve at every (F, d) coordinate. Contact points were determined and any pathological curves were filtered by visual inspection. For the most direct comparison with the results of other groups in a collaborative project, the Young's moduli were calculated with the Hertz model (for large tips) and conical model (for sharp tips) in a non-linearized fashion by fitting the data in the interval 0-

300 nm indentation depth range, using least-squares non-linear regression to find the best value of the modulus.

3.5 AFM Indentation Study of MCF7-B7 and MCF7-G11 Cells

3.5.1 Contributions

This work is in preparation for publication. The cell lines were developed and the Affymetrix gene expression profile microarray dataset was generated by Laura Gonzalez-Malerva. The cells were cultured and seeded on glass dishes for the measurements by Laura Gonzalez-Malerva. AFM-confocal measurements with sharp tips were conducted by myself and Nathan Banyai, whom I trained. AFM measurements with intermediate sized tips were conducted by myself. Some of the analysis methods and parts of the custom MATLAB programs used for the fitting were contributed by Bryant L. Doss. I analyzed the AFM data and gene expression data.

3.5.2 Overview

To investigate the influence of estrogen on the mechanical properties of estrogen receptor positive (ER+) breast cancer cells, an atomic force microscope on an inverted optical microscope was used to indent over the nuclear regions of tamoxifen-resistant and tamoxifen-sensitive subclones of the MCF7 cell line after 24 h incubation in presence and absence of 17β-estradiol (E2) and 4-hydroxytamoxifen (4-OHT). Addition of tamoxifen resulted in 27-28% stiffening relative to estrogen alone in both subclones. Addition of tamoxifen and removal of estrogen resulted in 39-44% stiffening relative to estrogen alone in both subclones. Interestingly, absence of both estrogen and tamoxifen resulted in 60% relative stiffening of tamoxifen-resistant cells, but tamoxifen-sensitive cells' stiffness did not differ significantly from those in estrogen alone. Taken together, these observations suggest that both

estrogen and tamoxifen have non-trivial effects on cellular elasticity, and that estrogen signaling plays an important role in ER+ breast cell mechano-transduction--especially in tamoxifen-resistant cells.

Breast cancer remains the second most common cancer (second only to skin cancer) and the second most deadly cancer (second only to lung cancer) for women in the United States. In recent years a more sophisticated picture of the disease has emerged, in which several molecular subtypes are distinguished based on expression profiles of estrogen receptors (ERα, ERβ), progesterone receptor (PR), epidermal growth factor receptors (HER1, HER2), and epithelial keratins (CK 5/6). The most common subtypes, luminal A and luminal B, both express ER and display estrogen-dependent proliferation (ER+). The most common therapeutic treatment for such ER+ breast cancers is the cytostatic ER antagonist tamoxifen. Metabolites of tamoxifen such as 4-hydroxytamoxifen (4-OHT) bind ER with high affinity, inhibiting ER binding by estrogens like 17β-estradiol by direct competition. Unfortunately, half of patients with advanced ER+ breast cancers exhibit intrinsic *de novo* resistance to the drug, while the other half acquire resistance over time. It is therefore of high interest to investigate the nature of tamoxifen resistance. Here the connections between estrogen-mediated cell mechanics and tamoxifen resistance are explored.

The MCF7 cell line is frequently studied as a model system for ER+ breast cancers. It was derived from a malignant pleural effusion originating in a luminal epithelial invasive ductal carcinoma (IDC). These cells express cytoplasmic ER and are proliferative and tumorigenic in mouse only with estrogen available to them.

3.5.3 Results

In the present work, mechanical properties of tamoxifen-sensitive MCF7-B7^{TamS} and tamoxifen-resistant MCF7-G11^{TamR} cells after 24 h of incubation in media with E2 (+EST, −TAM), 4-OHT (+TAM), neither (−EST, −TAM), and both (+EST, +TAM) were measured[208]. The experimental design with media conditions are related schematically in Figure 3.14.

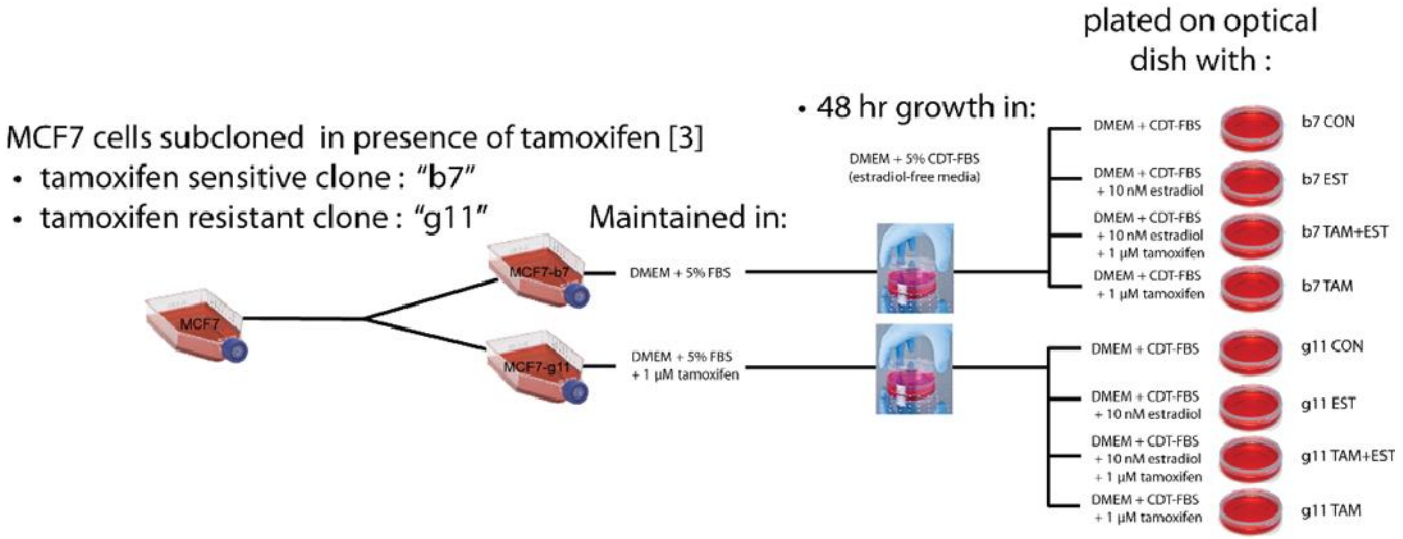

MCF7 cells subcloned in presence of tamoxifen [3]
• tamoxifen sensitive clone : "b7"
• tamoxifen resistant clone : "g11"
Maintained in:
MCF7
MCF7-b7
MCF7-g11
DMEM + 5% FBS
DMEM + 5% FBS + 1 µM tamoxifen
• 48 hr growth in:
DMEM + 5% CDT-FBS (estradiol-free media)
plated on optical dish with :
DMEM + CDT-FBS
b7 CON
DMEM + CDT-FBS + 10 nM estradiol
b7 EST
DMEM + CDT-FBS + 10 nM estradiol + 1 µM tamoxifen
b7 TAM+EST
DMEM + CDT-FBS + 1 µM tamoxifen
b7 TAM
DMEM + CDT-FBS
g11 CON
DMEM + CDT-FBS + 10 nM estradiol
g11 EST
DMEM + CDT-FBS + 10 nM estradiol + 1 µM tamoxifen
g11 TAM+EST
DMEM + CDT-FBS + 1 µM tamoxifen
g11 TAM

Figure 3.14: Experimental Design. Estrogen was depleted from the growth media of tamoxifen-resistant and –sensitive subclones for 48 h. The media was then exchanged with media buffered with 25 mM HEPES containing 10 nM estradiol, 1 μM 4-OHT, neither, or both. Cells were incubated 24 h before AFM indentation measurements.

An atomic force microscope was used to indent live adherent cells with a soft cantilever ($k = 0.134$ N/m), and large tip ($r = 815$ nm, $h \sim 15$ μm) in a $(\sim 2.5\ \mu m)^2$ 2 × 2 grid over the nuclear region.

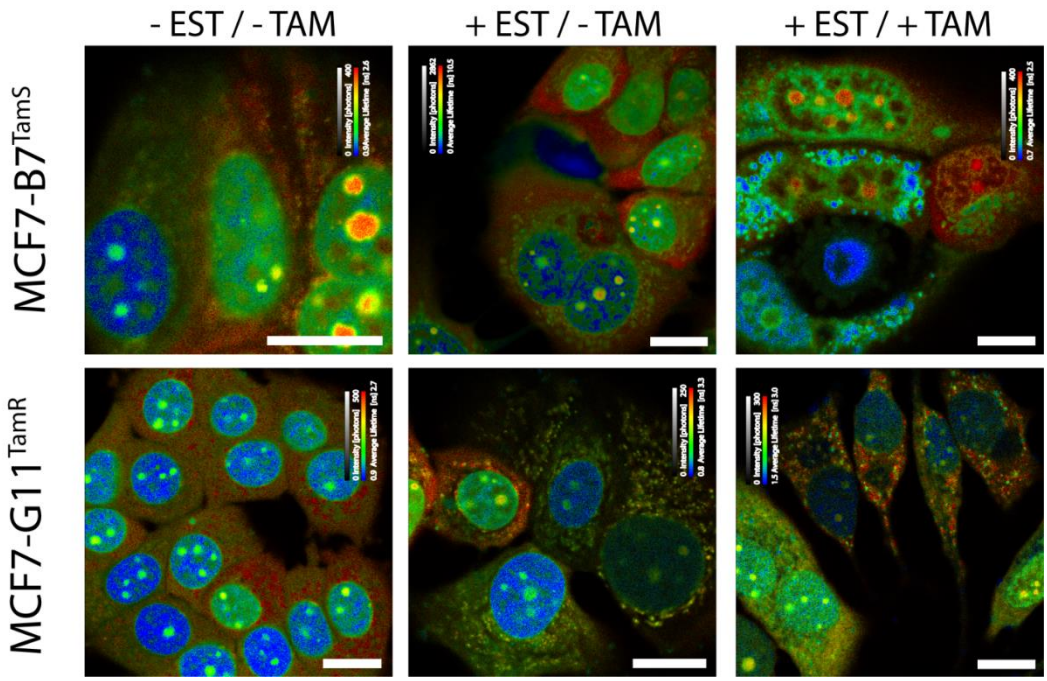


Figure 3.15: Fluorescence lifetime/intensity micrographs. MCF7-B7TamS (top) and MCF7-G11TamR (bottom) cells after 72 hours incubation in estrogen depleted (left), estrogen replete (middle), and estrogen blocked (right) growth media. Cells are stained with nuclear and nucleolar dyes, simultaneously excited by red and blue lasers and detected on two SPADs. Here the two channels are integrated. Pixel color: averaged fluorescence lifetime. Pixel brightness: summed fluorescence intensity. Scale bars: 10 μm.

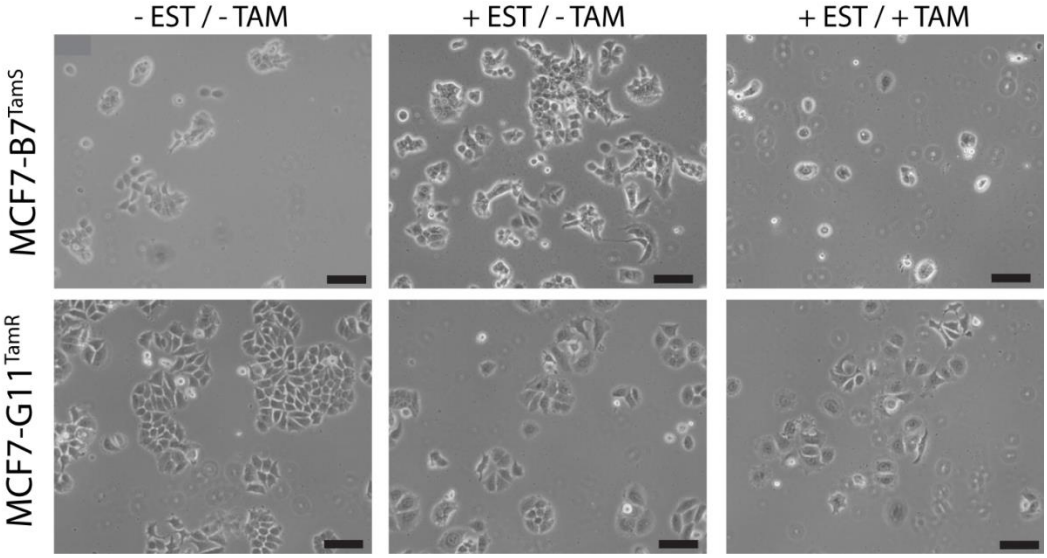


Figure 3.16: Phase contrast micrographs. MCF7-B7^{TamS} and MCF7-G11^{TamR} cells after 72 hours incubation in estrogen depleted, estrogen replete, and estrogen blocked growth media. 10× magnification. Scale bars: 100 μm. Images courtesy of Laura Gonzalez-Malerva.

Tamoxifen Sensitivity and Proliferation

In all four conditions, MCF7-G11^{TamR} cells appear to have normal morphologies and comparable proliferation. In E2-depleted and 4-OHT-treated conditions, MCF7-B7^{TamS} cell counts are relatively low, with morphologies more frequently indicative of senescence and apoptosis. These findings are in agreement with the phenomenological tamoxifen sensitivity and resistance of the two subclones. It is important to consider here that there is, as such, an intrinsic selection bias in these experiments, insofar as there are relatively fewer MCF7-B7^{TamS} cells available to measure in estrogen-depleted and estrogen-blocked conditions, and those cells may be in accordingly stressed or abnormal states. To decouple these factors, only the most morphologically normal cells (i.e., elongated cells with thin, well-adhered protrusions from either end) were selected for measurement. Cells close enough to neighbors for cell-cell signaling were preferntially selected for indentation. Another consideration is that the deformation induced by indentation of a cell in a cluster could be influenced by transduction of forces at intercellular junctions. Only small regions over the cell nuclei, far from cell-cell boundaries were probed; moreover, the deformation was localized to within ~2 μm and therefore mechanical boundary conditions imposed by neighboring cells can be neglected, as discussed by Boulbitch[209].

Elasticity

Each force-indentation curve is linearized and fitted piecewise as in §3.2 to a contact model for a spheroconical tip (described in §3.6). This approach was used to obtain a single (depth-independent) value for the elastic modulus for each curve by fitting the curve in the 0.25-2.5 μm indentation range (Table 3.3, Figs. 3.17 and 3.18). To obtain the apparent Young's modulus as a function of indentation depth, curves were segmented uniformly and fit in 0.25 μm intervals from the contact point (Fig. 3.19).

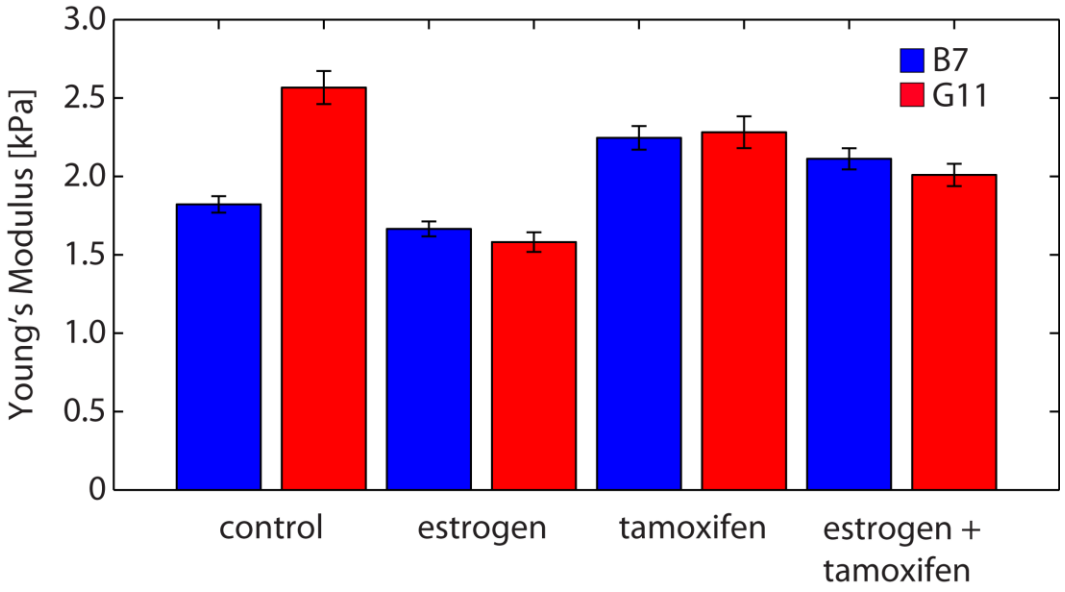


Figure 3.17: Young's moduli (mean ± s.e.) of MCF7-B7^{TamS} and MCF7-G11^{TamR} cells with and without estrogen and tamoxifen.

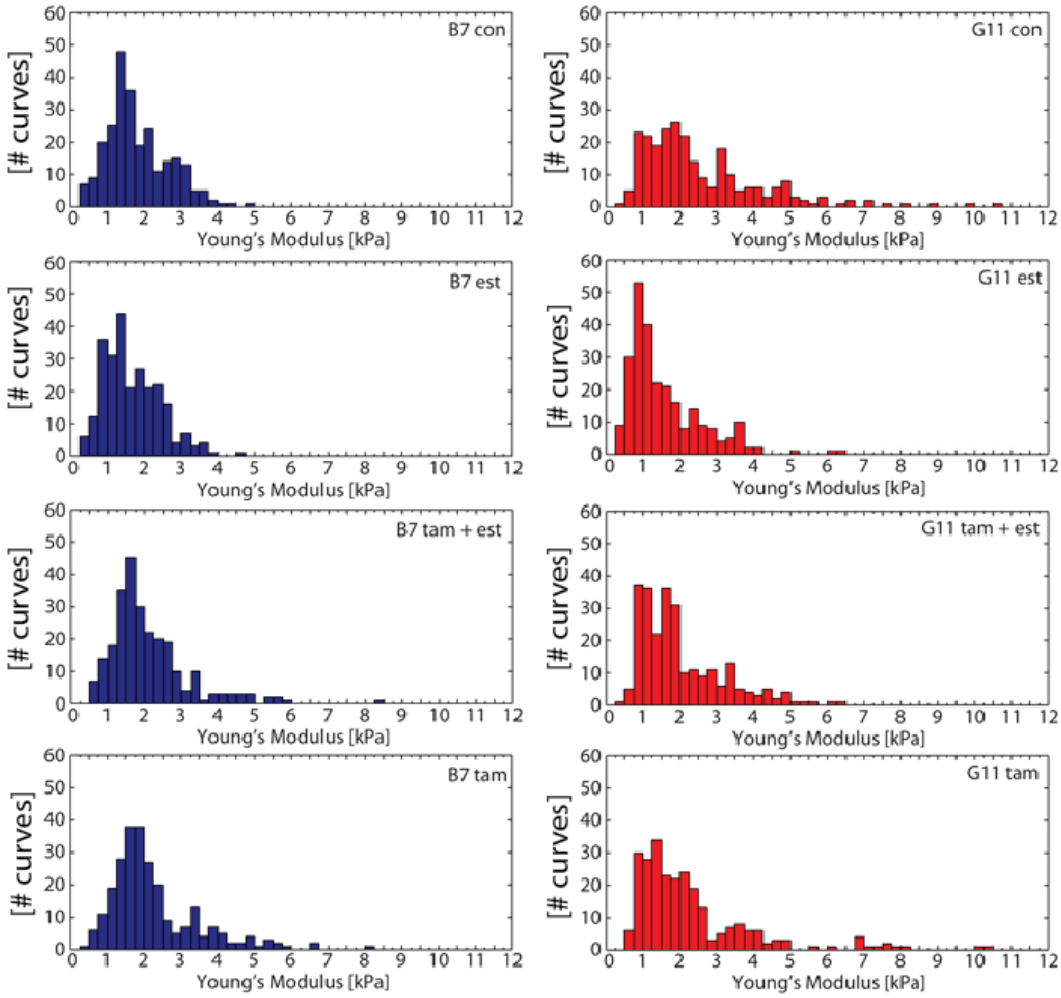


Figure 3.18: Histograms of Young's moduli of MCF7-B7^{TamS} and MCF-G11 cells with and without estrogen and tamoxifen.

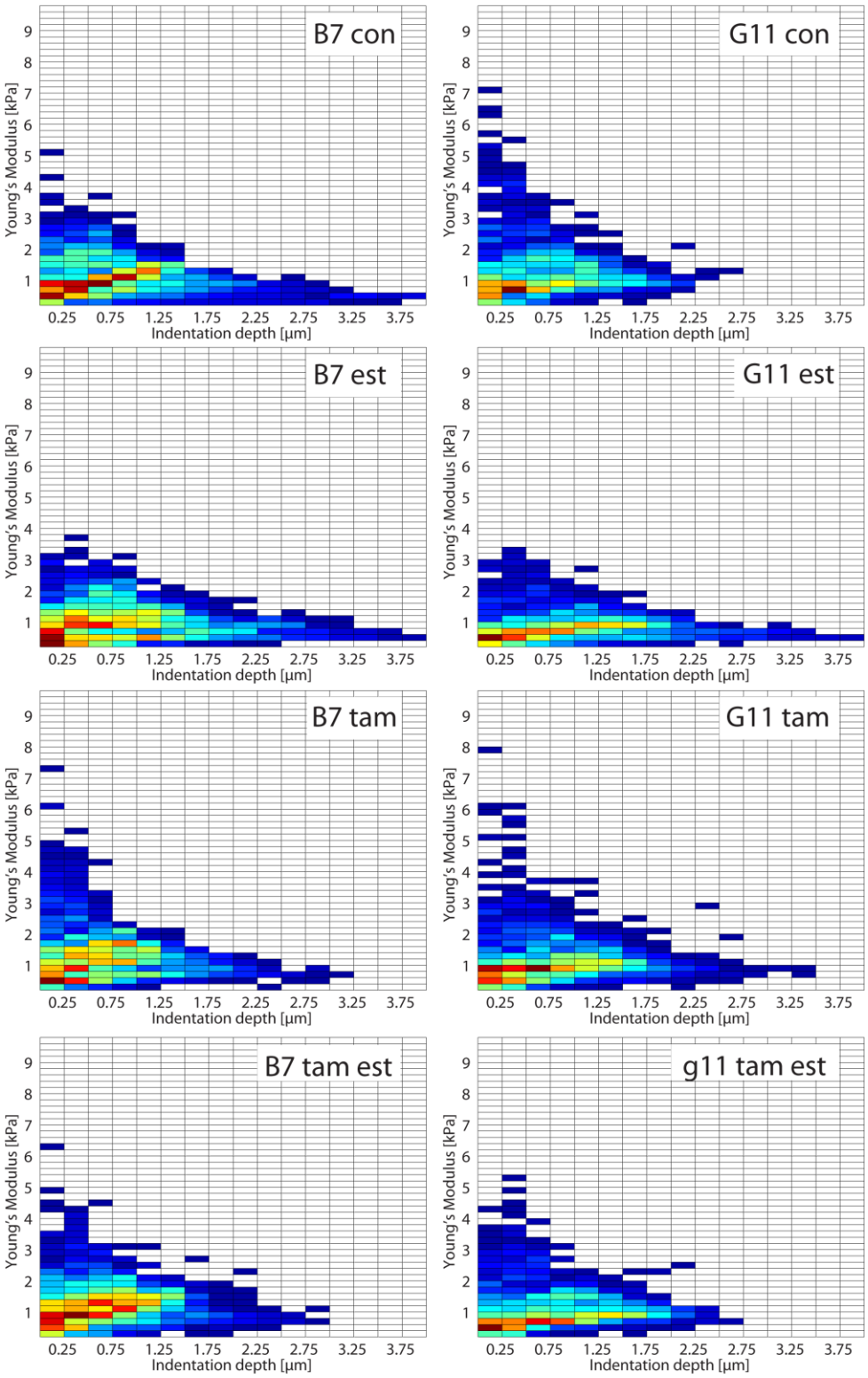

B7 con
G11 con
B7 est
G11 est
B7 tam
G11 tam
B7 tam est
g11 tam est
Young's Modulus [kPa]
Indentation depth [µm]
0.25 0.75 1.25 1.75 2.25 2.75 3.25 3.75
1 2 3 4 5 6 7 8 9

Figure 3.19: 2D histograms (Young's modulus vs. indentation depth) of MCF7-B7^{TamS} and MCF-G11 cells with and without estrogen and tamoxifen.

MCF7-B7^{TamS} cells in (+EST, -TAM) conditions had a mean Young's modulus of ~1.7 kPa, significantly ($p \sim 1 \cdot 10^{-8}$) stiffer (27%) with tamoxifen addition in (+EST, +TAM) conditions, and significantly ($p \sim 1 \cdot 10^{-11}$) stiffer yet (39%) with tamoxifen addition and estrogen depletion in (-EST, +TAM) conditions. Interestingly, estrogen depletion alone in (-EST, -TAM) conditions resulted in only 9% stiffening ($p=0.028$) (see Table 3.3).

The Young's moduli of MCF7-G11^{TamR} cells did not differ statistically significantly from MCF7-B7^{TamS} cells in (+EST, -TAM), (+EST, +TAM), (-EST, +TAM) conditions. They exhibit the same trend of stiffening slightly (28%) with the addition of tamoxifen and moreso (44%) with the addition of tamoxifen and the removal of estrogen. However, unlike the MCF7-B7^{TamS} cells, they stiffen even further (62%) in the absence of both estrogen and tamoxifen. MCF7-B7^{TamS} cells thus appear mechanically responsive to tamoxifen but not estrogen deprivation, whereas of MCF7-G11^{TamR} cells appear mechanically responsive to both tamoxifen and estrogen.

Subclone	Condition	Young's Modulus [Pa]	
		Mean ± S.E.	Median
MCF7-B7^{TamS}	(-EST, -TAM)	1822 ± 53	1622
	(+EST, -TAM)	1665 ± 48	1496
	(-EST, +TAM)	2316 ± 82	1918
	(+EST, +TAM)	2112 ± 68	1839
MCF7-G11^{TamR}	(-EST, -TAM)	2567 ± 105	2070
	(+EST, -TAM)	1581 ± 62	1215
	(-EST, +TAM)	2282 ± 101	1846
	(+EST, +TAM)	2028 ± 71	1691

Table 3.3: Young's Moduli of MCF7-B7 and MCF-G11 Cells with and without Estrogen and Tamoxifen.

Contact Point Determination

In the elastic analysis of a force-indentation curve, the results are highly dependent on the accurate determination of the contact point. For this purpose, a simple but robust method was developed. First the extension curve is represented as an n × 2 array of (F, δ) coordinates. They are then put into a distribution based only on their F-values. Because the baseline is ideally flat and there are many more data points on the baseline than in the contact region of the curve, the distribution should be sharply peaked around the force value of the baseline. This will remain true even if there is a slight slope to the baseline due to so-called 'virtual deflection', or in the case of some other artifacts, albeit with a broader peak. The resulting probability distribution is then fit with a kernel smoothing density estimate, whose fit parameters serve as a convenient representation of the distribution. From the fit, the peak F-value is found, as well as F-values bounding the full-width at half-maximum (FWHM). Then, the subset of only those (F, δ) coordinates whose F-values fall

within the FWHM are taken from the curve and a linear fit is performed on the subset. The resulting fit line is considered to be the baseline of the extension curve. The baseline is extrapolated in both directions from end to end. The contact point is then taken to be the (F, δ) coordinate of the extension curve with the largest δ-value at which the F-value of the baseline is greater than that of the extension curve. In a home-built program with a custom graphical user interface, every curve, along with its contact point and baselines, was visually inspected to ensure accurate fitting before further analysis.

Gene Expression Analysis

To further investigate mechanisms of estrogen's influence on cell mechanics, the microarray dataset publicly available through the Gene Expression Omnibus, GSE 26459[208] was studied. The main findings are simplified in Table 3.4. Tables B1-B8 in Appendix B list the fold-changes and p-values of all genes considered below.

Upregulated in Resistant Cells compared to Sensitive Cells	Downregulated in Resistant Cells compared to Sensitive Cells
Solute carrier proteins; Radixin; RhoA; RhoB; Spectrin; Filamin A; Filamin B; MAPK3; PKC-alpha; NCOA3	Ezrin; Moesin; Destrin

Table 3.4: Differential Regulation of Genes of Interest in Tamoxifen Resistant Cells.

As shown in Tables B1 and B2, microarray profiling revealed significantly differential expression of many solute carriers (SLC proteins), including sodium-hydrogen ion exchangers. NHE3 (*SLC9A7*) was expressed significantly less (by factors from ~1.45 to ~2.25) in MCF7-G11^{TamR} than MCF7-B7^{TamS} regardless of treatment. Expression levels in MCF7-B7^{TamS} were sensitive to tamoxifen: MCF7-B7^{TamS} NHE3 expression

was ~1.4-fold less in (+EST, +TAM) conditions than in (+EST, -TAM) conditions, while MCF7-B7^{TamS} NHE2 (*SLC9A2*) expression was ~1.33-fold more in (+EST, +TAM) conditions than in (+EST, -TAM) conditions. NHE1 (*SLC9A1*) expression levels changed by factors less than 1.3 and/or with p-values ≥ 0.05. The many changes in solute carrier expression suggest fundamental changes in the cellular milieu of various metals and ions, which may contribute to the tamoxifen resistance of the MCF7-G11^{TamR} cell line.

Table B3 shows differential expression of genes for ERM family actin-binding proteins as well as Rho GTPases. Moesin (*MSN*) and ezrin (*EZR*) expression were significantly elevated in MCF7-G11^{TamR} with respect to MCF7-B7^{TamS} regardless of treatment, by factors ~3–3.8 and ~1.3–1.7, respectively. Ezrin expression levels in MCF7-B7^{TamS} were sensitive to tamoxifen: MCF7-B7^{TamS} ezrin expression was ~1.5-fold less in (+EST, +TAM) conditions than in (+EST, −TAM) conditions. On the other hand, radixin (*RDX*) expression was significantly reduced in MCF7-G11^{TamR} with respect to MCF7-B7^{TamS} regardless of treatment, by factors ~1.3–1.8. These changes may reflect differences in the degree of crosslinking of cortical actin with the plasma membrane in the two subclones. In addition, RhoA (*RHOA*) and RhoB (*RHOB*) expression levels were both reduced in MCF7-G11^{TamR} with respect to MCF7-B7^{TamS} regardless of treatment, by factors ~2.25–2.33 and ~1.33–2, respectively. Rho GTPases regulate actin dynamics in various ways, e.g. via ROCK1-mediated cofilin stimulation. Differential Rho expression may therefore reflect differences in degree of stress fiber formation in the two subclones.

Other important actin binding proteins were differentially expressed as well, as shown in Table B4. Expression levels of spectrin (*SPTBN1*), which anchors actin filaments to the plasma membrane, were significantly reduced ~2.9-fold and ~1.8-fold in MCF7-G11^{TamR} with respect to MCF7-B7^{TamS} in (+EST, −TAM) and (+EST, +TAM) conditions, respectively. Spectrin expression levels in MCF7-B7^{TamS} were sensitive to tamoxifen: (+EST, +TAM) levels were ~1.8-fold greater than (+EST, −TAM) levels. Expression levels of the actin filament cross-linkers Filamin A (*FLNA*) and filamin B (*FLNB*) were significantly reduced in MCF7-G11^{TamR} with respect to MCF7-B7^{TamS} in (+EST, −TAM) conditions by factors of ~1.4 and ~2.0, respectively. The actin depolymerizing factor destrin (*DSTN*) was expressed ~1.4−2.1-fold more in MCF7-G11^{TamR} than in MCF7-B7^{TamS} in all conditions.

As shown in Table B5, Catechol-O-methyltransferase (*COMT*) expression was significantly reduced ~1.5-fold in MCF7-G11^{TamR} with respect to MCF7-B7^{TamS} in (−EST, +TAM) conditions. On the other hand expression in (+EST, +TAM) conditions was ~1.5-fold more in MCF7-G11^{TamR} than in MCF7-B7^{TamS}. This suggests *COMT* levels are more sensitive to estrogen in MCF7-G11^{TamR} than in MCF7-B7^{TamS}. MCF7-G11^{TamR} *COMT* expression varied with estrogen availability: levels were ~1.4-fold lower in (−EST, +TAM) than in (+EST, −TAM) conditions, and ~1.5- to 1.8-fold greater in (+EST, +TAM) conditions than in (−EST, −TAM) and (−EST, +TAM) conditions. MCF7-B7^{TamS} expression was tamoxifen-sensitive: levels were ~1.5-fold less in (+EST, +TAM) than in (+EST, −TAM). Taken together these observations indicate that catechol-O-methyltransferase levels vary with estrogen availability. In the simplest scenario, 2ME2 levels should also vary with

estrogen availability. Accordingly, increased estrogen would lead to increased 2ME2, which would lead to microtubule depolymerization and increased cell deformability.

As shown in Table B6, PKC-α (*PRKCA*) expression was significantly reduced by factors ~1.5–1.8 in MCF7-G11^{TamR} with respect to MCF7-B7^{TamS} regardless of treatment. PKC-α expression levels in MCF7-G11^{TamR} were tamoxifen-sensitive: expression is ~1.3-fold more in (+EST, +TAM) conditions than in (+EST, −TAM) conditions. Expression of proteins downstream of PKC-α are shown in Table B7. Many mitogen-activated protein kinases were significantly differentially expressed between the subclones and treatment types. For example, MAPK3 expression was ~2−3.3-fold less in MCF7-G11^{TamR} than in MCF7-B7^{TamS} regardless of treatment. MCF7-G11^{TamR} MAPK3 expression was tamoxifen-sensitive: levels were ~1.6-fold lower in (+EST, +TAM) than in (+EST, −TAM) conditions. This is not representative of MAPK signaling, as many other MAPK proteins displayed different trends. NFκB (*NFKB2*) expression was significantly reduced 1.4-fold in MCF7-G11^{TamR} with respect to MCF7-B7^{TamS} in (+EST, −TAM) conditions. In (−EST, +TAM) conditions, bcl-2 (*BCL2*) was expressed ~1.4-fold less in MCF7-G11^{TamR} than in MCF7-B7^{TamS}. p21^{cip1} (*CDKN1A*) expression was ~1.5-fold less in MCF7-G11^{TamR} than in MCF7-B7^{TamS} in (+EST, −TAM) and (−EST, +TAM) conditions, but ~1.8-fold greater in (+EST,+TAM) conditions. In MCF7-G11^{TamR}, p21^{cip1} expression was ~1.5-fold greater in (+EST, +TAM) than in all other conditions. These observations—lower expression of PKC-α and many downstream signaling molecules—thus conflict with the hypothesis that overexpression of PKC-α is required for tamoxifen resistance.

While the relative activation states of PKC-δ in the microarray experiments is unknown, PKC-δ (*PRKCD*) expression levels changed by factors less than 1.3 and/or with *p*-values >=0.05. This observation, together with the ambiguity of the changes in MAPK expression, does not seem to support the hypothesis of PKC-δ based tamoxifen resistance.

Some other PKC isoforms (See Table B6) showed decreased expression in MCF7-G11^{TamR} with respect to MCF7-B7^{TamS} . Both PKC-η (*PRKCH*) and PKC-ι (*PRKCI*) expression in (+EST, −TAM) conditions was ~1.4-fold less in MCF7-G11^{TamR} than in MCF7-B7^{TamS}. PKC-γ (*PRKCG*) expression in both (−EST, +TAM) and (+EST, +TAM) conditions was ~1.5-fold less in MCF7-G11^{TamR} than in MCF7-B7^{TamS}. On the other hand, PKC-ζ (*PRKCZ*) expression in (+EST, +TAM) conditions was ~1.4-fold higher in MCF7-G11^{TamR} than in MCF7-B7^{TamS}. Interestingly, MCF7-G11^{TamR} expression of some PKC isoforms was estrogen-senstive. PKC-η expression in MCF7-G11^{TamR} was ~1.4-fold greater in (-EST, -TAM) conditions than in (+EST, −TAM) conditions. PKC-θ (*PRKCQ*) in MCF7-G11^{TamR} was ~1.3-fold less in (−EST, +TAM) than in (+EST, +TAM) conditions.

As shown in Table B8, PAX2 expression levels were ~1.7 to 1.8-fold more in MCF7-G11^{TamR} than in MCF7-B7^{TamS} in all conditions. AIB-1/SRC-3 (*NCOA3*) levels were ~1.5−1.8-fold more in MCF7-G11^{TamR} than in MCF7-B7^{TamS} in all conditions. GPR30 (*GPER*) expression levels changed by factors less than 1.3 and/or with *p*-values >=0.05.

3.5.4 Discussion and Conclusions

MCF7 cell elasticity

Lim and co-workers previously measured the elasticity of MCF7 cells by AFM indentation with a micro-sized, spherical probe, and found their apparent Young's modulus to range from ~300–600 Pa, increasing slightly with loading rate[10]. Considering experimental differences including loading rate, probe geometry, analysis methods, and the type of MCF7 clones used, our findings are in reasonable agreement. In §3.4, the elasticity of standard MCF7 cells (ATCC, Cat. No. HTB-22) was measured in growth medium on polystyrene with a sharp probe and fit with a conical contact model, as well as with a similar intermediate sized tip using the Hertz model[14]. The (sharp tip) pointwise elastic modulus values of MCF7 cells reported there were ~800 Pa at indentation depths of 200–300 nm, about half the mean value of MCF7-B7^{TamS} in (+EST, −TAM) conditions reported here[14]. For the intermediate sized probes, both subclones are significantly stiffer than the wild-type MCF7 cells. This discrepancy may be due to the different models used, different indentation ranges fitted, differences in integrin activation and concommitant changes in cytoskeletal tension due to the different substrates, to the media in which they were measured, or to differences in their culturing prior to the experiments.

Estrogen-induced cell softening

Osmosis and membrane tension

The relationship between estrogen and cell elasticity remains largely unexplored. Hillebrand *et al.* found that human umbilical vascular endothelial cell (HUVEC) elasticity increased by 50 % in response to E2[210]. Sodium channel blockers were found to abolish the effect. According to the authors, a change in the antiport set-

point of the ubiquitously expressed Na^+/H^+ exchanger NHE1, brought about in response to E2, decreases intracellular $[H^+]_i$ and increases intracellular $[Na^+]_i$, resulting in an osmotic influx of water. The observed increase in cell volume brings about a rounding up of the cell, and the authors invoke the Laplace law to explain the attendant increase in elasticity.

pH and the cytoskeleton

If the NHE1 hypothesis above is correct, then in addition to the osmotically-driven mechanical changes, the increased intracellular alkalinity brought about by NHE1-induced H^+ efflux would affect the cell in many other ways as well. For example, the dynamics of actin polymerization are pH-dependent (see §2.2.1). While the kinetics are highly sensitive to cation identities and concentrations, *in vitro* actin self-assembly has been shown to be substantially accelerated at lower pH[60]. In addition, pH is known to control the actin binding of proteins such as cofilin, which depolymerizes more F-actin at higher pH[61,211]. Therefore, increases in intracellular pH induced by NHE1 and other ion channels are likely to shift the balance toward a sparser and hence more deformable actin cortex.

NHE1 and actin-binding proteins

Estrogen-mediated NHE1 activation may directly alter the actin cytoskeleton, as well. Denker *et al.* found that NHE1 directly associates with actin binding proteins such as ezrin, radixin, and moesin via its intracellular C-terminal domain. NHE1 was shown to anchor the actin cortex to the plasma membrane in the leading edge of lamellopodia in fibroblasts[212]. Furthermore, NHE1 is involved in focal adhesion assembly, stress fiber formation, and cell shape change via the RhoA signaling

pathway. This suggests NHE1 may play an important role both upstream and downstream of actin cortex reorganization[213].

Estrogen metabolism and microtubule stability

Another intriguing connection between estrogen and cell stiffness consists in the effect of 2-methoxyestradiol (2ME2) on microtubules. E2 is hydroxylated by P450 cytochromes, and the hydroxylated derivatives are then converted to 2ME2 by catechol-O-methyltransferase[214]. 2ME2 has been shown to disrupt microtubule networks[215,216,217] and to suppress microtubule dynamics[218,219]. Microtubules have been shown to play a significant mechanical role in the cell (see §2.2.1). Thus, estrogen metabolites may increase cell deformability by depolymerizing microtubules. In addition to their direct mechanical role, microtubules are critical to intracellular kinase signaling, GTP stoichiometry and transmembrane ion channel function, all of which have downstream effects on mechanical properties[38].

Estrogen may therefore increase cellular elasticity by many independent mechanisms:

(i) by altering the set-point of ion antiporters like NHE1, estrogen can bring about an osmotic influx of water that increases cell volume and cell membrane and cortex elasticity;

(ii) this process may also alter the interactions of NHE1 either with ERM (ezrin/radixin/moesin) proteins, which cross-link actin filaments with the plasma membrane, or with the Rho pathway, which regulates cell shape and the actin cytoskeleton;

(iii) by raising the pH, the change in antiporter set-point may diminish actin self-assembly and enhance actin depolymerization (see §2.1.1);

(iv) estrogen may be metabolized to form 2ME2, which has been found to depolymerize microtubules, a process that reduces cell stiffness.

The estrogen-depletion-induced cell stiffening of both subclones observed in the present study is therefore likely to be a robust effect caused by several independent cell-mechanical factors.

Tamoxifen Resistance

At first blush, it may seem that tamoxifen-resistant cells should be affected *less* by 4-OHT than tamoxifen-sensitive cells. However, the mechanical effects of E2 are not mediated by the classical estrogen receptors ERα and ERβ, to which tamoxifen competitively and antagonistically binds. Rather, (i) microtubule stability is altered directly by 2ME2 (as discussed above), and (ii) estrogen-mediated NHE1 activation is thought to be a rapid, non-genomic effect of 17β-estradiol directly interacting with the protein kinase C isoforms PKC-α and PKC-δ[220]. Although there is no indication of direct phosphorylation of NHE1 by PKC, PKC inhibition has been shown to block NHE1 activation by EGF[221,213]. One should therefore not expect tamoxifen to recapitulate the mechanical effects of estrogen depletion. Then why does it do so in tamoxifen-resistant cells? Tamoxifen may interact with PKC agonistically or antagonistically. Hillebrand *et al.* found that tamoxifen abrogated estrogen-induced cell softening in HUVEC cells, suggesting antagonism[210]. On the other hand, in the ER− MDA-MB-231 cell line, tamoxifen has been shown to induce reversible recruitment of PKC to the plasma membrane[222] (where it is most likely to activate NHE1), suggesting agonism. Metabolized tamoxifen (i.e., 4-OHT) has been shown to irreversibly inactivate PKC isoforms *in vitro* via an oxidative process that can be blocked by anti-oxidants[222]. Evidently PKC-tamoxifen interactions are sensitive to both cellular metabolism and the redox state of the cellular milieu. Critically, the

acquisition of tamoxifen-resistance has been associated in MCF7 xenograft mouse tumors with both increased oxidative stress and decreased antioxidant capacity[223]. 4-OHT-mediated inhibition of estrogen-induced cell softening may therefore be due to relatively high oxidative stress that enables 4-OHT to inactivate PKC.

A key observation of the present study is that tamoxifen significantly inhibits estrogen-induced cell softening.

PKC and tamoxifen resistance

In addition to their roles in NHE1 activation discussed above, both PKC-α and PKC-δ have been implicated in conferring tamoxifen resistance. Specifically, Tonetti *et al.* found that PKC-α imparted tamoxifen resistance in T47D:A18 breast cancer cell lines, but that PKC-δ did not[224]. Several molecules downstream of PKC-α signaling have been associated with tamoxifen resistance, including AP-1, PI3K/Akt, MAPK, NFκB, and the anti-apoptotic proteins bcl-2 and $p21^{cip1}$ [224]. In contrast, Reddy *et al.* showed tamoxifen-resistant MCF7 cells and xenograft tumors expressed significantly higher total and activated PKC-δ than tamoxifen sensitive counterparts, and furthermore that forced overexpression of PKC-δ in tamoxifen-sensitive MCF7 cells reduced tamoxifen-induced growth inhibition from ~75% down to ~25%[225]. The authors suggest that overexpression of active PKC-δ provides an alternate path to activate MAPK signaling and thus tamoxifen-resistant growth[225]. The discrepancy suggests the two isoforms may lead to tamoxifen resistance by different molecular mechanisms, and calls for further study[224].

GPR30 and tamoxifen resistance

Other mechanisms have also been shown to give rise to tamoxifen resistance. One such mechanism implicates the G-protein-coupled membrane estrogen receptor 1

(GPR30). Tamoxifen has been shown to be an agonist of GPR30[226,227]. Tamoxifen resistance (*viz.*, cell proliferation in presence of tamoxifen) has been attributed to GPR30, which transactivates EGFR, thus providing an alternative growth pathway [227]. Additionally, dose response curves have revealed that tamoxifen-resistant MCF7 cells display relatively enhanced growth sensitivity to estrogen, as well as to GPR30 agonist G1[227]. Interestingly, estrogen stimulated the translocation of GPR30 to the cell membrane in tamoxifen-resistant MCF7 cells, but not in tamoxifen-sensitive cells[227]. In another study by Jordan *et al.*, GPR30 was found to induce sustained increases in cytosolic calcium ion concentrations in MCF7 cells[228]. This effect is likely to produce osmotic influx of water and increase cell volume. A 200–350% volume increase was shown by Quist *et al.* to accompany decreased extracellular calcium ion concentration in BICR-MIR$_k$ (a rat epithelial mammary tumor cell line)[229]. However, contrary to Hillebrand *et al.*, these authors claim an associated ~50 % decrease in cell elasticity. This inconsistency may reflect either tissue or species specificity or the manifold downstream effects of calcium ion signaling.

ER/EGFR crosstalk

There are yet other mechanisms known to be involved in acquisition of tamoxifen resistance. ER/EGFR crosstalk was elucidated at the transcriptional level in terms of stoichiometric competition between tamoxifen-recruited ERBB2 repression by PAX2 and ERBB2 activation by the ER co-activator AIB-1/SRC-3[230]. Yet clarification of the complex interactions in these pathways, including the transcriptional activities of ER and GPR30, requires further study[231].

Conclusion

In §3.5, estrogen deprivation and tamoxifen treatment were found to result in up to ~60% relative cell stiffening in both tamoxifen-sensitive and tamoxifen-resistant ER+ MCF7 breast cancer cells. This observation is consistent with multiple independent cytomechanical effects of estrogen and tamoxifen.

Tamoxifen resistance, or more precisely, the retained ability to proliferative in presence of tamoxifen, does not imply a reduced sensitivity to estrogen *per se*. Taken together, these observations point to crosstalk between the mechanisms of estrogen-induced cell softening and tamoxifen resistance in ER+ breast cancer cells. Both estrogen and tamoxifen have non-trivial effects on cell elasticity, and accordingly estrogen signaling plays an important role in breast cancer cell mechano-transduction, especially in tamoxifen-resistant cells. This places cell mechanics in the line of sight in the fight against tamoxifen resistant breast cancer.

3.5.5 Materials and Methods

Cell Culture

The MCF7 metastatic breast cancer cell line was separated by limited dilution into tamoxifen-resistant and -sensitive subclones based on the ratio between their proliferation in media (DMEM supplemented with 5% FBS) with and without the addition of 1 μM 4-hydroxytamofixen (4-OHT) as described previously[208]. In the present study, two of these subclones, MCF7-G11^{TamR} (tamoxifen-resistant) and MCF7-B7^{TamS} (tamoxifen-sensitive), were maintained in DMEM supplemented with 5% FBS. 1 μM 4-OHT was added to the media of the resistant MCF7-G11^{TamR} cells.

Cells were passaged every 2-3 days, for which purpose cells were washed twice with PBS, trypsinized and replated.

Sample Preparation

Cells were plated onto 10 cm dishes and incubated for 48 h in steroid-depleted (phenol red free) DMEM supplemented with 5% steroid-depleted (charcoal-dextran treated) FBS (CDT-FBS) to ensure removal of estradiol. Cells were then split and ~10^3 cells were seeded on a 50 mm optical bottom dish. On the following day the media was exchanged with and incubated for 24 h in media corresponding to one of four experimental conditions: (i) (−EST, −TAM) steroid-depleted media (same as above); (ii) (+EST) steroid-depleted media + 10 nM 17β-estradiol; (iii) (+EST, +TAM) steroid-depleted media + 10 nM 17β-estradiol + 1 μM 4-OHT; (iv) (+TAM) steroid-depleted media + 1 μM 4-OHT. HEPES was added to each of these media at a concentration of 25 mM.

AFM Indentation

Measurements were conducted with an MFP3D-BIO (Asylum Research) mounted on an IX-71 inverted microscope (Olympus). Large radius (R = 815 nm) silicon AFM probes with nominal spring constants k = 134 pN/nm and long tips (h ~ 15 μm) are used for the indentation experiments (Team Nanotec). The spring constant of each cantilever was determined with the AFM software (Asylum Research, Santa Barbara, CA) by the thermal noise method[164,165]. A 100X oil objective was used to view the cells and the AFM probe through the eyepiece. The geometric center of the nucleus is brought directly under the AFM tip. In a $(\sim 2.5\ \mu m)^2$ region, a 2 × 2 grid of indentations is acquired with 2 μm/s approach and retract speeds in force volume mode with a trigger force of 3 nN, corresponding to total indentations ~2 – 4 μm

deep. For all experimental conditions, 64 cells from a single dish were measured, all using the same AFM probe and probe calibration.

AFM Data Analysis

All data was analyzed with home-built routines written in MATLAB 7.11 (The MathWorks, Natick, MA).

Analysis of Affymetrix Gene Expression Profile Dataset

In a previous work[208], MCF7-B7^{TamS} and MCF7-G11^{TamR} cells were incubated in estrogen depleted media and then treated in triplicate using one of four different conditions: (i) estrogen-depleted medium (control); (ii) estrogen (E) at 10 nM; (iii) 4-OHT at 1 μM; and (iv) E at 10 nM and 4-OHT at 1 μM. After 4 h, RNA was isolated and processed for gene-expression profiling according to the Affymetrix protocol (Human Genome U133 plus 2.0 Array) at the Microarray Core Facility at the Dana Farber Cancer Institute. For the present study, the entire microarray data set (accession no. GSE 26459) was downloaded from the Gene Expression Omnibus homepage. The library files, sequence, and annotation data specific to the array were downloaded from the Affymetrix homepage. MATLAB 7.11 Bioinformatics and Statistics Toolboxes were used for data analysis (The MathWorks, Natick, MA). Briefly, arrays of $\log_2$ based gene expression values were obtained from the .CDF and .CEL files using robust multi-array averaging (RMA) for background adjustment, quantile normalization and summarization procedures. Genes with low intensity, intrinsically low variation, or no annotation data were filtered out. Thereafter, differential gene expression was evaluated pairwise between relevant pairs of replicate sets (e.g., all MCF7-B7^{TamS} in (+EST, −TAM) vs. all MCF7-B7^{TamS} in (+EST, +TAM)) using a two-sample Student's *t*-test. Permutation methods (n =

10,000 permutations) were used to estimate the truly null distribution of the test statistics, yielding corrected *p*-values[232,233]. Only genes of biological interest that were differentially expressed with fold changes F such that $|F| \geq 1.3$ and corrected *p*-values such that $p \leq 0.05$ are considered in the text and listed in Tables B1-B8 in Appendix B.

3.6 MDA-MB-231 Cells in 3D Collagen Matrices

3.6.1 Contributions

This work is in preparation for publication. Collagen hydrogels were prepared by myself. Confocal reflection microscopy and characterization of the hydrogels were conducted by myself. Cells were cultured and seeded on hydrogels by Bryant L. Doss. AFM-CLSM measurements were conducted by Bryant L. Doss and myself. The two-layer correction method and spheroconical model were implemented in MATLAB by Bryant L. Doss. Finite element simulations were conducted by Bryant L. Doss. Data was analyzed by Bryant L. Doss and myself.

3.6.2 Overview

This section describes experimental measurements of Young's moduli of MDA-MB-231 cells partially and fully embedded in collagen I matrices. The analysis method enables separate accounting of the cell and gel material properties, so that the Young's moduli of cells partially or fully embedded within a layer of matrix can be quantified. To measure the Young's moduli of single cells embedded in hydrogels, a combined AFM and confocal fluorescence microscope setup is used (Figure 3.20A).

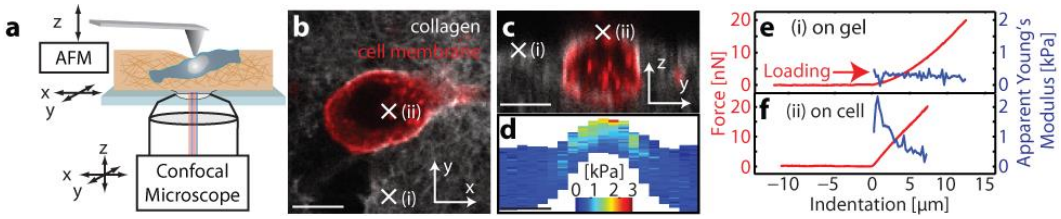


Figure 3.20: Combined AFM indentation and confocal fluorescence microscopy for elasticity measurements on embedded cells. (A) Schematic of AFM-CLSM setup. The AFM is sample scanning in the X and Y directions, and the objective of the confocal microscope is scanned in the X, Y, and Z directions. The AFM tip is aligned in the confocal volume prior to indentations and this alignment is preserved during the experiment when the sample is scanned. (B) Lateral (XY) and (C) axial (YZ) confocal fluorescence micrographs of an MDA-MB-231 cell partially embedded in collagen. The cell membrane (red) and collagen (white) are fluorescently labelled. (D) Spatially co-registered elasticity tomogram showing the apparent Young's moduli (fitted piecewise in 250 nm intervals of indentation depth) determined from indentations in the axial plane in (C). (E, F) Force-indentation curves (red) and corresponding apparent Young's moduli (blue) from points (i) and (ii). Scale bars: 10 μm.

The AFM tip is aligned with the laser focus to precisely determine the location of the nanoindentation[191]. 2D confocal scans are conducted in lateral (Figure 3.20B) and axial (Figure 3.20C) planes. AFM indentations are then conducted in the axial plane to generate spatially co-registered elasticity nanotomograms (Figure 3.20D) using raw force-indentation data and piecewise apparent Young's modulus on the collagen (Figure 3.20E) and apical cellular (Figure 3.20F) regions. An AFM probe with a large spheroconical tip (apex radius: ~750 nm; tip height: ~15 μm) is used to perform deep indentations with well-defined contact geometry (Figure 3.21).

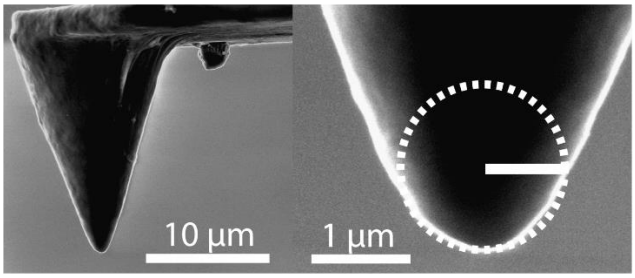


Figure 3.21: Scanning electron microscope image of an LRCH-750 tip (Team Nanotec). The image was taken with XL30 ESEM-FEG at the LeRoy Eyring Center at Arizona State University. The pictured tip has a measured half-angle of 18.8°, apex radius of 695 nm, and tip height ~ 15 µm.

3.6.3 Results

Collagen hydrogels

MDA-MB-231 breast cancer cells were seeded on top of fully polymerized collagen I matrices (initial concentrations ranging 2.44−4.88 mg·ml^{-1}) with Young's moduli ($E_{col.}$) ranging 0.1−5 kPa and subsequently measured after times ranging 6−96 h, during which time a majority of cells invaded the collagen either partially or fully. Neither the cells' NCPH nor their Young's moduli at times $t \leq 24$ h differed significantly from those at times $t \geq 49$ h ($p = 0.99$, $p = 0.37$, respectively), and there was significant overlap in the distributions of pericellular collagen stiffness from different concentrations (Figure 3.22), so data from all times and concentrations were pooled.

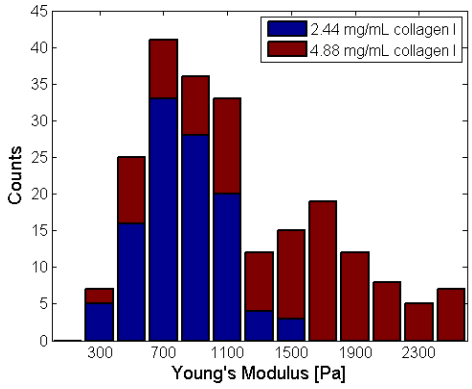


Figure 3.22: Histograms of Young's moduli of pericellular collagen from hydrogels formed at different initial collagen concentrations.

Gels had areal porosity ~70% and pore size ~0.5 ± 0.3 μm (Table 3.5, Figure 3.23). To quantify the gels' pore size distributions, four collagen hydrogels were prepared as described in the methods section, but were not stained with fluorescent dyes. After 24 h, the DPBS was removed from the gels and exchanged with growth media (to two of the dishes, 50 μl cell suspension was also added; one of the gels seeded with cells was also supplemented with 10 μM Y-27632) and incubated 96 h. Gels were then rinsed with DPBS and fixed with 3.7% paraformaldehyde in DPBS for 0.5 h (one of the two unseeded gels was left unfixed). The gels were then rinsed again in DPBS, covered in DPBS, and stored at 4 °C for 24 h. The gels were then imaged by confocal reflection microscopy with circularly polarized light. Samples were imaged by a 100X oil objective with 640 nm laser excitation of enough intensity to transmit reflected light through the dichroic mirror with sufficiently high signal:noise ratio. On each sample, ~20 10 μm × 10 μm scans (39 nm/pixel) were recorded. Resulting intensity bitmaps were imported as stacks and binarized in ImageJ[205] (Image>Adjust>Auto-Threshold [Mean; White objects on Black Background; Stack;

Use Stack Histogram]). Binarized images were then segmented (Process>Binary>Watershed). The pores were then analyzed (Analyze>Analyze Particles… [10-Infinity; 0.00-1.00; Pixel Units; Show Ellipses; Exclude on edges; Include holes]). The pore size of each ellipse was taken as the average length of its minor and major axes. The areal porosity was also calculated in ImageJ (Invert>Analyze>Measure>%Area).

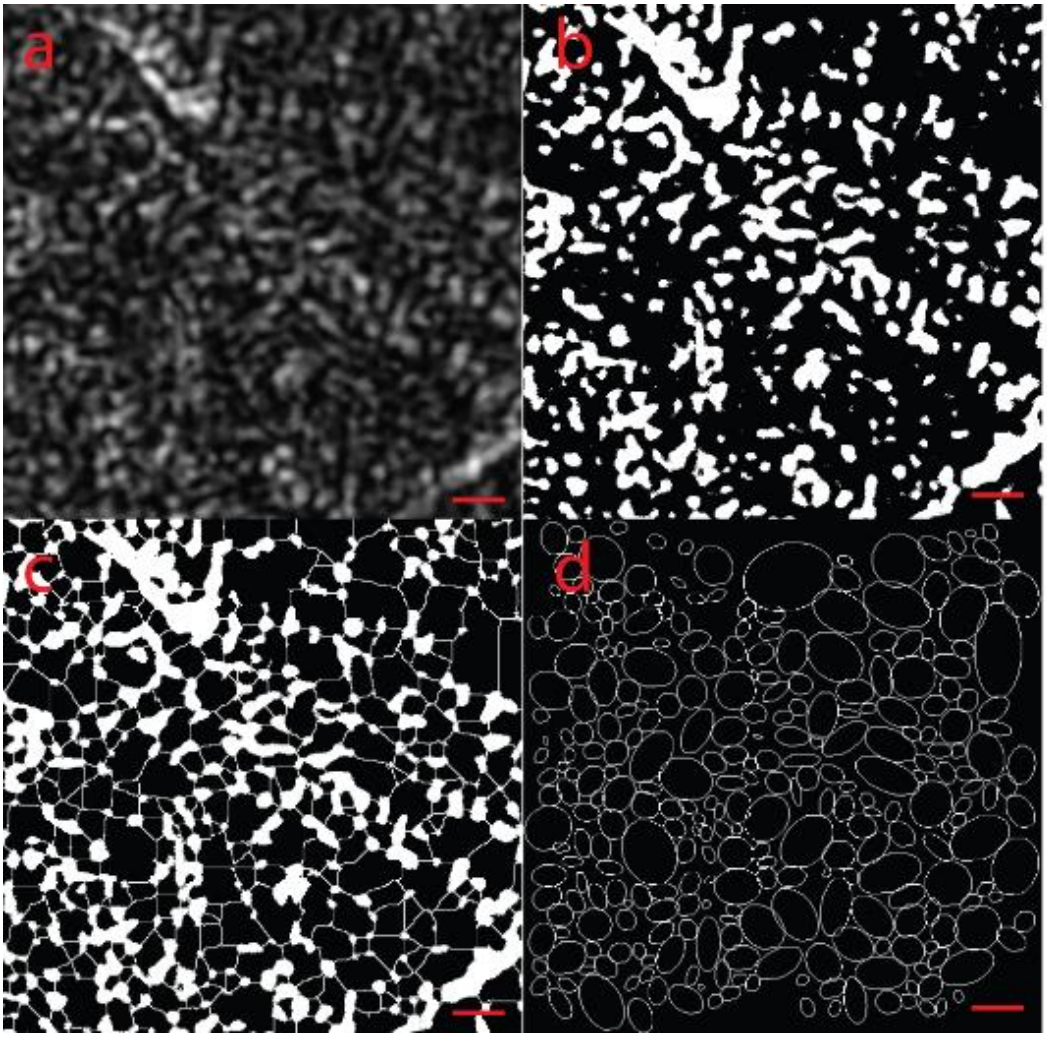


Figure 3.23: Collagen pore size distribution. (a) Example confocal reflection micrograph of collagen I hydrogel. (b) Image in (a) after thresholding and binarization. (c) Image in (b) after Watershed segmentation. (d) Elliptical particle analysis of image in (c). Scale bars: 1 μm.

	Pore Size [μm] (Mean ± std.)	Pore Area [μm^2] (Mean ± std.)	Areal Porosity [%] (Mean ± std.)
Fixed, MDA untreated	0.547 ± 0.277	0.280 ± 0.338	67 ± 7
Fixed, MDA 10 μM Y	0.537 ± 0.296	0.280 ± 0.378	68 ± 12
Fixed, No cells	0.532 ± 0.280	0.268 ± 0.337	68 ± 10
Unfixed, No cells	0.588 ± 0.324	0.336 ± 0.441	72 ± 9

Table 3.5: Collagen Pore Size, Pore Area, and Areal Porosity.

Quantitative elastic modulus determination of heterogeneous materials.

To determine the apparent Young's modulus from indentations, an elastic contact model for a spheroconical tip is used[182]. The geometry of the tip in this model is a sphere with radius R that transitions smoothly and continuously (at transition radius $b = r\cos\theta$) to an axisymmetric cone with semi-vertical angle θ at the (Figure 2.4, Eqs. 17, 18)[183]. In order to separate out the contribution to the force response from the underlying collagen layer, the spheroconical model is used in conjunction with a two-layer model developed by Dhaliwal and Rau, who presented a generalized analytical solution to the indentation problem of two bonded layers in the form of a Fredholm Integral Equation of the Second Kind[186]. The equations are solved in MATLAB numerically using the Nyström method[234].

MDA-MB-231 cells stiffen as they invade collagen I matrices.

MDA-MB-231 breast cancer cells were seeded on top of fully polymerized collagen I matrices. After 24-72 hours, the cells began to invade into the collagen matrices. As exemplified by the confocal micrographs and elasticity tomograms in Figure 3.24, more deeply embedded cells exhibited significant stiffening. To correctly quantify this effect, force-indentation curves on pericellular collagen were fitted to

approximate the Young's modulus of the collagen underneath the cell (i.e. the substrate). The cell height and substrate Young's modulus were then used to determine the cell's substrate-corrected Young's modulus from force-indentation curves on the cell.

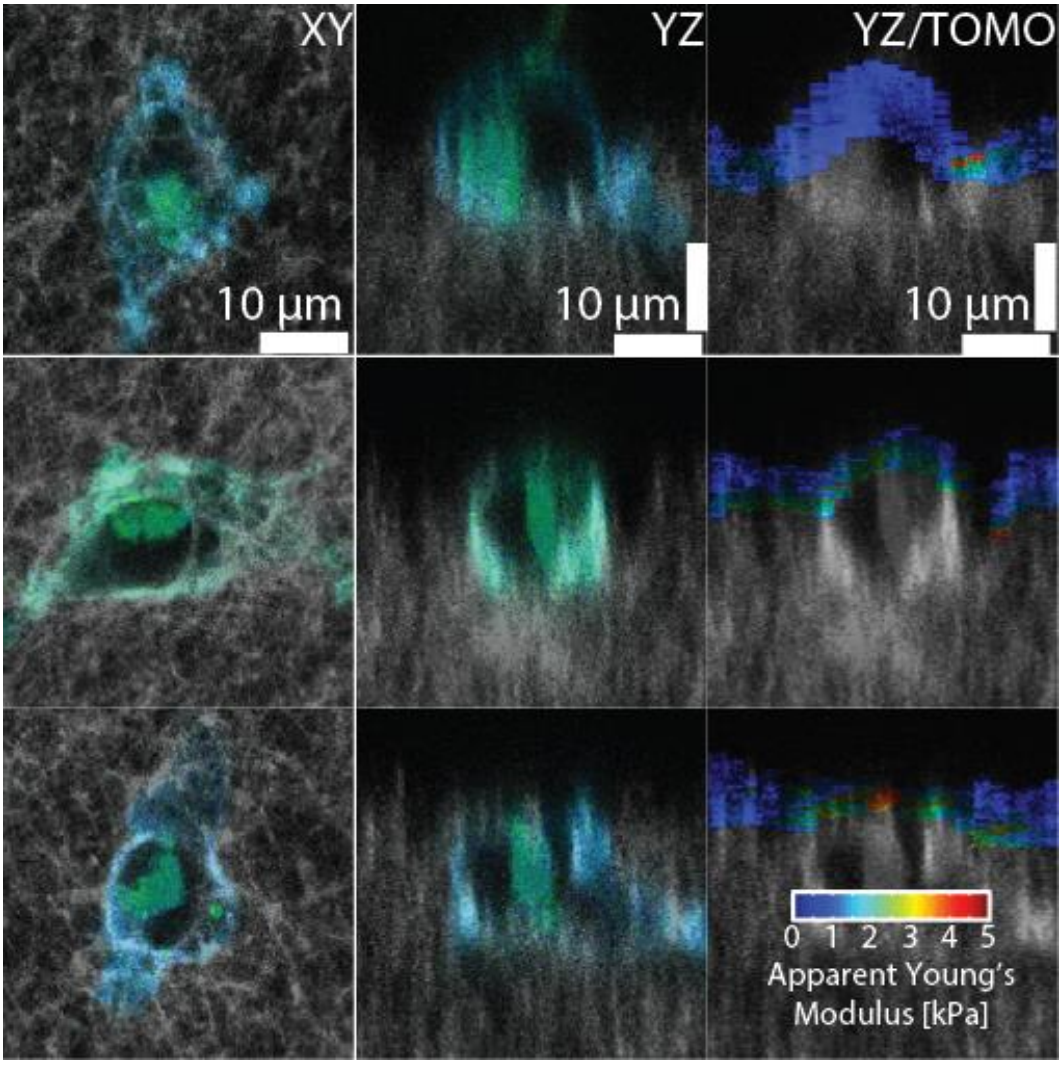


Figure 3.24: Confocal fluorescence lifetime images with superposed elasticity tomograms. The more embedded cell (bottom row) has a peak modulus of ~5 kPa, typical of the observed invasion-associated cell stiffening.

To quantify a cell's embeddedness, the normalized cell protrusion height (NCPH) is defined as the height difference between the collagen and top cell surfaces (determined from the contact points of the force-indentation curves) divided by the cell height (Figure 3.25A).

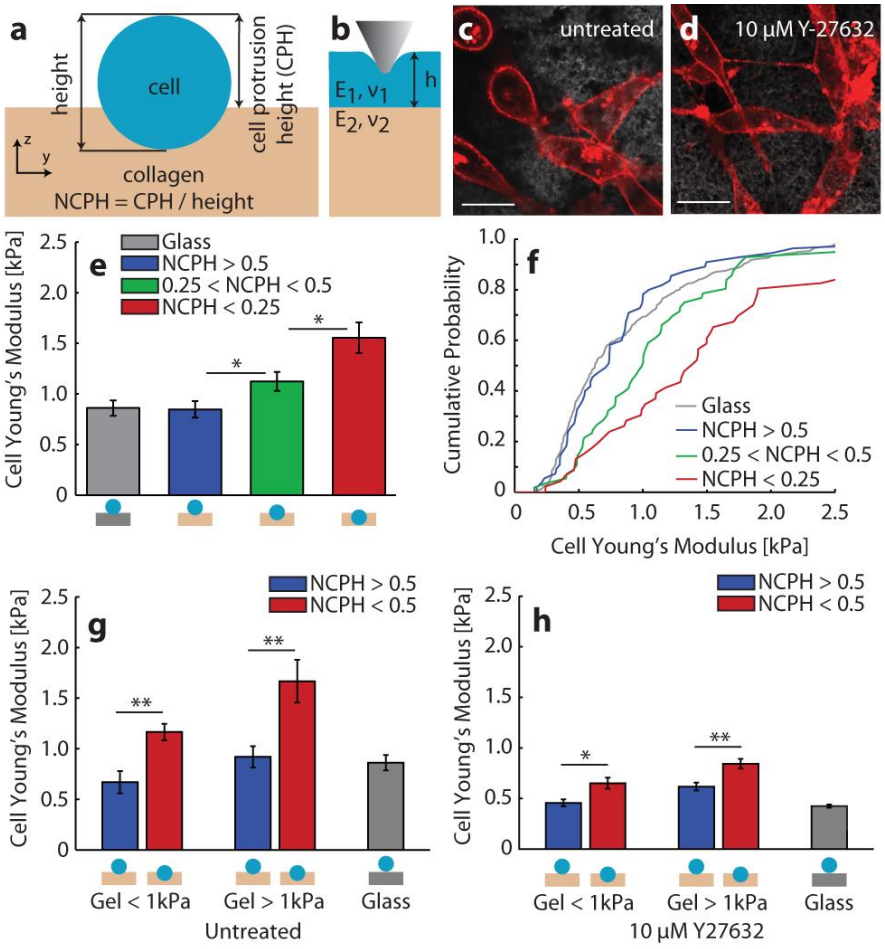


Figure 3.25: Young's moduli of MDA-MB-231 cells on glass and partially embedded in collagen I hydrogels. (A) Schematic defining the normalized cell protrusion height (NCPH) quantifying the degree of cell embedding., (B) Bar chart (mean ± s.e.m) and (C) cumulative probability of Young's moduli of cells on glass and cells partially embedded in collagen, binned according to NCPH (from left to right: n = 64, n = 55, n = 56, and n = 46). (D) Schematic of the axisymmetric finite element simulations of a partially embedded cell in collagen using ANSYS. The element lengths used in the mesh for the finite element simulations is 50 nm for the tip and 500 nm for the cell. The tip is spheroconical with r=750 nm and θ=22.5°, the cell is modeled as a sphere with 7 μm radius embedded in a half-space. (E) Bar graphs showing the apparent Young's modulus for different gel elasticity and NCPH determined by fitting the simulated force-indentation results. In all combinations of collagen cell stiffnesses tested, the increase in apparent Young's modulus from NCPH=0.64 to NCPH=0.07 is 9%, which is less than experimentally observed. Young's moduli are determined by fitting the indentation from 0.25−2.5 μm and corrected to account for the influence of the collagen substrate. * denotes $p < 0.05$ from independent two-tailed, two-sample Student's *t*-tests for equal means and equal but unknown variances with $a = 0.05$.

Figure 3.25E,F show the Young's moduli of partially embedded cells as a function of embeddedness, binned into three nearly equally populated groups. Cells 0−50% embedded (NCPH > 0.5) had Young's moduli of 847 ± 82 Pa (mean ± s.e.m.), similar to the observed moduli of cells on glass ($p = 0.88$). Cells 50−75% embedded (0.25 < NCPH < 0.5) had Young's moduli of 1124 ± 94 Pa, significantly stiffer (33%, $p = 0.028$) than cells 0−50% embedded. Cells 75−100% embedded (NCPH < 0.25) had Young's moduli of 1554 ± 152 Pa, significantly stiffer again (38%, $p = 0.014$) than cells 50−75% embedded.

Invasion-associated stiffening is enhanced on stiffer matrices.

In addition to binning the cells as a function of their degree of invasion, the cell stiffness was binned according to the stiffness of the underlying collagen matrix, without taking into account the cells' degree of embeddedness. No significant dependence of cell stiffness on collagen stiffness was observed (Figure 3.26). This is complementary to previous findings that MDA-MB-231 cells have reduced

mechanosensitivity to substrate stiffness; unlike MCF-10A cells, their proliferation and morphology was not affected by changes in subtrate stiffness[22].

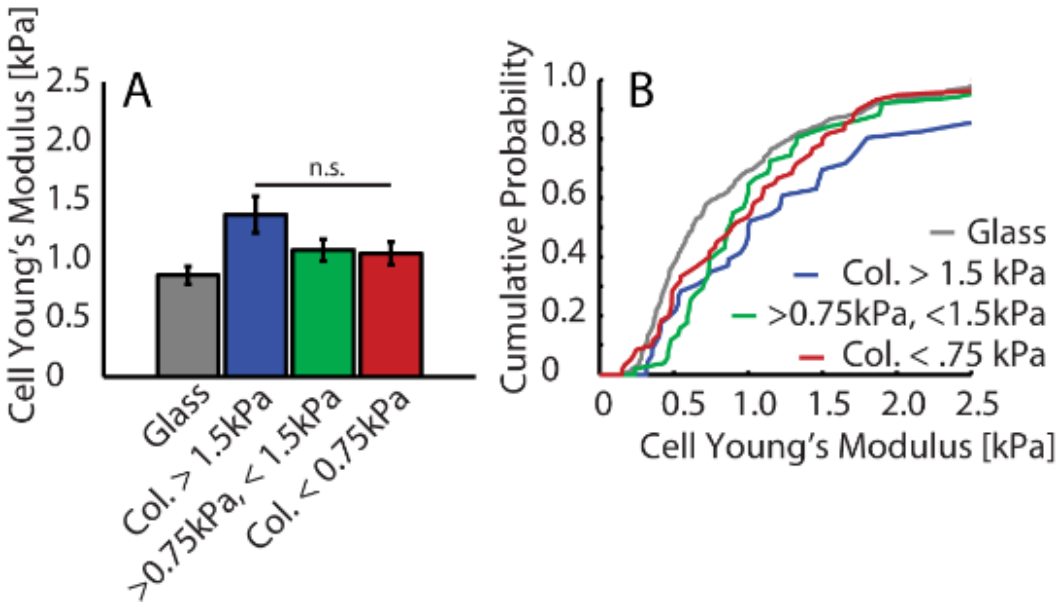


Figure 3.26: (A) Bar chart (mean ± s.e.m) and (B) cumulative probability of Young's moduli of cells on glass and cells partially embedded in collagen, binned according to underlying collagen stiffness. n.s. denotes $p > 0.05$ from independent two-tailed, two-sample Student's *t*-tests for equal means and equal but unknown variances with $a = 0.05$.

The data was then binned by both embeddedness and collagen stiffness (Figure 3.25G). On soft collagen ($E_{col.} < 1$ kPa), cells 50−100% embedded (NCPH < 0.5) were significantly stiffer (74%, $p = 0.0067$) than cells 0−50% embedded (NCPH > 0.5). On stiff collagen ($E_{col.} > 1$ kPa), cells 50−100% embedded were 81% stiffer ($p = 0.0012$) than cells 0−50% embedded. Conversely, the stiffness of 0−50% embedded cells on soft and stiff collagen did not differ significantly ($p = 0.165$), whereas 50−100% embedded cells on stiff collagen were 43% stiffer than those on

soft collagen (p = 0.008). The observed correlation between cell stiffness and embeddedness is thus more pronounced on stiffer collagen.

Invasion-associated stiffening is Rho/ROCK-dependent.

Because the least-embedded cells had Young's moduli similar to those measured on glass, and the stiffest cells were those invading the stiffer collagen regions, it was hypothesized that more invasive cells are stiffer due to enhanced actomyosin contractility, which is associated with decreased F-actin depolymerization and increased actin fiber bundling—both factors which would cause increased cytoskeletal rigidity. Additionally, invasion of MDA-MB-231 cells in collagen and Matrigel® has been shown to depend on the Rho/ROCK pathway, which regulates actomyosin contractility and amoeboid motility[235,69,236,237].

Measurements were then repeated on cells in presence of 10 μM Y-27632 ROCK inhibitor. Treated cells adopted a characteristic spindle-like morphology (Figure 3.25 C,D). Compared to untreated cells, ROCK inhibition significantly reduced Young's moduli of cells on glass (51%, p = 2.39 E-7); cells embedded 0-50% on soft collagen (32%, p = 0.073) and stiff collagen (33%, p = 0.003); and cells embedded 50-100% on soft collagen (44%, p = 6.33 E-5) and stiff collagen (49%, p = 0.004) (Fig. 29H, Table 3.6). ROCK inhibition also diminished the increase in cell stiffness observed with increasing embeddedness. On soft collagen, 50−100% embedded cells were only 42% stiffer (c.f. 74%) than 0−50% embedded cells (p = 0.024), and on stiff collagen, 50−100% embedded cells were only 37% (c.f. 81%) stiffer than 0−50% embedded cells (p = 0.002). Additionally, 50−100% embedded cells on stiff collagen were only 30% stiffer (c.f. 43%) than those on soft collagen (p = 0.022). This

confirms that ROCK-mediated contractility plays a significant role in the substrate-stiffness-dependent invasion-associated cell stiffening observed.

	Substrate	NCPH	Number of cells	Young's Modulus of the cell [Pa]	
				(mean ± s.e.m.)	(median)
Untreated	Glass	= 1	64	861 ± 76	627
	Col E < 1 kPa	> 0.5	16	669 ± 109	663
	Col E > 1 kPa	> 0.5	39	920 ± 105	739
	Col E < 1 kPa	< 0.5	71	1165 ± 81	1092
	Col E > 1 kPa	< 0.5	31	1667 ± 211	1231
	All	Fully Embedded	10	1400 ± 200	1500
+ 10 μM Y27632	Glass	= 1	64	425 ± 15	362
	Col E < 1 kPa	> 0.5	16	457 ± 34	451
	Col E > 1 kPa	> 0.5	55	618 ± 39	563
	Col E < 1 kPa	< 0.5	34	651 ± 55	585
	Col E > 1 kPa	< 0.5	19	844 ± 48	832

Table 3.6: Young's Moduli of MDA-MB-231 Cells Partially Embedded in Collagen I Matrices, by Pericellular Collagen Stiffness and Degree of Embedding, with and without ROCK Inhibition.

To address the possibility that the stiffening was due merely to the support from the surrounding matrix, we conducted finite element simulations of indentations on models of a cell (E = 1.5 kPa) embedded to varying degrees in two materials ($E_{col.}$ = 1.5 kPa or $E_{col.}$ = 0.75 kPa) (Figure 3.27). Simulated force curves were generated and fitted to find the Young's moduli, which vary with the cell's embeddedness by ≤ 9%, much less than in the experiments, and well within the range of cantilever calibration errors. Therefore, the cells become stiffer with increased embeddedness, a clear example of change in phenotype in response to changes in the 3D environment.

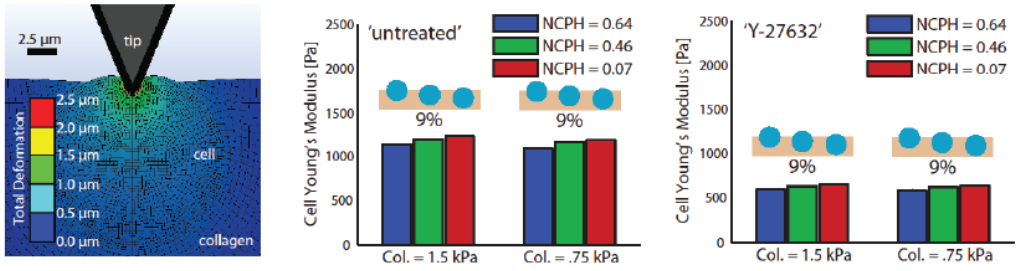


Figure 3.27: Finite element simulations of partially embedded spheres using ANSYS to simulate cells that are partially invaded into a collagen I matrix. For the simulations, the radius of the sphero-conical tip is 750nm with half-angle of $\pi/8$, the radius of the cell is 7µm, the mesh of the tip is 50nm, the mesh of the cell is 300nm, and force of indentation is calculated every 2nm. The Young's modulus for the untreated cell is taken to be 1.5kPa, and the Young's modulus for the cell treated with Y-27632 is taken to be 0.75kPa. The bar graph shows the calculated Young's modulus from 0.25-2.50µm simulated indentations which has been corrected for the collagen influence with the two-layer theory. When the cell is nearly fully embedded (NCPH=0.07), the apparent Young's modulus is only 9% stiffer than the case where it is much less embedded (NCPH=0.64) for all cell and collagen Young's moduli. For the case of the cell not being embedded at all (NCPH ~ 0.0), the cell and collagen will have an extremely small contact area resulting in a very low apparent Young's modulus because the cell will be mostly unsupported on the bottom edge, however this is not considered (a hemisphere would be more appropriate than a sphere for this case).

Fully embedded cells exhibit similar invasion-associated stiffening.

Figure 3.28 shows collagen remodelling and cell protrusions in different optical sections under the collagen surface, along with the apparent stiffness at indentation depths corresponding to those sections.

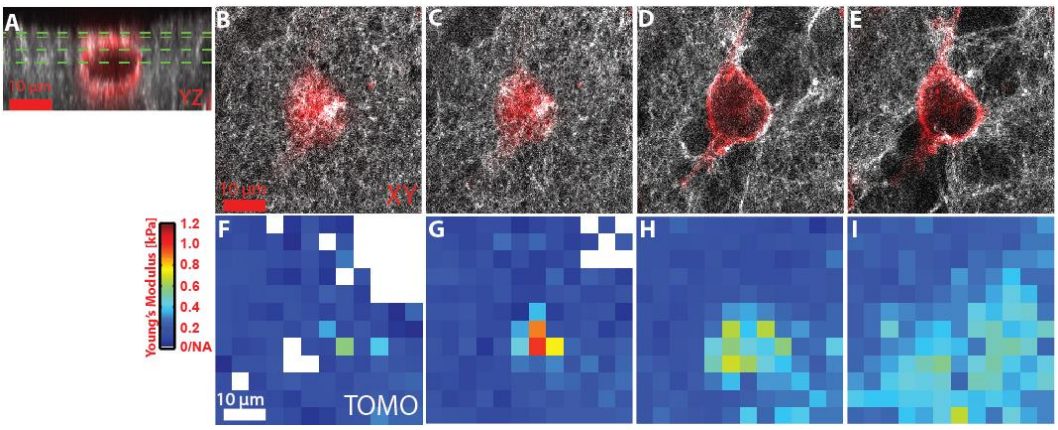


Figure 3.28: MDA-MB-231 cell fully embedded in collagen I matrix. (A) Axial confocal fluorescence micrograph. Dashed lines correspond (from top to bottom) to lateral planes shown in (B,F), (C,G), (D,H), (E,I). (B,D,F,H) show the lateral confocal micrographs, detailing the collagen remodelling and cellular protrusions. (F,G,H,I) show the elasticity tomograms indicating the apparent Young's modulus at the corresponding depths.

To determine the Young's moduli of cells that were fully embedded in collagen, simulations of indentations were performed using finite element models with geometry determined from the axial confocal micrographs. Each cell's position and Young's modulus were iteratively adjusted in the simulation until the simulated force-indentation curve resulted in an apparent Young's modulus that differed minimally from the apparent Young's modulus fitted from the experimental force-indentation curve, as illustrated in Figure 3.29D-G.

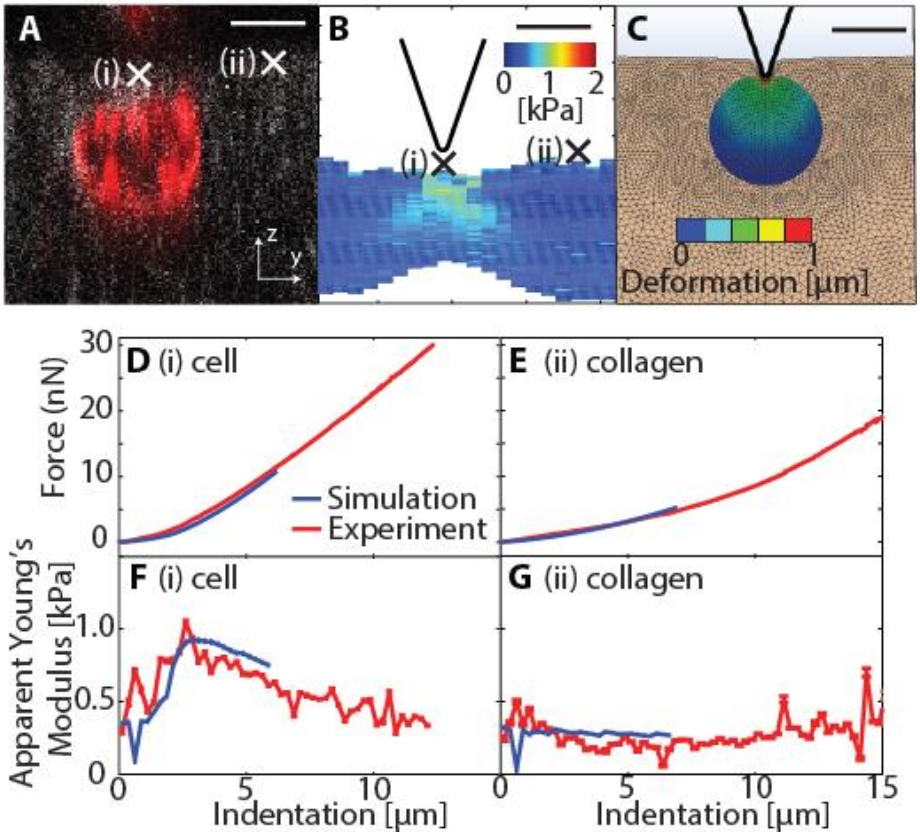


Figure 3.29: Determining the Young's modulus of a fully embedded cell by finite element simulation. (A) Axial confocal fluorescence micrograph. (B) AFM elasticity tomogram showing the apparent Young's modulus as a function of depth. (C) Finite element model corresponding to the sample. (D,E) Indentation force-depth curves taken over points above the cell (i) and gel (ii) in experiment (red) and in simulation (blue). (F,G) Apparent Young's modulus determined from the curves in (D,E) by piecewise fitting with the spheroconical model.

While many fully embedded cells were measured experimentally (n = 64), only those at invasion depths ≤ 3.5 µm could be quantified with this method despite the AFM probe reaching the depth of the cell, since more deeply embedded cells have lower mechanical contrast (Figure 3.29).

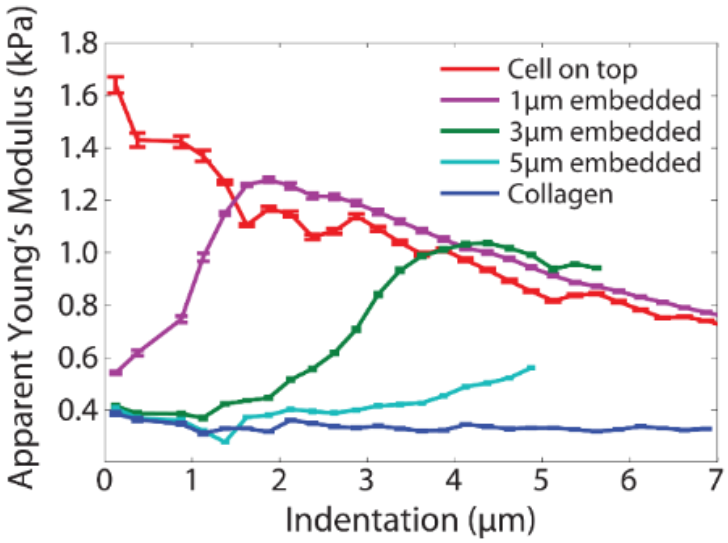


Figure 3.30: Plot of the depth-dependent Young's modulus of fully embedded cells at various depths from finite element analysis simulations. The parameters used are a sphero-conical tip with apex radius 745 nm and half-angle 18.81°, the cell Young's modulus is 2.0 kPa and collagen Young's modulus is 0.3 kPa (both with Poisson ratio 0.45), and the radius of the cell is 6.5 μm. As the cell moves from sitting on top of the collagen gel with a protrusion of 1 μm (red) to being 5 μm embedded (teal), both the highest observed value of the Young's modulus and the rate at which the signal transitions from collagen to cell decrease. Thus, the mechanical contrast decreases as the cell becomes further embedded in the collagen, so the analysis of the fully embedded cells must be limited to cells that have not invaded too deeply.

13 cells were analyzed with this approach; with 3 stiff outliers omitted, the Young's modulus was 1.4 ± 0.2 kPa (mean ± s.e.m.) with median 1.5 kPa (Table 3.6, Figure 3.31). This is ~65% stiffer than non-embedded cells and consistent with the statistically robust trend observed among partially embedded cells.

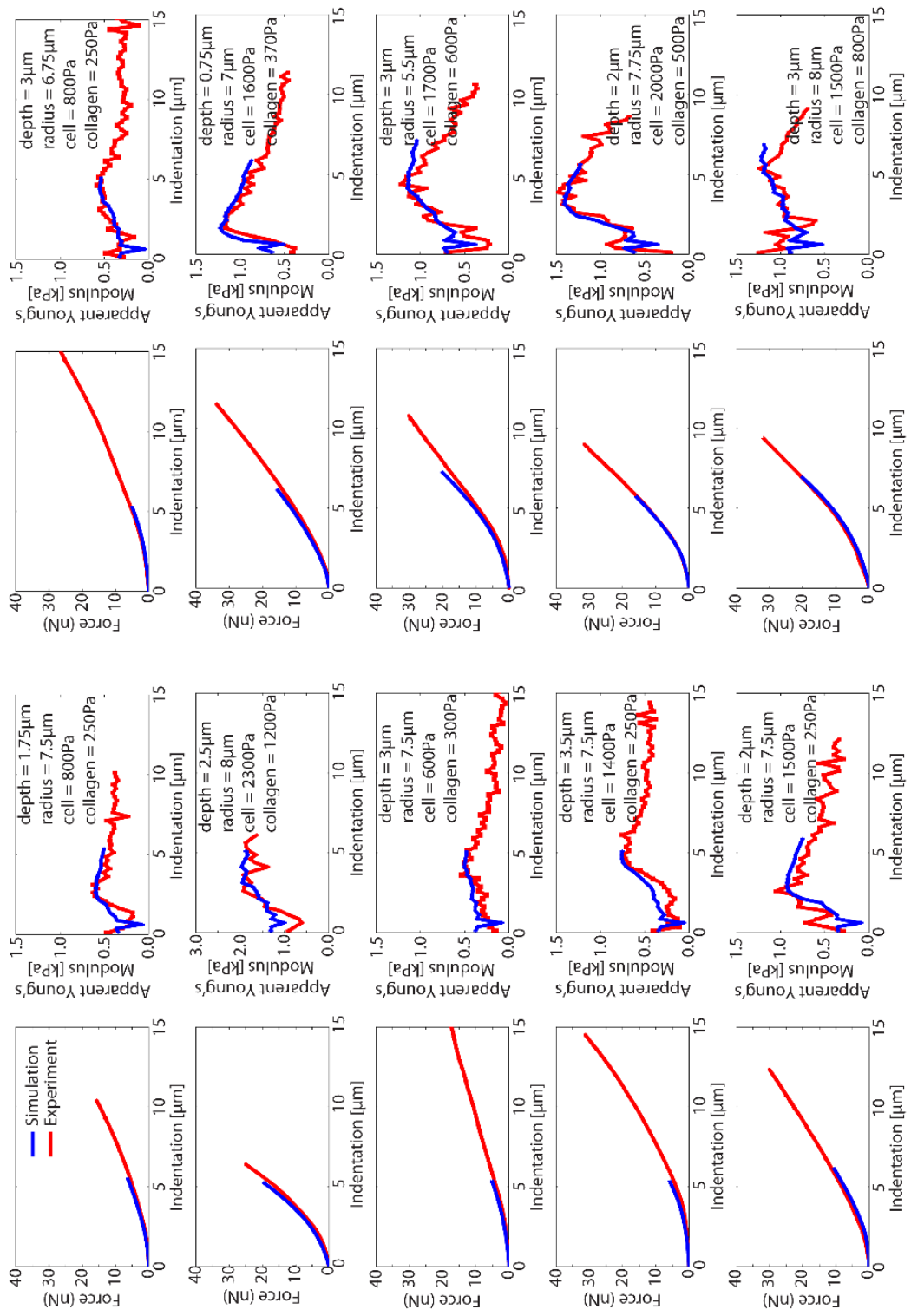

Simulation
Experiment
Force (nN)
Indentation [µm]
Apparent Young's Modulus [kPa]
depth = 1.75µm
radius = 7.5µm
cell = 800Pa
collagen = 250Pa
depth = 2.5µm
radius = 8µm
cell = 2300Pa
collagen = 1200Pa
depth = 3µm
radius = 7.5µm
cell = 600Pa
collagen = 300Pa
depth = 3.5µm
radius = 7.5µm
cell = 1400Pa
collagen = 250Pa
depth = 2µm
radius = 7.5µm
cell = 1500Pa
collagen = 250Pa
depth = 3µm
radius = 6.75µm
cell = 800Pa
collagen = 250Pa
depth = 0.75µm
radius = 7µm
cell = 1600Pa
collagen = 370Pa
depth = 3µm
radius = 5.5µm
cell = 1700Pa
collagen = 600Pa
depth = 2µm
radius = 7.75µm
cell = 2000Pa
collagen = 500Pa
depth = 3µm
radius = 8µm
cell = 1500Pa
collagen = 800Pa

Figure 3.31: Ten fully embedded cells with the experimental force-indentation curves and depth-dependent fits (red) overlayed with the finite element simulation results (blue) from ANSYS. For each cell, the physical dimensions and elasticity parameters of the sample are given. The tip is modeled to be sphero-conical with the same dimensions as used in the experiment. The mesh of the cell and collagen is triangular with element length of 500 nm for a radial distance of 20 μm from the top and center of the collagen, and then tapers to 1μm. The simulation is axisymmetric, and the collagen has a depth and radius of 100 μm. The mesh of the tip is triangular with element length of 50 nm. The contact point of the force-indentation data is determined manually for each of these examples. The bin size for the depth-dependent fits are 250 nm.

3.6.4 Conclusions

In §3.6, an approach combining AFM, confocal microscopy, and simulation was demonstrated that allows for the extraction of quantitative data from indentations on submerged objects. Despite the cells' being embedded in ECM, the force responses of the cell and ECM have been successfully decoupled to achieve single cell force resolution in a 3D microenvironment. MDA-MB-231 cells were found to stiffen as they invade into collagen I matrices, and evidence was provided that this stiffening is due to Rho/ROCK-dependent actomyosin contractility. This novel observation illustrates the importance of the 3D microenvironment to understanding the mechanics and behavior of cells in their physiological context. Poincloux *et al.* reported the formation of F-actin rich uropod-like structures at the cell rear of MDA-MB-231 cells during rounded-cell vertical migration into 3D ECM (requiring RhoA-ROCK-myosin II-mediated contractility) [237]; the results here corroborate the rounded-cell invasion model. The methods presented enhance the potential of AFM for use in cell mechanics assays to identify cells' response to specific treatment or growth conditions while cultured in ECM-like materials.

3.6.5 Materials and Methods

Collagen preparation

Bovine collagen I (Nutragen, Advanced Biomatrix) gels were attached to glass surfaces using a procedure similar to Pelham and Wang[238]. Glass-bottom dishes were ultrasonicated in ethanol for 10 min, then ultrasonicated in ultrapure water for 10 min. Dishes were blown dry with N_2 gas, plasma cleaned in O_2 gas for 5 min, incubated in 1% (3-Aminopropyl)triethoxysilane in ethanol for 30 min, then washed with ethanol and ultrapure water. Surfaces were then incubated in 0.5% glutaraldehyde in 1× DPBS for 1 h, washed with ultrapure water, then allowed to dry vertically. Purified bovine collagen I (6.1 $mg \cdot ml^{-1}$) was mixed on ice with 10× DPBS, 0.1 M NaOH, and ultrapure water at a ratio of 32:4:3:1 to form a 4.88 $mg \cdot ml^{-1}$ gel. The collagen was diluted with ultrapure water and the amount of NaOH was linearly decreased to form gels at lower concentrations. 200 μL was pipetted onto functionalized dishes and spread with the pipette tip. Dishes were then incubated 1.5 h at 37 °C, 5% CO_2, after which the gels were gently covered with 37 °C 1× Dulbecco's phosphate buffered saline (DPBS). Collagen was stained with 0.02 $mg \cdot ml^{-1}$ Atto 465 NHS, which was suspended at 2 $mg \cdot ml^{-1}$ in dimethyl sulfoxide (DMSO).

Cell Culture

MDA-MB-231 metastatic breast cancer cells from ATCC were cultured at 37 °C and 5% CO_2 in 1× Dulbecco's Modified Eagle Medium containing 4.5 $mg \cdot ml^{-1}$ D-glucose and L-glutamine supplemented with 10% Fetal Bovine Serum. Cells were cultured as in[22] using Cellstripper™ in place of trypsin. For experiments with inhibitors, growth medium was supplemented with 10 μM Y-27632 at the time the cells were seeded on

the dishes. Cells were seeded on top of polymerized collagen gels or glass-bottom dishes 6−96 hours prior to measurements in growth medium for use in experiments. Cell membranes were stained using 2.5 $\mu g \cdot ml^{-1}$ CellMask™ Deep Red Plasma membrane stain, which was suspended at 1 $mg \cdot ml^{-1}$ in DMSO. Cell measurements and staining were performed at 37 °C in 1× Hank's Balanced Salt Solution (HBSS) containing calcium and magnesium. For experiments with inhibitors, HBSS was supplemented with 10 μM Y-27632.

Atomic force microscopy and confocal fluorescence microscopy.

The AFM and confocal fluorescence measurements were performed on a combined system consisting of an Asylum Research MFP-3D-BIO AFM and a Picoquant Microtime 200 confocal laser scanning microscope[21,191]. Team NanoTec LRCH-750 AFM probes were used. Spring constants were determined using the thermal energy dissipation method (typically ~0.15 $N \cdot m^{-1}$)[164,165]. The AFM tip was aligned in the confocal volume and confocal fluorescence images were scanned in lateral and axial planes. Data collected for elasticity nanotomograms was recorded by taking a line measurement of 40 μm with 20 force-indentation measurements in the axial plane, normal to the cantilever (one indentation per 2 μm) with 2 $\mu m \cdot s^{-1}$ approach and retraction speeds and a variable trigger force (typically 15−35 nN). For cells plated on glass, each cell is indented 4 times in force-volume mode over a 4 μm^2 area in the central nuclear region.

Finite element analysis

Finite element analysis was performed using ANSYS Workbench 14.0. The models were axially symmetric around the center of the tip and cell to increase computational efficiency. The collagen was modeled as an Ogden 1st order solid (α_1 =

2, identical to Neo-Hookean solid) with height and radius of 100 μm with a fixed support on the bottom boundary. The cell was modeled as a spherical inclusion bonded to the collagen with a different Young's modulus but otherwise similar material properties. The AFM tip was modeled as a spheroconical tip with dimensions similar to those used in the experiment and Young's modulus on the order of GPa. The tip had a triangular mesh size of 50 nm and the contact between the tip and sample was assumed to be frictionless. The cell and collagen mesh had an element length of 500 nm within 20 μm from the tip, which then tapered up to 1 μm. All elements had midside nodes. Indentations between 4 μm and 7 μm were performed in 5 nm incremental steps depending on when the simulation failed to converge due to numerical instability occurring from large deformations. The Poisson ratios of the cell and the collagen were set to 0.45.

Data analysis

Data analysis was performed with home-built routines in MATLAB. AFM force-indentation curve analysis with the sphero-conical contact model and analytical two-layer correction are described in full details in SI text. Cells and collagen were assumed to be incompressible ($\nu_{cell} = \nu_{col.} = 0.5$). All reported *p*-values between compared populations come from independent two-tailed, two-sample Student's *t*-tests at the 5% significance level for populations with equal means and equal but unknown variances.

To determine the Young's modulus partially embedded cells, confocal images and elasticity nanotomograms were recorded. The spheroconical tip and the two-layer correction are used to analyze the raw data. For each measured cell, 3−6 force-

indentation curves on pericellular collagen (4−12 μm from the cell, 3 on each side if available) are fitted in the 0.25-2.5 μm range using the sphero-conical contact model to find the collagen Young's modulus E_2. The cell height h is estimated from the axial confocal fluorescence micrograph recorded before the indentations. A set of 3−4 experimental force-indentation curves from the highest part of the cell's apical surface are recorded and averaged. The cell Young's modulus E is approximated using the minimization method using E_2 and h on the 0.25-2.5 μm indentation interval. To determine the Young's modulus of cells on glass, the data is fit with the sphero-conical tip geometry on the 0.25-2.5 μm indentation interval and the results for each cell are averaged over 4 curves. To determine the Young's modulus fully embedded cells, confocal images and elasticity nanotomograms were recorded as described in the atomic force microscopy and confocal fluorescence microscopy methods. One experimental force-indentation curve over the highest part of the cell's nuclear region is used to represent the cell, and fitted piecewise to the sphero-conical model in 250 nm intervals to find the depth-dependent apparent Young's modulus. For the finite element models, the invasion depth of the cell is estimated from the axial confocal micrograph, and the Young's modulus of the collagen is determined from force-indentation data. The cell's Young's modulus is initially guessed, and an indentation by a rigid (~1 GPa) probe with geometry similar to that of the experimentally used AFM probe is then produced using ANSYS, yielding a simulated force-indentation curve. The simulated curve is fitted piecewise with the spheroconical model in 250 nm intervals to find the depth-dependent apparent Young's modulus, which is then compared to that resulting from the experimental

force-indentation curve. Simulations are repeated in subsequent models in which the depth of the cell is adjusted in 0.25 μm increments, and the Young's modulus of the cell is adjusted in 0.1 kPa increments, until the experimental and simulated depth-dependent apparent Young's moduli differ minimally.

12. OUTLOOK

There are several different directions that could be taken to advance the investigation of cell mechanics using the methods used and developed in this thesis. Among the most immediate are the application of AFM-based dynamic mechanical analysis to 3D heterogeneous samples such as those studied in §3.6. By oscillating the probe, the phase lag between drive and response can be used to find the frequency-dependent storage and loss moduli. Extending such studies into the frequency domain would be extremely useful in itself. Furthermore, propagation of mechanical waves through the sample may enable characterization of more deeply embedded cells. Also, cells may be more accurately distinguished from their surroundings with the additional information about the sample. Cytoskeletal drugs, like the ROCK inhibitor used in §3.6, or myosin inhibitors, and drugs that modify actin polymerization, cholesterol, microtubule dynamics, and intermediate filaments can all be employed straightforwardly to further investigate the relative contributions of various cytoskeletal components to the measured mechanical properties. Even the introduction of growth factors and pre-conditioned media are likely to reveal interesting changes in mechanics during migration. Cells with fluorescent proteins conjugated to cytoskeletal proteins of interest could also be studied (e.g. to compare cell stiffness in regions with actin fibers to regions with branched actin filament networks). Cells could also be studied in matrices with different composition or densities, aligned fibers, or in micropattered environments. With environmental control, time-lapse studies could be conducted to investigate mechanics during

migration in more detail. AFM could also be combined with other mechanical methods, e.g. particle tracking inside the cell.

In 1924, Seifriz wrote in the discussion of results obtained with his new apparatus for the mechanical measurements on cells and other soft biomaterials:

> "The stretching value of 9 μ[m] obtained is, in itself, of little significance as a value. Only by comparison with some standard will such a value mean anything. Unfortunately there is no accepted standard among colloidal jellies. The elastic properties of jellies have received little attention. Comparisons of elastic values of protoplasm with those of known concentrations of, for example, gelatin, would give a basis for standardization"[239].

Sadly, 90 years later the situation remains much the same. The broader cell mechanics field would benefit greatly from an accepted standard reference material with which to compare measurements on cells.

REFERENCES

1. Schrodinger, E. *What is life? the physical aspect of the living cell ; with Mind and matter ; & Autobiographical sketches*. (Cambridge University Press, 1992). at <http://search.ebscohost.com/login.aspx?direct=true&scope=site&db=nlebk&db=nlabk&AN=53597>

2. WATSON, J. D. & CRICK, F. H. D. Molecular Structure of Nucleic Acids: A Structure for Deoxyribose Nucleic Acid. *Nat.* **171,** 737–738 (1953).

3. Austin, R. H. & Gerstman, B. S. Preface: Physics of Cancer. *AIP Adv.* **2,** 010901 (2012).

4. Paszek, M. J. *et al.* Tensional homeostasis and the malignant phenotype. *Cancer Cell* **8,** 241–54 (2005).

5. Fraley, S. I. *et al.* A distinctive role for focal adhesion proteins in three-dimensional cell motility. *Nat. Cell Biol.* **12,** 598–604 (2010).

6. Kasas, S. *et al.* Superficial and deep changes of cellular mechanical properties following cytoskeleton disassembly. *Cell Motil. Cytoskeleton* **62,** 124–32 (2005).

7. Huang, S. & Ingber, D. E. Cell tension, matrix mechanics, and cancer development. *Cancer Cell* **8,** 175–6 (2005).

8. Cross, S. E. *et al.* AFM-based analysis of human metastatic cancer cells. *Nanotechnology* **19,** 384003 (2008).

9. Cross, S. E., Jin, Y.-S., Rao, J. & Gimzewski, J. K. Nanomechanical analysis of cells from cancer patients. *Nat. Nanotechnol.* **2,** 780–3 (2007).

10. Li, Q. S., Lee, G. Y. H., Ong, C. N. & Lim, C. T. AFM indentation study of breast cancer cells. *Biochem. Biophys. Res. Commun.* **374,** 609–13 (2008).

11. Lekka, M. *et al.* Elasticity of normal and cancerous human bladder cells studied by scanning force microscopy. *Eur. Biophys. J.* **28,** 312–6 (1999).

12. Lekka, M. *et al.* Local elastic properties of cells studied by SFM. *Appl. Surf. Sci.* **141,** 345–349 (1999).

13. Guck, J. *et al.* Optical deformability as an inherent cell marker for testing malignant transformation and metastatic competence. *Biophys. J.* **88,** 3689–98 (2005).

14. Lee, M.-H. *et al.* Mismatch in Mechanical and Adhesive Properties Induces Pulsating Cancer Cell Migration in Epithelial Monolayer. *Biophys. J.* **102,** 2731–2741 (2012).

15. Rosenbluth, M. J., Lam, W. a & Fletcher, D. a. Force microscopy of nonadherent cells: a comparison of leukemia cell deformability. *Biophys. J.* **90,** 2994–3003 (2006).

16. Yao, W., Gu, L., Sun, D., Ka, W. & Wen, Z. Wild Type p53 Gene Causes Reorganization of Cytoskeleton and , Therefore , the Impaired Deformability and Difficult Migration of Murine Erythroleukemia Cells. *Cell Motil. Cytoskeleton* **56,** 1–12 (2003).

17. Ochalek, T., Nordt, F. J., Tullberg, K., Variants, M. C. & Burger, M. M. Correlation between Cell Deformability and Metastatic Potential in B16-F1 Melanoma Cell Variants Correlation between Cell Deformability and Metastatic Potential in B16-F1. *Cancer Res.* **48,** 5124–5128 (1988).

18. Ward, K. A., Wen-I, L., Zimmer, S. & Davis, T. Viscoelastic properties of transformed cells : role in tumor cell progression and metastasis formation. *Biorheology* **28,** 301–313 (1991).

19. Park, S., Koch, D., Cardenas, R., Käs, J. & Shih, C. K. Cell motility and local viscoelasticity of fibroblasts. *Biophys. J.* **89,** 4330–42 (2005).

20. Suresh, S. Biomechanics and biophysics of cancer cells. *Acta Biomater.* **3,** 413–38 (2007).

21. Fuhrmann, A. *et al.* AFM stiffness nanotomography of normal, metaplastic and dysplastic human esophageal cells. *Phys. Biol.* **8,** 015007 (2011).

22. The Physical Sciences Oncology - Centers Network. A physical sciences network characterization of non-tumorigenic and metastatic cells. *Sci. Rep.* **3,** 1–12 (2013).

23. Davies, P. C. W. & Lineweaver, C. H. Cancer tumors as Metazoa 1.0: tapping genes of ancient ancestors. *Phys. Biol.* **8,** 1–10 (2011).

24. Hanahan, Douglas, Weinberg, R. A. The Hallmarks of Cancer. *Cell* **100,** 57–70 (2000).

25. Hanahan, D. & Weinberg, R. a. Hallmarks of cancer: the next generation. *Cell* **144,** 646–74 (2011).

26. Tlsty, T. D. & Coussens, L. M. Tumor stroma and regulation of cancer development. *Annu. Rev. Pathol.* **1,** 119–50 (2006).

27. McKinnell, R. G. *The biological basis of cancer*. (Cambridge University Press, 1998).

28. Ambrus JL Mink IB, Pickren JW, A. C. M. Causes of death in cancer patients. *J. Med.* **6,** 61–64 (1975).

29. Alberts, B. *Molecular biology of the cell.* (Garland Science, 2008).

30. Capco, D. G., Wan, K. M. & Penman, S. The nuclear matrix: Three-dimensional architecture and protein composition. *Cell* **29,** 847–858 (1982).

31. Spencer, V. a *et al.* Depletion of nuclear actin is a key mediator of quiescence in epithelial cells. *J. Cell Sci.* **124,** 123–32 (2011).

32. Dechat, T. *et al.* Nuclear lamins : major factors in the structural organization and function of the nucleus and chromatin. 832–853 (2008). doi:10.1101/gad.1652708.832

33. Lee, J. *The force in biology : understanding and measuring the role of cell mechanics in cancer and aging.* (VDM Verlag Dr. Müller, 2008).

34. Stewart, C. L., Roux, K. J. & Burke, B. Blurring the boundary: the nuclear envelope extends its reach. *Science* **318,** 1408–12 (2007).

35. Shivashankar, G. V. Mechanosignaling to the cell nucleus and gene regulation. *Annu. Rev. Biophys.* **40,** 361–78 (2011).

36. Wang, J. H.-C., Thampatty, B. P., Lin, J.-S. & Im, H.-J. Mechanoregulation of gene expression in fibroblasts. *Gene* **391,** 1–15 (2007).

37. Lindsay, P. K. and B. P. and P. C. and S. M. C. and S. M. V. and S. Hydrophobicity of methylated DNA as a possible mechanism for gene silencing. *Phys. Biol.* **9,** 65001 (2012).

38. Janmey, P. a. The cytoskeleton and cell signaling: component localization and mechanical coupling. *Physiol. Rev.* **78,** 763–81 (1998).

39. Mazumder, A., Roopa, T., Basu, A., Mahadevan, L. & Shivashankar, G. V. Dynamics of chromatin decondensation reveals the structural integrity of a mechanically prestressed nucleus. *Biophys. J.* **95,** 3028–35 (2008).

40. Caille, N., Thoumine, O., Tardy, Y. & Meister, J.-J. Contribution of the nucleus to the mechanical properties of endothelial cells. *J. Biomech.* **35,** 177–187 (2002).

41. Guilak, F., Tedrow, J. R. & Burgkart, R. Viscoelastic properties of the cell nucleus. *Biochem. Biophys. Res. Commun.* **269,** 781–6 (2000).

42. Dahl, K. N., Ribeiro, A. J. S. & Lammerding, J. Nuclear shape, mechanics, and mechanotransduction. *Circ. Res.* **102,** 1307–18 (2008).

43. Scianna, M. & Preziosi, L. Modeling the influence of nucleus elasticity on cell invasion in fiber networks and microchannels. *J. Theor. Biol.* **317,** 394–406 (2013).

44. Fu, Y., Chin, L. K., Bourouina, T., Liu, A. Q. & VanDongen, A. M. J. Nuclear deformation during breast cancer cell transmigration. *Lab Chip* **12,** 3774–8 (2012).

45. Gerlitz, G. & Bustin, M. The role of chromatin structure in cell migration. *Trends Cell Biol.* **21,** 6–11 (2011).

46. Wolf, K. *et al.* Physical limits of cell migration: control by ECM space and nuclear deformation and tuning by proteolysis and traction force. *J. Cell Biol.* **201,** 1069–84 (2013).

47. Voter, W. A. & Erickson, H. P. The Kinetics of Microtubule Assembly. **259,** 10430–10438 (1984).

48. De Forges, H., Bouissou, A. & Perez, F. Interplay between microtubule dynamics and intracellular organization. *Int. J. Biochem. Cell Biol.* **44,** 266–74 (2012).

49. Mofrad Kamm, Roger D., M. R. K. *Cytoskeletal Mechanics: Models and Measurements*. (Cambridge University Press, 2006).

50. Ingber, D. E. Cellular tensegrity: defining new rules of biological design that govern the cytoskeleton. *J. Cell Sci.* **104 (Pt 3,** 613–27 (1993).

51. Pokorný, J., Vedruccio, C., Cifra, M. & Kučera, O. Cancer physics: diagnostics based on damped cellular elastoelectrical vibrations in microtubules. *Eur. Biophys. J.* **40,** 747–59 (2011).

52. Stamenović, D., Mijailovich, S. M., Tolić-Nørrelykke, I. M., Chen, J. & Wang, N. Cell prestress. II. Contribution of microtubules. *Am. J. Physiol. Cell Physiol.* **282,** C617–24 (2002).

53. Nishimura, S. *et al.* Microtubules modulate the stiffness of cardiomyocytes against shear stress. *Circ. Res.* **98,** 81–7 (2006).

54. Lin, Y.-C., Koenderink, G. H., MacKintosh, F. C. & Weitz, D. a. Control of non-linear elasticity in F-actin networks with microtubules. *Soft Matter* **7,** 902 (2011).

55. Wang, N. Mechanical Interactions Among Cytoskeletal Filaments. *Hypertension* **32,** 162–165 (1998).

56. Harris, A. R. & Charras, G. T. Experimental validation of atomic force microscopy-based cell elasticity measurements. *Nanotechnology* **22,** 345102 (2011).

57. Rotsch, C. & Radmacher, M. Drug-induced changes of cytoskeletal structure and mechanics in fibroblasts: an atomic force microscopy study. *Biophys. J.* **78,** 520–35 (2000).

58. McGrath, J. L., Osborn, E. a, Tardy, Y. S., Dewey, C. F. & Hartwig, J. H. Regulation of the actin cycle in vivo by actin filament severing. *Proc. Natl. Acad. Sci. U. S. A.* **97,** 6532–7 (2000).

59. Ethier, C. R. & Simmons, C. A. *Introductory Biomechanics: From Cells to Organisms*. (Cambridge University Press, 2007).

60. Wang, F., Sampogna, R. V & Ware, B. R. pH dependence of actin self-assembly. *Biophys. J.* **55,** 293–8 (1989).

61. Yonezawa, N., Nishida, E. & Sakai, H. pH control of actin polymerization by cofilin. *J. Biol. Chem.* **260,** 14410–2 (1985).

62. Janmey, P. A. *et al.* The Mechanical Properties of Actin Gels. **269,** 32503–32513 (1994).

63. Pak, C. W., Flynn, K. C. & Bamburg, J. R. Actin-binding proteins take the reins in growth cones. *Nat. Rev. Neurosci.* **9,** 136–47 (2008).

64. Waugh, R. & Evans, E. A. Thermoelasticity of red blood cell. **26,** 115–131 (1979).

65. Boehm, H. *et al.* Mapping the mechanics and macromolecular organization of hyaluronan-rich cell coats. *Soft Matter* **5,** 4331 (2009).

66. Iyer, S., Gaikwad, R. M., Subba-Rao, V., Woodworth, C. D. & Sokolov, I. Atomic force microscopy detects differences in the surface brush of normal and cancerous cells. *Nat. Nanotechnol.* **4,** 389–93 (2009).

67. Stamenović, D., Fredberg, J. J., Wang, N., Butler, J. P. & Ingber, D. E. A microstructural approach to cytoskeletal mechanics based on tensegrity. *J. Theor. Biol.* **181,** 125–36 (1996).

68. Coughlin, M. F. & Stamenović, D. A prestressed cable network model of the adherent cell cytoskeleton. *Biophys. J.* **84,** 1328–36 (2003).

69. Provenzano, P. P., Inman, D. R., Eliceiri, K. W., Trier, S. M. & Keely, P. J. Contact guidance mediated three-dimensional cell migration is regulated by Rho/ROCK-dependent matrix reorganization. *Biophys. J.* **95,** 5374–84 (2008).

70. Berrier, A. L. & Yamada, K. M. Cell – Matrix Adhesion. 565–573 (2007). doi:10.1002/JCP

71. Shoulders, M. D. & Raines, R. T. Collagen structure and stability. *Annu. Rev. Biochem.* **78,** 929–58 (2009).

72. Wenger, M. P. E., Bozec, L., Horton, M. a & Mesquida, P. Mechanical properties of collagen fibrils. *Biophys. J.* **93,** 1255–63 (2007).

73. Tseng, Q. *et al.* A new micropatterning method of soft substrates reveals that different tumorigenic signals can promote or reduce cell contraction levels. *Lab Chip* **11,** 2231–40 (2011).

74. Balaban, N. Q. *et al.* Force and focal adhesion assembly : a close relationship studied using elastic micropatterned substrates. **3,** (2001).

75. Pietrucha, K. Changes in denaturation and rheological properties of collagen-hyaluronic acid scaffolds as a result of temperature dependencies. *Int. J. Biol. Macromol.* **36,** 299–304 (2005).

76. Scarth, G. W. THE ELASTICITY O F GELATIN IN RELATION TO PH AND SWELLING *. *J. Phys. Chem.* **29,** 1009–1022 (1925).

77. Pelling, A. E. & Horton, M. a. An historical perspective on cell mechanics. *Pflugers Arch.* **456,** 3–12 (2008).

78. Ulrich, T. a, Jain, A., Tanner, K., MacKay, J. L. & Kumar, S. Probing cellular mechanobiology in three-dimensional culture with collagen-agarose matrices. *Biomaterials* **31,** 1875–84 (2010).

79. Grinnell, F. & Petroll, W. M. Cell motility and mechanics in three-dimensional collagen matrices. *Annu. Rev. Cell Dev. Biol.* **26,** 335–61 (2010).

80. Powell, H. M. & Boyce, S. T. Engineered Human Skin Fabricated Using Electrospun Collagen–PCL Blends: Morphogenesis and Mechanical Properties. **15,** (2009).

81. Kaipparettu, B. A. *et al.* Novel egg white-based 3-D cell culture system. *Biotechniques* **45,** 165–8, 170–1 (2008).

82. Teresa, M. *et al.* Apoptosis , cell adhesion and the extracellular matrix in the three-dimensional growth of multicellular tumor spheroids. **36,** 75–87 (2000).

83. Ridley, A. J. *et al.* Cell migration: integrating signals from front to back. *Science* **302,** 1704–9 (2003).

84. Olson, M. F. & Sahai, E. The actin cytoskeleton in cancer cell motility. *Clin. Exp. Metastasis* **26,** 273–87 (2009).

85. Buchsbaum, R. J. Rho activation at a glance. *J. Cell Sci.* **120,** 1149–52 (2007).

86. Butcher, D. T., Alliston, T. & Weaver, V. M. A tense situation: forcing tumour progression. *Nat. Rev. Cancer* **9,** 108–22 (2009).

87. Tzima, E., Angel, M., Shattil, S. J., Chien, S. & Schwartz, M. A. Activation of integrins in endothelial cells by fluid shear stress mediates Rho-dependent cytoskeletal alignment. **20,** 4639–4647 (2001).

88. Riveline, D. *et al.* Focal Contacts as Mechanosensors: Externally Applied Local Mechanical Force Induces Growth of Focal Contacts by an Mdia1-Dependent and Rock-Independent Mechanism. *J. Cell Biol.* **153,** 1175–1186 (2001).

89. Sieminski, a L., Hebbel, R. P. & Gooch, K. J. The relative magnitudes of endothelial force generation and matrix stiffness modulate capillary morphogenesis in vitro. *Exp. Cell Res.* **297,** 574–84 (2004).

90. Friedrichs, J., Helenius, J. & Muller, D. J. Quantifying cellular adhesion to extracellular matrix components by single-cell force spectroscopy. *Nat. Protoc.* **5,** 1353–61 (2010).

91. Li, F., Redick, S. D., Erickson, H. P. & Moy, V. T. Force measurements of the alpha5beta1 integrin-fibronectin interaction. *Biophys. J.* **84,** 1252–62 (2003).

92. Kuznetsova, T. G., Starodubtseva, M. N., Yegorenkov, N. I., Chizhik, S. a & Zhdanov, R. I. Atomic force microscopy probing of cell elasticity. *Micron* **38,** 824–33 (2007).

93. Dumbauld, D. W. *et al.* Contractility modulates cell adhesion strengthening through focal adhesion kinase and assembly of vinculin-containing focal adhesions. *J. Cell. Physiol.* **223,** 746–56 (2010).

94. Galbraith, C. G., Yamada, K. M. & Sheetz, M. P. The relationship between force and focal complex development. *J. Cell Biol.* **159,** 695–705 (2002).

95. Grashoff, C. *et al.* Measuring mechanical tension across vinculin reveals regulation of focal adhesion dynamics. *Nature* **466,** 263–6 (2010).

96. O'Connor, K. & Chen, M. Dynamic functions of RhoA in tumor cell migration and invasion. *Small GTPases* **4,** 141–7 (2013).

97. Ridley, A. J., Paterson, H. F., Johnston, C. L., Diekmann, D. & Hall, A. The Small GTP-Binding Protein rat Regulates Growth Factor-Induced Membrane. **70,** 401–410 (1992).

98. Sander, E. E., Klooster, J. P., Delft, S. Van, Kammen, R. A. Van Der & Collard, J. G. Rac Downregulates Rho Activity : Reciprocal Balance between Both GTPases Determines Cellular Morphology and Migratory Behavior. **147,** 1009–1021 (1999).

99. Zondag, G. C. M. *et al.* Oncogenic Ras Downregulates Rac Activity , which Leads to Increased Rho Activity and Epithelial – Mesenchymal Transition. **149,** 775–781 (2000).

100. Palazzo, A. F., Cook, T. A., Alberts, A. S. & Gundersen, G. G. mDia mediates Rho-regulated formation and orientation of stable microtubules. **3,** 723–729 (2001).

101. Eden, S., Rohatgi, R., Podtelejnikov, A. V, Mann, M. & Kirschner, M. W. Mechanism of regulation of WAVE1-induced actin nucleation by Rac1 and Nck. **418,** 1–4 (2002).

102. Hall, A. Rho GTPases and the Actin Cytoskeleton. *Science (80-.).* **279,** 509–514 (1998).

103. Thiery, J. P., Acloque, H., Huang, R. Y. J. & Nieto, M. A. Epithelial-mesenchymal transitions in development and disease. *Cell* **139,** 871–90 (2009).

104. Yang, J. & Weinberg, R. a. Epithelial-mesenchymal transition: at the crossroads of development and tumor metastasis. *Dev. Cell* **14,** 818–29 (2008).

105. Mani, S. a *et al.* The epithelial-mesenchymal transition generates cells with properties of stem cells. *Cell* **133,** 704–15 (2008).

106. Radisky, D. C. & LaBarge, M. a. Epithelial-mesenchymal transition and the stem cell phenotype. *Cell Stem Cell* **2,** 511–2 (2008).

107. Lee, J. S. H., Chang, M. I., Tseng, Y. & Wirtz, D. Cdc42 mediates nucleus movement and MTOC polarization in Swiss 3T3 fibroblasts under mechanical shear stress. *Mol. Biol. Cell* **16,** 871–80 (2005).

108. Wolf, K. & Friedl, P. Extracellular matrix determinants of proteolytic and non-proteolytic cell migration. *Trends Cell Biol.* **21,** 736–44 (2011).

109. Lindemann, C. B. A CAMP-Induced Demembranated Increase in the Motility Bull Sperm Models of. **13,** 9–18 (1978).

110. Verkhovsky, A. B., Svitkina, T. M. & Borisy, G. G. Self-polarization and directional motility of cytoplasm. *Curr. Biol.* **9,** 11–S1 (1999).

111. Nabi, I. R. The polarization of the motile cell. *J. Cell Sci.* **1811,** 1803–1811 (1999).

112. Stroka, K. M. *et al.* Water permeation drives tumor cell migration in confined microenvironments. *Cell* **157,** 611–23 (2014).

113. Yamazaki, D., Kurisu, S. & Takenawa, T. Regulation of cancer cell motility through actin reorganization. *Cancer Sci.* **96,** 379–86 (2005).

114. Friedl, P. & Wolf, K. Plasticity of cell migration: a multiscale tuning model. *J. Cell Biol.* **188,** 11–9 (2010).

115. Friedl, P. & Alexander, S. Cancer invasion and the microenvironment: plasticity and reciprocity. *Cell* **147,** 992–1009 (2011).

116. Nguyen-Ngoc, K.-V. *et al.* ECM microenvironment regulates collective migration and local dissemination in normal and malignant mammary epithelium. *Proc. Natl. Acad. Sci. U. S. A.* **109,** E2595–604 (2012).

117. Mierke, C. T. Physical break-down of the classical view on cancer cell invasion and metastasis. *Eur. J. Cell Biol.* **92,** 89–104 (2013).

118. Wyckoff, J. B., Pinner, S. E., Gschmeissner, S., Condeelis, J. S. & Sahai, E. ROCK- and myosin-dependent matrix deformation enables protease-independent tumor-cell invasion in vivo. *Curr. Biol.* **16,** 1515–23 (2006).

119. Carey, S. P., Starchenko, A., McGregor, A. L. & Reinhart-King, C. a. Leading malignant cells initiate collective epithelial cell invasion in a three-dimensional heterotypic tumor spheroid model. *Clin. Exp. Metastasis* **30,** 615–30 (2013).

120. Tsuji, T., Ibaragi, S. & Hu, G. Epithelial-mesenchymal transition and cell cooperativity in metastasis. *Cancer Res.* **69,** 7135–9 (2009).

121. Ali, M. Y., Chuang, C.-Y. & Saif, M. T. a. Reprogramming cellular phenotype by soft collagen gels. *Soft Matter* **10,** 8829–37 (2014).

122. Grinnell, F. & Ho, C.-H. The effect of growth factor environment on fibroblast morphological response to substrate stiffness. *Biomaterials* **34,** 965–74 (2013).

123. Lovett, D. B., Shekhar, N., Nickerson, J. a, Roux, K. J. & Lele, T. P. Modulation of Nuclear Shape by Substrate Rigidity. *Cell. Mol. Bioeng.* **6,** 230–238 (2013).

124. Solon, J., Levental, I., Sengupta, K., Georges, P. C. & Janmey, P. a. Fibroblast adaptation and stiffness matching to soft elastic substrates. *Biophys. J.* **93,** 4453–61 (2007).

125. Liu, H., Sun, Y. & Simmons, C. a. Determination of local and global elastic moduli of valve interstitial cells cultured on soft substrates. *J. Biomech.* **46,** 1967–71 (2013).

126. Byfield, F. J. *et al.* Absence of filamin A prevents cells from responding to stiffness gradients on gels coated with collagen but not fibronectin. *Biophys. J.* **96,** 5095–102 (2009).

127. Gu, Y. *et al.* The influence of substrate stiffness on the behavior and functions of Schwann cells in culture. *Biomaterials* **33,** 6672–81 (2012).

128. Kim, T.-J. *et al.* Substrate rigidity regulates Ca2+ oscillation via RhoA pathway in stem cells. *J. Cell. Physiol.* **218,** 285–93 (2009).

129. Tee, S.-Y., Fu, J., Chen, C. S. & Janmey, P. a. Cell shape and substrate rigidity both regulate cell stiffness. *Biophys. J.* **100,** L25–7 (2011).

130. Poh, Y.-C., Chowdhury, F., Tanaka, T. S. & Wang, N. Embryonic stem cells do not stiffen on rigid substrates. *Biophys. J.* **99,** L19–21 (2010).

131. Bajaj, P., Tang, X., Saif, T. a & Bashir, R. Stiffness of the substrate influences the phenotype of embryonic chicken cardiac myocytes. *J. Biomed. Mater. Res. A* **95,** 1261–9 (2010).

132. Baker, E. L., Bonnecaze, R. T. & Zaman, M. H. Extracellular matrix stiffness and architecture govern intracellular rheology in cancer. *Biophys. J.* **97,** 1013–21 (2009).

133. Hotary, K., Allen, E., Punturieri, A., Yana, I. & Weiss, S. J. Regulation of Cell Invasion and Morphogenesis in a Three-dimensional Type I Collagen Matrix by Membrane-type Matrix Metalloproteinases 1 , 2 , and 3. **149,** 1309–1323 (2000).

134. Corte, V. De *et al.* Gelsolin-induced epithelial cell invasion is dependent on Ras ± Rac signaling. **21,** 6781–6790 (2002).

135. Koshikawa, N., Giannelli, G., Cirulli, V., Miyazaki, K. & Quaranta, V. Role of Cell Surface Metalloprotease MT1-MMP in Epithelial Cell Migration over Laminin-5. **148,** 615–624 (2000).

136. Shriver, M. *et al.* Loss of giant obscurins from breast epithelium promotes epithelial-to-mesenchymal transition, tumorigenicity and metastasis. *Oncogene* 1–12 (2014). doi:10.1038/onc.2014.358

137. Hoenerhoff, M. J. *et al.* BM1 cooperates with H-RAS to induce an aggressive breast cancer phenotype with brain metastases. *Oncogene* **28,** 3022–3032 (2009).

138. Moon, A. *et al.* Global gene expression profiling unveils S100A8/A9 as candidate markers in H-ras-mediated human breast epithelial cell invasion. *Mol. Cancer Res.* **6,** 1544–53 (2008).

139. Heidemann, S. R. & Wirtz, D. Towards a regional approach to cell mechanics. *Trends Cell Biol.* **14,** 160–6 (2004).

140. Koch, T. M., Münster, S., Bonakdar, N., Butler, J. P. & Fabry, B. 3D Traction forces in cancer cell invasion. *PLoS One* **7,** e33476 (2012).

141. Schoen, I., Hu, W., Klotzsch, E. & Vogel, V. Probing cellular traction forces by micropillar arrays: contribution of substrate warping to pillar deflection. *Nano Lett.* **10,** 1823–1830 (2011).

142. Wuang, S. C., Ladoux, B. & Lim, C. T. Probing the Chemo-Mechanical Effects of an Anti-Cancer Drug Emodin on Breast Cancer Cells. *Cell. Mol. Bioeng.* **4,** 466–475 (2011).

143. Tseng, Y., Kole, T. P. & Wirtz, D. Micromechanical mapping of live cells by multiple-particle-tracking microrheology. *Biophys. J.* **83,** 3162–76 (2002).

144. Wirtz, D. Particle-tracking microrheology of living cells: principles and applications. *Annu. Rev. Biophys.* **38,** 301–26 (2009).

145. Nelson Radosavljević, Marko., Bromberg, Sarina., P. C. *Biological physics : energy, information, life*. (W.H. Freeman and Co., 2004).

146. Mason, T., Ganesan, K., van Zanten, J., Wirtz, D. & Kuo, S. Particle Tracking Microrheology of Complex Fluids. *Phys. Rev. Lett.* **79,** 3282–3285 (1997).

147. Wang, N., Butler, J. P. & Ingber, D. E. Mechanotransduction across the cell surface and through the cytoskeleton. *Science (80-.).* **260,** 1124–1127 (1993).

148. Wang Ingber, Donald E., N. Probing transmembrane mechanical coupling and cytomechanics using magnetic twisting cytometry. *Biochem. Cell Biol. Biochem. Cell Biol.* **73,** 327–335 (1995).

149. Puig-de-morales, M. *et al.* Measurement of cell microrheology by magnetic twisting cytometry with frequency domain demodulation Measurement of cell microrheology by magnetic twisting cytometry with frequency domain demodulation. 1152–1159 (2001).

150. Poh, Y.-C. & Wang, N. The use of Optical Magnetic Twisting Cytometry and Flourescence Resonance Energy Transfer to quantify force-induced protein dissociation in the nucleus of a living cell . (2012). at <http://dx.doi.org/10.1038/protex.2012.012>

151. Fabry, B., Maksym, G. N., Hubmayr, R. D., Butler, J. P. & Fredberg, J. J. Implications of heterogeneous bead behavior on cell mechanical properties measured with magnetic twisting cytometry. *J. Magn. Magn. Mater.* **194,** 120–125 (1999).

152. Fabry, B. *et al.* Time scale and other invariants of integrative mechanical behavior in living cells. *Phys. Rev. E* **68,** 1–18 (2003).

153. Alcaraz, J. *et al.* Microrheology of human lung epithelial cells measured by atomic force microscopy. *Biophys. J.* **84,** 2071–9 (2003).

154. Guck, J. *et al.* The optical stretcher: a novel laser tool to micromanipulate cells. *Biophys. J.* **81,** 767–84 (2001).

155. Guck, J. *et al.* Optical deformability as an inherent cell marker for testing malignant transformation and metastatic competence. *Biophys. J.* **88,** 3689–98 (2005).

156. Remmerbach, T. W. *et al.* Oral cancer diagnosis by mechanical phenotyping. *Cancer Res.* **69,** 1728–32 (2009).

157. Klemuk, S. a, Jaiswal, S. & Titze, I. R. Cell viability viscoelastic measurement in a rheometer used to stress and engineer tissues at low sonic frequencies. *J. Acoust. Soc. Am.* **124,** 2330–9 (2008).

158. Desprat, N., Richert, A., Simeon, J. & Asnacios, A. Creep function of a single living cell. *Biophys. J.* **88,** 2224–33 (2005).

159. Mitchison, B. Y. J. M. & Swann, M. M. THE MECHANICAL PROPERTIES OF THE CELL. *J. Exp. Biol.* **31,** 443–460 (1954).

160. McConnaughey, W. B. & Petersen, N. O. Cell poker: An apparatus for stress-strain measurements on living cells. *Rev. Sci. Instrum.* **51,** 575 (1980).

161. Binnig, G., Quate, C. F. & Gerber, C. Atomic Force Microscope. *Phys. Rev. Lett.* **56,** 930–933 (1986).

162. Binnig, G. & Rohrer, H. Scanning tunneling microscopy. *IBM J. Res. Dev.* **30,** 355–369 (1986).

163. Lindsay, S. M. Introduction to nanoscience. (2010). at <http://public.eblib.com/choice/publicfullrecord.aspx?p=472316>

164. Hutter, J. L. & Bechhoefer, J. Calibration of atomic-force microscope tips. *Rev. Sci. Instrum.* **64,** 1868 (1993).

165. Butt, H.-J. & Jachke, M. Calculation of thermal noise in atomic force microscopy. *Nanotechnology* **6,** 1–7 (1995).

166. Walters, D. a. *et al.* Short cantilevers for atomic force microscopy. *Rev. Sci. Instrum.* **67,** 3583 (1996).

167. Heer, C. V. *Statistical Mechanics, Kinetic Theory, and STochastic Processes*. (Academic Press, Inc., 1972).

168. Passeri, D., Rossi, M. & Vlassak, J. J. On the tip calibration for accurate modulus measurement by contact resonance atomic force microscopy. *Ultramicroscopy* **128,** 32–41 (2013).

169. Burnham, N. a *et al.* Comparison of calibration methods for atomic-force microscopy cantilevers. *Nanotechnology* **14,** 1–6 (2003).

170. Mahaffy, R. E., Park, S., Gerde, E., Käs, J. & Shih, C. K. Quantitative analysis of the viscoelastic properties of thin regions of fibroblasts using atomic force microscopy. *Biophys. J.* **86,** 1777–93 (2004).

171. Lulevich, V., Zink, T., Chen, H.-Y., Liu, F.-T. & Liu, G. Cell Mechanics Using Atomic Force Microscopy-Based Single-Cell Compression. *Langmuir* **22,** 8151–8155 (2006).

172. Tao, N. J., Lindsay, S. M. & Lees, S. Measuring the microelastic properties of biological material. *Biophys. J.* **63,** 1165–9 (1992).

173. Hoh, J. H. & Schoenenberger, C. a. Surface morphology and mechanical properties of MDCK monolayers by atomic force microscopy. *J. Cell Sci.* **107 (Pt 5,** 1105–14 (1994).

174. Discher, D. E., Mohandas, N. & Evans, E. a. Molecular maps of red cell deformation: hidden elasticity and in situ connectivity. *Science* **266,** 1032–5 (1994).

175. Radmacher, M., Fritz, M., Kacher, C. M., Cleveland, J. P. & Hansma, P. K. Measuring the viscoelastic properties of human platelets with the atomic force microscope. *Biophys. J.* **70,** 556–567 (1996).

176. You, H. X. & Yu, L. Atomic force microscopy imaging of living cells: progress, problems and prospects. *Methods cell Sci.* **21,** 1–17 (1999).

177. Alonso, J. Feeling the forces: atomic force microscopy in cell biology. *Life Sci.* **72,** 2553–2560 (2003).

178. Wojcikiewicz, E. P., Zhang, X. & Moy, V. T. Force and Compliance Measurements on Living Cells Using Atomic Force Microscopy (AFM). *Biol. Proced. Online* **6,** 1–9 (2004).

179. Radmacher, M. Measuring the elastic properties of biological samples with the AFM. *IEEE Enginerring Med. Biol.* (1997).

180. Yin, F C P, C. K. Analysis of Indentation : Implications for Measuring Mechanical Properties With Atomic Force Microscopy. *J. Biomech. Eng.* **121,** 462–471 (1999).

181. Johnson, K. L. in *Contact Mech.* 1–17 (Cambridge University Press, 1985).

182. Sneddon, I. N. The relation between load and penetration in the axisymmetric boussinesq problem for a punch of arbitrary profile. *Intl. J. Engng Sci.* **3,** 47–57 (1965).

183. Briscoe, B. J., Sebastian, K. S. & Adams, M. J. The effect of indenter geometry on the elastic response to indentation. *J. Phys. D Appl. Phys.* **27,** 1156–1162 (1994).

184. Hertz, H. Ueber die Berührung fester elastischer Körper. *J. für die reine und Angew. Math. (Crelle's Journal)* **1882,** 156 (1882).

185. Trickey, W. R., Baaijens, F. P. T., Laursen, T. a, Alexopoulos, L. G. & Guilak, F. Determination of the Poisson's ratio of the cell: recovery properties of chondrocytes after release from complete micropipette aspiration. *J. Biomech.* **39,** 78–87 (2006).

186. Dhaliwal, R. S. & Rau, I. The axisymmetric Boussinesq problem for a thick elsatic layer under a punch of arbitrary profile. *Int. J. Engng Sci.* **8,** 843–856 (1970).

187. Lin, D. C., Dimitriadis, E. K. & Horkay, F. Robust strategies for automated AFM force curve analysis-II: adhesion-influenced indentation of soft, elastic materials. *J. Biomech. Eng.* **129,** 904–12 (2007).

188. *Handbook of Biological Confocal Microscopy*. (Springer, 2006).

189. Esposito, A. & Wouters, F. S. Fluorescence Lifetime Imaging Microscopy. *Curr. Protoc. Cell Biol.* **4.14.1,** 1–30 (2004).

190. Sanders, R., Draaijer, A., Gerritsen, H. C., Houpt, P. M. & Levine, Y. K. Quantitative pH Imaging in Cells Using Confocal Fluorescence Lifetime Imaging Microscopy. *Anal. Biochem.* **227,** 302–308 (995).

191. Schulz, O. *et al.* Simultaneous single molecule atomic force and fluorescence lifetime imaging. *Imaging* **7571,** 757109–757109–10 (2010).

192. Andl, C. D. *et al.* Epidermal growth factor receptor mediates increased cell proliferation, migration, and aggregation in esophageal keratinocytes in vitro and in vivo. *J. Biol. Chem.* **278,** 1824–30 (2003).

193. Palanca-Wessels, M. *et al.* Genetic analysis of long-term Berratt's esophagus epithelial cultures exhibiting cytogenetic and ploidy abnormalities. *Gastroenterology* **114,** 295–304 (1998).

194. Palanca-Wessels MC Reid BJ, Norwood TH, Opheim KE, Paulson TG, Feng Z, Rabinovitch PS, K. A. Extended lifespan of Barrett's esophagus epithelium transduced with the human telomerase catalytic subunit: a useful in vitro model. *Carcinogenesis* **24,** 1183–1190 (2003).

195. Wessels, J. T., Yamauchi, K., Hoffman, R. M. & Wouters, F. S. Advances in cellular, subcellular, and nanoscale imaging in vitro and in vivo. *Cytometry. A* **77,** 667–76 (2010).

196. Fuhrmann, A. *et al.* AFM stiffness nanotomography of normal, metaplastic and dysplastic human esophageal cells. *Phys. Biol.* **8,** 015007 (2011).

197. Li, Q. S., Lee, G. Y. H., Ong, C. N. & Lim, C. T. AFM indentation study of breast cancer cells. *Biochem. Biophys. Res. Commun.* **374,** 609–13 (2008).

198. Lulevich, V., Shih, Y.-P., Lo, S. H. & Liu, G.-Y. Cell tracing dyes significantly change single cell mechanics. *J. Phys. Chem. B* **113,** 6511–9 (2009).

199. Roduit, C. *et al.* Elastic membrane heterogeneity of living cells revealed by stiff nanoscale membrane domains. *Biophys. J.* **94,** 1521–32 (2008).

200. Costa, K. D., Sim, A. J. & Yin, F. C.-P. Non-Hertzian approach to analyzing mechanical properties of endothelial cells probed by atomic force microscopy. *J. Biomech. Eng.* **128,** 176–84 (2006).

201. Smith, P. G., Roy, C., Zhang, Y. N. & Chauduri, S. Mechanical stress increases RhoA activation in airway smooth muscle cells. *Am. J. Respir. Cell Mol. Biol.* **28,** 436–42 (2003).

202. Chen, C. S. & Ingber, D. E. Tensegrity and mechanoregulation: from skeleton to cytoskeleton. *Osteoarthritis Cartilage* **7,** 81–94 (1999).

203. Sheen, V. L. *et al.* Filamin A and Filamin B are co-expressed within neurons during periods of neuronal migration and can physically interact. *Hum. Mol. Genet.* **11,** 2845–54 (2002).

204. Fiori, J. L. *et al.* Filamin A modulates kinase activation and intracellular trafficking of epidermal growth factor receptors in human melanoma cells. *Endocrinology* **150,** 2551–60 (2009).

205. Abràmoff, M. D., Hospitals, I., Magalhães, P. J. & Abràmoff, M. Image Processing with ImageJ. *Biophotonics Int.* **11,** 36–42 (2004).

206. Guo, S. & Akhremitchev, B. B. Packing density and structural heterogeneity of insulin amyloid fibrils measured by AFM nanoindentation. *Biomacromolecules* **7,** 1630–6 (2006).

207. NCI OPSO. *Cell Line Protocol.* (Physical Sciences - Oncology Centers Network, 2010).

208. Gonzalez-Malerva, L. *et al.* High-throughput ectopic expression screen for tamoxifen resistance identifies an atypical kinase that blocks autophagy. *Proc. Natl. Acad. Sci. U. S. A.* **108,** 2058–63 (2011).

209. Boulbitch, a. Deflection of a cell membrane under application of a local force. *Phys. Rev. E* **57,** 2123–2128 (1998).

210. Hillebrand, U. *et al.* 17beta-estradiol increases volume, apical surface and elasticity of human endothelium mediated by Na+/H+ exchange. *Cardiovasc. Res.* **69,** 916–24 (2006).

211. Yonezawa, N. *et al.* Distribution among Tissues and Intracellular Localization of Cofilin , a 21kDa Actin-Binding Protein. *Cell Struct. Funct.* **12,** 443–452 (1987).

212. Denker, S. P. *et al.* Direct Binding of the Na – H Exchanger NHE1 to ERM Proteins Regulates the Cortical Cytoskeleton and Cell Shape Independently of H Translocation. *Mol. Cell* **6,** 1425–1436 (2000).

213. Putney, L. K., Denker, S. P. & Barber, D. L. The Changing Face Of The Na + / H + Exchanger, NHE1 : Structure , Regulation, and Cellular Actions. *Annu. Rev. Pharmacol. Toxicol.* **42,** 527–52 (2002).

214. McDonagh, E. M., Whirl-Carrillo, M., Garten, Y., Altman, R. B. & Klein, T. E. From pharmacogenomic knowledge acquisition to clinical applications: the PharmGKB as a clinical pharmacogenomic biomarker resource. *Biomark. Med.* **5,** 795–806 (2011).

215. Mabjeesh, N. J. *et al.* 2ME2 inhibits tumor growth and angiogenesis by disrupting microtubules and dysregulating HIF. *Cancer Cell* **3,** 363–75 (2003).

216. Shen, J. & Pappano, A. J. An Estrogen Metabolite , 2-Methoxyestradiol , Disrupts Cardiac Microtubules and Unmasks Muscarinic Inhibition of Calcium Current. *Pharmacology* **325,** 507–512 (2008).

217. Carbonaro, M., Brate, A. O. & Giannakakou, P. Microtubule disruption targets HIF-1alpha mRNA to cytoplasmic P-bodies for translational repression. *Cell* **192,** 83–99 (2011).

218. Kamath, K. *et al.* 2-Methoxyestradiol suppresses microtubule dynamics and arrests mitosis without depolymerizing microtubules. *Mol. Cancer Ther.* **5,** 2225–33 (2006).

219. Chua, Y. S., Chua, Y. L. & Hagen, T. Structure activity analysis of 2-methoxyestradiol analogues reveals targeting of microtubules as the major mechanism of antiproliferative and proapoptotic activity. *Mol. Cancer Ther.* **9,** 224–35 (2010).

220. Harvey, B. J., Condliffe, S. & Doolan, C. M. Sex and salt hormones: rapid effects in epithelia. *News Physiol. Sci.* **16,** 174–7 (2001).

221. Liaw, Y. *et al.* PKC activation is required by EGF-stimulated Na+/H+ exchanger in human pleural mesothelial cells PKC activation is required by EGF-stimulated Na+/H+ exchanger in human pleural mesothelial cells. *Am J Physiol Lung Cell Mol Physiol* (1998).

222. Gundimeda, U., Chen, Z. H. & Gopalakrishna, R. Tamoxifen modulates protein kinase C via oxidative stress in estrogen receptor-negative breast cancer cells. *J. Biol. Chem.* **271,** 13504–14 (1996).

223. Schiff, R. *et al.* Oxidative Stress and AP-1 Activity in Tamoxifen- Resistant Breast Tumors In Vivo. *J. Natl. Cancer Inst.* **92,** (2000).

224. Lin, X. *et al.* Overexpression of PKCalpha is required to impart estradiol inhibition and tamoxifen-resistance in a T47D human breast cancer tumor model. *Carcinogenesis* **27,** 1538–46 (2006).

225. Nabha, S. M. *et al.* Upregulation of PKC-delta contributes to antiestrogen resistance in mammary tumor cells. *Oncogene* **24,** 3166–76 (2005).

226. Pandey, D. P. *et al.* Estrogenic GPR30 signalling induces proliferation and migration of breast cancer cells through CTGF. *EMBO J.* **28,** 523–32 (2009).

227. Ignatov, A., Ignatov, T., Roessner, A., Costa, S. D. & Kalinski, T. Role of GPR30 in the mechanisms of tamoxifen resistance in breast cancer MCF-7 cells. *Breast Cancer Res. Treat.* **123,** 87–96 (2010).

228. Ariazi, E. A. *et al.* The G Protein-Coupled Receptor GPR30 Inhibits Proliferation of Estrogen Receptor-Positive Breast Cancer Cells. *Clin. Cancer Res.* **70,** 1184–1194 (2011).

229. Quist, A. P., Rhee, S. K., Lin, H. & Lal, R. Physiological role of gap-junctional hemichannels. Extracellular calcium-dependent isosmotic volume regulation. *J. Cell Biol.* **148,** 1063–74 (2000).

230. Hurtado, A. *et al.* Regulation of ERBB2 by oestrogen receptor – PAX2 determines response to tamoxifen. *Nature* **456,** 3–8 (2008).

231. Prossnitz, E. R. *et al.* Estrogen signaling through the transmembrane G protein-coupled receptor GPR30. *Annu. Rev. Physiol.* **70,** 165–90 (2008).

232. Storey, J. D. & Tibshirani, R. Statistical significance for genomewide studies. *Proc. Natl. Acad. Sci. U. S. A.* **100,** 9440–5 (2003).

233. Dudoit, S., Shaffer, J. P. & Boldrick, J. C. Multiple Hypothesis Testing in Microarray Experiments. *Stat. Sci.* **18,** 71–103 (2003).

234. Atkinson, K. E. & Shampine, L. F. Algorithm 876 : Solving Fredholm Integral Equations of the Second Kind in M ATLAB. **34,** (2008).

235. Bloom, R. J., George, J. P., Celedon, A., Sun, S. X. & Wirtz, D. Mapping local matrix remodeling induced by a migrating tumor cell using three-dimensional multiple-particle tracking. *Biophys. J.* **95,** 4077–88 (2008).

236. Pillé, J.-Y. *et al.* Anti-RhoA and anti-RhoC siRNAs inhibit the proliferation and invasiveness of MDA-MB-231 breast cancer cells in vitro and in vivo. *Mol. Ther.* **11,** 267–74 (2005).

237. Poincloux, R. *et al.* Contractility of the cell rear drives invasion of breast tumor cells in 3D Matrigel. *Proc. Natl. Acad. Sci. U. S. A.* **108,** 1943–8 (2011).

238. Wang, Y.-L. & Pelham, R. J. J. Preparation of a flexible porous polyacrylamide substrate for mechanical studies of cultured cells. *Methods Enzymol.* **298,** 489–496 (1998).

239. Seifriz, W. An Elastic Value of Protoplasm, with further Observations on the Viscosity of Protoplasm. *Br. J. Exp. Biol.* **11,** (1924).

APPENDIX A

DETAILED PROTOCOL FOR INDENTATION OF CELLS IN COLLAGEN

Contents

1) Collagen Gel Preparation
   a) Materials
   b) Equipment
   c) Cleaning Dishes
   d) Plasma-treating Dishes
   e) Functionalizing Dishes
   f) Coating Dishes with Collagen
   g) Staining Dishes with Fluorescent Dye
   h) Seeding Dishes with Cells
   i) Staining Cells with fluorescent Dye

2) Setting up the experiment
   a) Setting up the optics
      i) Starting the software
      ii) Cleaning an objective
      iii) Uninstalling and installing an objective
      iv) Using the laser to focus on a glass surface
      v) Aligning a dichroic mirror
      vi) Installing and aligning a pinhole
      vii) Setting up the supercontinuum light source for confocal microscopy
   b) Setting up the AFM
      i) Starting the software
      ii) Installing an AFM probe
      iii) Approaching a surface
      iv) Doing a force curve
      v) Calibrating an AFM probe
         (1) Correcting virtual deflection
         (2) Determining inverse optical lever sensitivity
         (3) Determining spring constant by thermal noise method
         (4) Getting invOLS in liquid

3) Conducting the measurements
   a) Aligning the tip in the confocal volume
   b) Doing confocal scans of the sample
   c) Doing a co-registered line scan of indentations on the sample

4) Data Analysis
   a) Pre-processing
   b) Curve-fitting in MATLAB

1) Collagen Gel Preparation

a) Materials

- Fluorodishes (World Precision Instruments, Item#: FD5040-100)
- Cloth (e.g. ITX Texwipe, TX609 TechniCloth 9" x 9" Wiper)
- Ultrapure water (Millipore Milli-Q Synthesis 25 MΩ)
- Ethanol (preferably spectroscopic grade)
- APTES (fresh and freshly prepared)
- Glutaraldehyde
- Dulbecco's Phosphate Buffered Saline (10X)
- Sodium Hydroxide
- Nutragen Bovine Collagen I (Advanced Biomatrix, Catalog #5010-D)
- Fluorescent dye for labelling collagen (e.g. Atto 465 NHS)

b) Equipment

- Chemical fume hood
- Ultrasonicator
- Oxygen plasma cleaner
- Laminar flow bench
- Biosafety cabinet
- Incubator (5% CO2, 37 °C)
- Refrigerator (4 °C)
- Beakers, pipetters, ice bucket, ice machine

c) Cleaning Dishes

i) Thoroughly clean 2 140 ml glass beakers with soap and DI water at the sink and return them to the fume hood.

ii) Clean the bench surface in the fume hood and put a X609 nonwoven wiper down (a clean lint-free paper towel, essentially); this is where you will put your dishes during functionalization.

iii) Bring 4 fluorodishes into the hood and open the packaging. Put aside the lids, taking care to avoid getting them dusty.

iv) Fill one of your beakers with ~120 ml ethanol, making sure the ethanol is clean without any cloudiness or particulates. Using a forcep, place the 4 dishes in the ethanol and sonicate. A watch glass can be used to cover the beaker to avoid dust.

v) After sonication in ethanol, fill your other beaker with ~120 ml Millipore water. Using a forcep, move the 4 dishes from the ethanol into the Millipore and sonicate. The ethanol you use can be placed back into the bottle for reuse afterwards.

vi) Put the lids back on and bring the dishes over to the laminar flow bench. Blow them dry with nitrogen. (Note: some tanks of nitrogen have contained contaminants that can scratch and ruin the dishes; the dishes can instead be air dried in the laminar flow bench by leaning them vertically against something).

vii) Place them in a styrofoam box and bring them down to the basement for plasma cleaning. Don't forget to bring gloves.

d) Plasma-treating Dishes

i) Open the oxygen tank. Suit up and bring the samples to the clean room. Place the dishes in the plasma cleaner chamber.

ii) Turn on the pump and power, close the door with the valve in the horizontal position. The vacuum will seal the door closed. Wait 3 minutes for the air inside to be purged.

iii) Turn the valve to the up position. The pressure gauge should fall to 500 psi. This should take about 30 seconds. The pressure may be unstable and fluctuate. It may take a few minutes to stabilize to 500 psi. In practice, if it stabilizes at a different pressure results will not vary appreciably.

iv) Turn the plasma on and set it to High. Wait 3 minutes. The chamber should have a purple haze if oxygen plasma is working properly.

v) After 3 minutes, Turn off all three switches and turn the valve to the down position. The chamber will re-pressurize and the door will pop open. Take you samples out, un-suit, close the oxygen tank, and return to the chemical fume hood.

e) Functionalizing Dishes

i) Prepare a fresh solution of 11.88 ml ethanol + 120 μl APTES in a 15 ml falcon tube.

ii) Place 3 ml of solution in each dish. Put the lids on and wait 30-60 minutes.

iii) Use an ethanol squirt bottle to wash each dish 5-10 seconds to remove unbound APTES.

iv) Then use a DI water squirt bottle to wash each dish 5-10 seconds.

v) Prepare a solution of 0.5% Glutaraldehyde in 1X DPBS. Place 3 ml of solution in each dish. Put the lids on and wait 60 minutes.

vi) After, use a DI water squirt bottle to thoroughly wash each dish 20-30 seconds to remove unbound glutaraldehyde.

vii) Blow them dry with nitrogen. (Note: some tanks of nitrogen have contained contaminants that can scratch and ruin the dishes; the dishes can instead be air dried in the laminar flow bench by leaning them vertically against something).

f) Coating Dishes with Collagen

i) Prepare a clean working surface in the biosafety cabinet.

ii) Take an ice bucket to the ice machine in PSH hallway. Get a microvial and fill it with Millipore water.

iii) Get a bottle of 0.1 M NaOH and a bottle of 10X DPBS, and a bottle of Nutragen (Advanced Biomatrix, Catalog #5010-D) from the fridge. Make sure it is not expired. Spray them all down, put them in the ice, spray down the ice bucket, and put them in the cabinet.

iv) To prepare a 4.88 mg/ml gel, Add 100 µl 10X PBS, 75 µl 0.1 M NaOH, and 25 µl Millipore to a microvial on ice. Allow it to chill for a few minutes.

v) Bring your functionalized dishes into the cabinet.

vi) Add 800 µl of Nutragen to your microvial using a 1 ml pipetter. Use the pipetter to mix the solution. Keep it set at 800 µl and pipette up and down ~80 times. Do not pipette fully, just go from ~25-75% of the range repeatedly, with the tip near the bottom of the vial. The solution must be thoroughly mixed to improve homogeneity. You want to keep your eye on it while you mix so as not to allow any air bubbles into the solution.

vii) Using a 200 µl pipette tip, pipette 200 µl of your collagen solution onto the center of a dish. Pick up the dish in your hand and use the side of the pipette tip to push the collagen from the center to the edges. Do not touch the pipette tip to the surface, only break the surface tension of the collagen droplet. Use the surface tension to carefully spread the droplet across the entire glass. Do this by holding the pipetter stationary, and holding the dish at a 45deg angle, then rotate the dish with your fingers. Gravity will help the droplet spread. Push the solution all the way around, even covering the ridge at the glass/plastic interface. Repeat for all four dishes, using a new 200 ul pipette tip each time.

viii) Put the lids on and place all four dishes in the incubator for 90 minutes.

ix) Place some 1X DPBS in the water bath beforehand and after 90 minutes*, bring the dishes back into the biosafety cabinet. Using a 1 ml pipetter, place 1 ml PBS on the center of the collagen. The collagen may be quite hydrophobic so the PBS will stay in the middle.

**The longer you wait, the more your gels will dehydrate, resulting in a thinner, stiffer gel.*

x) Add another 2 ml PBS, the liquid should spread out more, but might not completely cover the collagen. Gently slide the dish back and forth ~1-2" while on the bench surface to get the PBS to cover the entire surface, both glass and plastic. Repeat for all four dishes, and return them to the incubator.

Polymerization is a continuous process. Collagen polymerization occurs gradually and 'full polymerization' is an approximate, equilibrium condition, which is reached logarithmically over time. At this point, you will achieve more consistent polymerization if you allow the gels to incubate overnight before staining or seeding.

g) Staining Dishes with Fluorescent Dye

i) Add 2.5 μl (up to 10 μl is fine too) of 5 μM Atto 465-NHS to 1 ml of 1X DPBS, mix/shake it up.

ii) Aspirate the PBS from the dishes and pipette the dye solution onto the collagen. Incubate for at least 45 minutes (longer is fine too), aspirate, and replace dye solution with 2 ml 1X DPBS. You may use other dyes, or collagen specific antibody conjugated dyes, if desired. The Atto 465 NHS will label the collagen non-specifically, so be sure to wash away any free dye before seeding with cells.

h) Seeding Dishes with Cells

i) The dishes can now be seeded with cells. MDA-MB-231 cells are subcultured according to the PSOC Cell Line Exercise Protocol. After trypsinization, centrifugation, and resuspension, take ~50 μl (this will depend on your initial cell density and desired final cell density, so do a cell count first if you want to get it right) of resuspended cells/media and pipette it into 1-2 ml of warm (37 °C) media.

ii) Use the aspirator to remove the PBS from the dish, taking care not to touch or remove any collagen. Pipette the cells/media onto the collagen and return the dishes back to the incubator.

iii) The cells will need at least 4-6 hours (preferably 24 hours) to adhere to the collagen. Invasive MDA-MB-231 cells may begin to invade the gel. About half of the cells should be fully invaded into the gel within a week. Exchange the media every other day while the cells are on the gel.

i) Staining Cells with fluorescent Dye

i) If you want to fluorescently label the cells, do so now, before your experiment. Cells can be labeled with e.g. plasma membrane dye (CellMask Deep Red HCS, Invitrogen). Add 2.5 μl of 5mg/ml Cell Mask to 1 ml of 1X DPBS, mix/shake it up.

ii) Aspirate the media from the dish. Pipette the staining solution onto the cells and incubate for 30 minutes. Membrane dyes will diffuse into the cytoplasm over time due to lipid recycling; your best images of the membrane will be 30-60 minutes after staining.

Your samples are now ready for indentation and imaging.

2) Setting up the experiment

Multi-tasking is not recommended, just take your time and do everything correctly the first time. It will save you time in the end.

Sometimes software glitches. The best approach is to begin your session with freshly rebooted computers. Turn off the Microtime 200 router, PI digital piezo controller (whose switches are on the front), and both Sepia Boxes (Sepia II & Picoharp 300, whose switches are on the back). Make sure the FastGate cable (which is used by other users in the lab) is NOT plugged into either Laser Channel on the front of the Sepia II. Wait a few seconds and turn them all back on. Reboot both computers. Unless you are having AFM-specific problems, you should always leave the AFM controller ON, due to improved stability.

a. Setting up the optics

i) Setting up the software

(1) On the confocal computer, from the desktop, open the wxPropview, click Use, click Live.

(2) Next Open Sepia II. If you want to use the blue 470 nm laser, check the '1' box under Burst Out. If you want the red 670 nm laser, check the '2' box under Burst out. If you want both, check both. If you want both to fire simultaneously, Set the Burst Length to '1' in row 1 and all other Burst lengths to '0', and check 'Sync Enable'.

This setting will give you the lifetimes from both lasers accurately. However unless you split the FLIM image into separate channels, the colors will be overlapped and you won't be able to distinguish the channels by their lifetimes. If you want the two channels to be separated by color in the merged image and don't need accurate lifetimes, you can instead delay the firing of red laser to fire 25 ns after the blue laser in each pulse sequence. This way the red laser lifetimes will be 25 ns longer than they really are. To do this, have both Burst Out checked and set Burst Length to '1' in the first and the second row, and check Sync Enable in both rows. It is recommended however to fire them simultaneously and get the true lifetimes for most applications. The invert check box should remain unchecked, the base oscillator should be 80 MHz with Divider "2". The blue laser (Slot 200) intensity should be 37% with Falling (ext.) trigger. The red laser (Slot 300) intensity should be

29% with Falling (ext.) trigger. The Intensities can be adjusted if you need different laser powers for your application, or could even be set to continuous mode-but this would result in fast photobleaching for most dyes. Then make sure to hit 'apply', a couple times doesn't hurt. The laser(s) are now firing. Minimize the window.

(3) Now open SymphoTime 5.13 (Operation). It will say "Unable to open framegrabber device" because you are using wxPropView as your framegrabber. Click OK. Go to File New/Load Workspace. Click 'Show Oscilloscope', 'Operate Shutters', and 'Data Acquisition: Video'. In the Shutter Control, click on the red X to the left. This opens the electronic shutter that allows the lasers from the optical fiber into the confocal optical beam path.

Now if you look at the objective, you should see a (red, blue, or both=purple) dot coming out of the center of the aperture.

If you do not see it, go to the laser enclosure and try dialing the micrometer wheel (which controls a ND filter) counterclockwise to increase the power, or turn the filter to a lower number (0 is the least (none) ND filter). If you still don't see any laser power either at the aperture or on the Intensity (A.U.) readout in the Data Acquisition: Video window, it means your lasers are not entering the confocal optical beam path. Check the excitation filter in the Microtime200. Make sure it is not obstructed by anything (e.g. a spare dichroic). Most likely your issue is in the laser enclosure. Open the laser enclosure. The flip mirror should be flipped down (out of the path) to send the beams into the fiber to the confocal. If it is flipped up, the beams will be sent out of the box and into the path that feeds into the back of the IX71 (for widefield and TIRF etc). Use a paper target to follow the beam up to the dichroic, and to then between the IX-71 and the dichroic. If you see the beam here but not through the objective, you will need to align the dichroic, or your objective is not installed properly. If you can see the laser at the aperture, you are ready to install your sample.

ii) Cleaning an objective

iii) Uninstalling and installing an objective

(1) Use an ethanol kimwipe to clean the eyepieces of the IX-71.

(2) Choose your objective.

For thick samples, you will need to use the 60X water objective. For thin samples, you should use the 100X oil objective. The air objectives can be used but only need to be used under special circumstances (thick samples, problematic sample undersides etc.)

(3) To install an objective, you need to remove the sample stage.

(a) Before you begin, if there is an objective already installed, you must make sure to dial the focus all the way down so the objective is as far away from the stage as possible.

(b) Then remove the AFM head, carefully and without twisting the cable, and place it on the table.

(c) Next use the micrometer to bring the sample stage all the forward, closest to you.

(d) Then with the small flathead screwdriver, remove the spring in the front right corner, place it where you won't lose it and don't let it fly away when you pop it off.

(e) Now you may lift the sample stage up and out of the way (e.g. resting on eyepiece column).

(4) You can now access the objective, and carefully unscrew the currently installed objective out, and put it in its bag/container.

When screwing or unscrewing any objective into a cap of a container, hold the objective stationary in your hand and turn the cap- you don't want to accidentally drop the objective.

(5) Now you can install the desired objective

(a) Screw the objective in gently, without stripping the threads or forcing it in at all. Don't screw it in too tightly, just enough that there is no wiggle.

(b) Put the stage back together.

(c) Wipe down the whole stage with ethanol using a kimwipe. There is sometimes dust/residue etc from the previous user.

(d) Next you will need to add a small droplet of water to the water objective, or a small drop of oil to the oil objective.

For the oil objective, there should already be oil on it, but usually I add a tiny amount (not a whole drop, just whatever is on the applicator by surface tension when you pull it out of the oil bottle) initially, since every time you change the sample, the amount of oil on your objective decreases some.

Bring the objective all the way up to apply the droplet, and then bring it back down before installing your sample.

iv) Using the laser to focus on a glass surface
(This method is always useful and is especially needed when focusing on a surface that doesn't have objects on it that are visible through the eyepiece.)

1. You will need a clean glass fluorodish to align the pinhole.

   Wipe both sides of the dish with a kimwipe onto which you have applied a small drop of pure ethanol from the ethanol squirt bottle in the AFM room. It is recommended that you keep one of these calibration dishes for yourself in a safe place in the AFM room labelled in a box so that you can reuse the dish for this purpose. This will reduce waste. You could even have one for the water objective, one for the oil objective, and one for AFM calibration. If you hang on to them, they should last forever and you don't need to keep using new dishes.

2. Place the dish on the sample stage.

3. The dish has four plastic tabs, one of them is smaller than the others. The dish fits on the stage best if you place the small tab toward your right, on the side with the cable for the dish heater.

4. Next you want to secure the dish using the magnetic sample holder.

   We have two. Notice that one of them has the magnetic screws installed in the opposite way from the other with respect to the top plate. Specifically, the top plate is flat on one side and has a recess on the other. For fluorodishes, you want to use the one in which the top plate has the recessed side facing down, toward the magnetic side of the screws. The height of the screws should already be roughly correct, and this provides a 'lip' that makes it more secure. Place the holder over the dish, listening for a 'snap'. You don't want it to snap, which is telling you the magnets in the screws are in full contact with the magnets on the sample stage. Get down at eye level so you can see the space between the stage and the holder. You want to screw the screws so that all four of them have an equal amount of space between them and the magnets on the stage. The idea is that the magnetic force will hold your sample down, without transmitting mechanical vibrations (as would happen if the magnets were in contact).

5. Now you want to be looking at wxPropView. You should see some light, and the light should change if you move the objective up and down a little.

6. Now you can raise the objective up until your water or oil comes into contact with the glass.

   If using an air objective, you should get in focus before you get too close to the surface- i.e. the objective should never touch the glass. You should keep a close eye on the water/oil contact and make sure that you don't get an air bubble. If you see even the tiniest little air bubble, you will NEED to remove your dish, wipe off the underside with an ethanol kimwipe, and then pop the bubble in the water/oil. To pop the bubble, use the dry corner of a clean kimwipe. Use the flashlight. If it doesn't pop, try another (dry) corner. You may find you need to push the bubble to the edge of the oil/water and use the surface tension to

pop it. If you are having trouble, you can always clean off the objective completely and add new oil/water.

7. When your backscattered light is brightest, you are focused on the top surface of the glass. Lower the intensity (using the micrometer and/or the ND filter wheel at the laser enclosure) until you can only see the center of the pattern and the four lobes.

   You should see a pattern of radially symmetric interference. If you now turn the laser intensity down you should see the pattern reduce to a small pattern with four lobes. Each objective, and each laser, results in a slightly different pattern. It should be relatively crisp and symmetric. If the lobes change length asymmetrically as you defocus and refocus, you may need to adjust the beam by adjusting the alignment of the dichroic.

v) Aligning a dichroic mirror

vi) Installing and aligning a pinhole

For YZ confocal scans your best resolution will be achieved if you use the smallest pinhole (30 μm). If the right pinhole is already installed, you should not need to align it, (as it should have been aligned by whomever installed it last) unless you are getting poor images.

1. Now that you have focused on the glass surface, and the dichroic is aligned, it is time to install and align the pinhole. For this, it is important to stay in focus on the surface. Because the stage is in better mechanical equilibrium when the AFM head is weighing down on it, you should now put the AFM head back on the stage.

   Do so by moving it in such a way that you take the same (reversed) path as you took to remove it, so as not to put any kinks or twists in the cable. Because of the added weight, you will need to dial the objective down a few micrometers in order to regain your focus on the top glass surface.

   If you will be using both lasers, it is debatable whether you should align the pinhole using red (longer wave), blue (shorter wave), both (co-optimized), or whichever color channel requires the better axial resolution. Try them all and see, it shouldn't be too critical. You may find that using the other laser or both to align the pinhole would result in needing to turn the knobs slightly in order to get the max amplitude, and this is because the beams may not lie perfectly on top of each other. It should be good enough either way.

2. Now set the ND filter to 3 and turn the filter micrometer so the Intensity A.U. readout is quite low (~1 a.u.). You will use reflected light into SPAD1. To send all the reflected light to SPAD 1, disengage from the beampath the beamsplitter between SPAD 2 and SPAD 1 by pulling the rod all the way up.

3. Next remove the emission filter from in front of SPAD 1. Remember to put the emission filter and the beamsplitter (rod in middle position) back into the path when you are done. If you have not already done so, turn on the SPADs by hitting Channel 1 Select and Channel 2 Select (one at a time) on the Microtime router.

4. Finally you are ready to open the electronic shutter in front of SPAD1 by clicking the red X above the icon labeled 'I' in the Shutter Control window.

5. Go to the PicoHarp: Time Trace window. Press Start. Watch the time trace. Ensure the trace is working by varying the focus or intensity slightly and seeing that the amplitude changes accordingly. Turn the lights on and off in the room. The amplitude should change a little bit since you have the Microtime box lid off and some of the ambient light is coming into the detector. Therefore you want to leave the lights off for this and use a flashlight to see what you are doing. Change the counts axis to Lin and adjust the min and max so the range is tighter around your amplitude.

6. Dial the objective up and down until the amplitude is at a maximum. Now you will screw the (30 μm) pinhole gently into the pinhole mount. While doing so, you will see the amplitude drop off. Once it is all the way screwed in, readjust the min and max again so it is in your amplitude range. Now just turn one of the knobs back and forth (just a little bit in either direction at first). If the amplitude does not change considerably turn it back to where it was. If it increases and then decreases when you turn it in one direction, turn it to the local maximum. Then do the same for the other knob. While doing this, the stage may still be mechanically settling, and the objective may be drifting out of position, so routinely go back and change the focus of the objective until it maximizes the amplitude. Repeat the procedure going from knob to knob to objective until you have tweaked it until you cannot get the amplitude any higher.

7. Note that you want to be maximizing the amplitude in the time trace, not the Average Intensity in Cts. value.

8. Once you are happy with it, you are done aligning the pinhole. Press Stop, Close the SPAD1 Shutter, Close the Laser Shutter, put the emission filter and beamsplitter back in the path, put the lid back on the box, and turn the room lights back on.

vii) Setting up the supercontinuum light source for confocal microscopy

b) Setting up the AFM

i) Starting the software

1. The controller should be on. On the AFM computer, double-click the 'AR 101010+1006' icon to open Igor. After a moment, it should say ARC Ready and Ready. File>Load AFM Software. Heater Panel\Controls\Mode: On & \Feedback: On. Set Target temp (e.g. 37°C for cells) Master Panel\Main\Set Point: 0.1V. Master Panel\Main\Path… set your path to a folder for your experimental data.

2. I like to center the stage immediately. Master Panel\Main\Scan Size: 80 um. Frame Down. Wait for the Retrace windows to update to the new frame size. Press Stop. Master Panel\Force\Go There\ check Show Markers, check Show Tip, set Spot Number to '0', click Go There. Now the center of your sample scanning stage is centered below the AFM tip.

ii) Installing an AFM probe

1. Make a space at the computer desk where you can comfortably install the holder.

2. Get the small (black and red handle) flathead and Phillips head screwdrivers, the cantilever holder base, and the cantilever holder you will be using.

> *For force measurements, you will want to use the one that does NOT say '5E8' handwritten in silver on the side).*

3. Pop the cantilever holder into the base.

4. Inspect the cantilever holder.

> *Make sure that there is no debris under the clip. If a previous user broke a tip and was not careful there may be chunks of silicon under the clip. Make sure the two small outer screws are screwed in securely. You should not need to screw or unscrew these normally, avoid unnecessarily wearing out the screws. Use an ethanol kimwipe to clean the surface of the holder.*

5. Loosen the center screw. Place the end of the flathead screwdriver under the clip, propping it open slightly. Get the forcep/tweezer that you are most comfortable using to handle the probe.

> *I prefer the "broken" one with the bent end for some reason- it's just personal preference.*
>
> *If you are using a probe from a wafer, you probably want to use a sharper tweezer to remover the probe from the wafer. Come down around the sides of the probe chip, holding the tweezer nearly vertically. Grasp it firmly and rock the tweezer back and forth until the tabs on the sides crack free.*

6. Pick up the chip with the tweezer.

    a. With the tweezer grasping the center of the sides of the probe chip, rock back and forth from side to side until the chip is no longer stuck to the gel surface it is sitting on. Try not to crack the sides of the probe too much, but a little bit is ok.

    b. Once it is free, you can regrip the probe for the installation. You want to perform this with one fluid motion.

If you need to try again, just rest the probe back on the gel surface and pick it up again. You want to grip the front of the sides (closer to the cantilever end) with the tweezer, so there is ample room to tuck the back end in under the clip on the holder. You should orient the holder and the box so you can do this with minimal movement.

c. Take your time, exhale, and transfer the probe to the holder so the back is tucked under the clip, and release the tweezer from the probe.

d. Carefully pull out the flathead screwdriver. The clip should tighten down slightly onto the probe. Now turn the base so the cantilever is parallel to your line of sight, pointing to the wall in front of you (away from you).

e. Now use the tweezer to place the probe into perfect position.

You want it to be centered (not at an angle, not straight-but-off-center) and also you want the tip to sit approximately over the center of the prism. Spend a minute getting it exactly right, you don't want to have to do this again.

f. Once it is positioned as good as you can get it, rotate the base 90° and get at eye level with the probe.

g. Use the Phillips head to tighten the center screw.

You will see the gap close and the probe get pushed downward. DO NOT overtighten or you will crack your chip. You want to tighten it just so when you turn the screwdriver any further without holding the base, the base will rotate a little. Sometimes friction causes the probe to twist clockwise by a few degrees. If so loosen and try again. If it happens every time, compensate by positioning the tip at a slight counterclockwise angle so tightening it will straighten it out.

h. Now that your probe is installed in the base, bring the base to the AFM head.

It is helpful now to use the bubble level to take a look at whether the head is level and how high the head is raised. First set the level on the (silver metal) stage and see where the bubble rests. Now put the level on the head and see where the bubble rests. Typically the previous user only raises the front legs up after use and leaves the back legs positioned so that when the front legs are lowered, the front legs and the back legs are level when the probe is near the surface. However, it is critical to be aware that not all samples are the same thickness, so the back legs may be very high or low relative to your sample if a thick sample was measured previously. In this case, if you were only to adjust the front legs and come into contact, your AFM would not be level, and ***you will have problems****.*

7. Dial the front legs up a good amount, because the next time you put the head back, it will have a tip in it, and it will have a glass dish under it, and you don't want to instantly crash your tip on the glass because the head wasn't raised.

8. Then remove the AFM head, turn it upside down, remove the holder from the base, and install the holder into the head. Hold in the button while you do so, and give the holder a little push in both directions after you release the button. It should move a little both ways. Push down a bit on it and feel it to ensure that it is sprung in properly.

9. If you are doing relatively long experiments on cells in liquid, you will now want to install the transparent annular membrane. Wipe it down thoroughly with ethanol to sterilize it, then place it over the cantilever holder. It will act as a dish cover. This will reduce evaporation, keep the temperature more stable, and reduce contamination.

10. Lower the objective out of the way. Get a clean glass dish. Wipe it with water with a kimwipe. Dry it. Wipe it with thoroughly ethanol with a kimwipe. Dry it. Install it on the stage with the sample holder as described above. Click once on the Camera Icon in the bottom pane of Igor. Turn the AFM lamp on with the remote control knob on the table. Place the AFM head back on the stage.

11. There are two little knobs sitting next to each other sticking out of the very back of the AFM head that control the mirror that directs the lamp light (and camera view-field) down through and to the probe. Adjust the knobs so you can see your cantilever in the **Video** window.

    If you notice the cantilever is at an angle in the plane, you should reposition it in the holder now. If you notice the cantilever looks whitish, it is reflecting light because it is at an angle normal to the plane (ie not parallel to the cantilever holder surface like it should be). This could mean your probe is bent (broken). It could also mean you need to reposition the probe. Sometimes this means it is tucked in under the clip too far or not far enough. Other times it means the screw is not tight enough. Try and try again. If your AFM head is dialed way, way up or is very unlevel, you may also get this problem. If it is level and not too far from the surface, you should try a different tip.

12. Next, turn the lamp intensity down. Go to the AFM controller and turn the key to turn the AFM laser diode On. You should see at least a faint whitish blue haze in the Video window coming from the laser. Now you want to get the laser onto the back of the cantilever. Use the **LDX** and **LDY** wheels on the head to move the laser spot. Once you find the spot in the **Video** window, move it to the cantilever. Once it is on the lever, you will see the **Sum** increase.

    If you are not getting a sum, even though it looks like it is on there, you may be looking at a reflection of the laser spot, instead of the real spot. In this case, use only **LDY** *to move the reflection up or down, until you find the true spot. If the true spot is not giving you a*

sum, or a very weak sum, it may be your cantilever is bent or in the case of a (heavily) used probe, the reflective coating is worn off and you can't get a signal so you need to get a new probe. Try repositioning the probe in the holder before giving up on it.

I typically try to work with **0.00 Lateral**. *Usually slight adjustment of* **LDY** *will get you to 0 lateral, and then adjust both* **LDY** *and* **LDX** *to maximize the Sum. You want a strong signal for force measurements.*

13. Once you have your sum, adjust the **PD** wheel on the AFM head so the **Deflection** is **0**. This is called 'zeroing your deflection'.

14. Ensure that your **Setpoint** is **0.1 V**.

15. **Ensure that the volume is up on the AFM computer, the speakers are turned on (the blue led is on)**. You will want to hear the *Ding* when you reach the glass. Click **Engage**. You will see the **Z Voltage** swing to the right in the **Sum** and **Deflection Meter** window. Now you are going to dial down to the surface.

iii) Approaching a surface

1. Check the bubble level. You want the AFM head to be level when you are at the surface. To do this, you may or may not need to dial both the front and the back wheels down as you approach. Often, especially when everyone is using the same thickness of sample, you will only need to dial the front down. However if you are calibrating on glass but your sample is going to be a few hundred micrometers thicker (like a thick collagen gel for example), then level for calibration won't be exactly level for your sample, so keep this in mind. It doesn't need to be perfectly level, but if it is way off when you get to the surface you could have problems or even crash your tip. Dial the wheels down slowly. You should be staring at the sum and deflection meter, while doing this, as well as looking at the level and the Video window.

   Note: if your deflection is changing at all or significantly as you approach, it is probably due to long range forces between the tip and the surface. This means your surface is dirty. Sometimes you have to clean over and over alternately with water and ethanol to get it right. Dial up the head, clean the glass, and try again. Start over with a new glass if necessary. Note also that freshly opened fluorodishes are not necessarily clean. It is ok if it happens a little bit. Often you need to re-zero your deflection with the PD wheel a few times as you approach.

2. Dial down until you hear the Ding. This means your probe is touching the surface and is being bent by an amount equal to 0.1V. 1V would be bent more. Look at the Z Voltage, and dial the front wheel down until the Z voltage is in the center (no red or blue) or a little past the center (a couple of millimeters into the blue). Click Withdraw. The deflection shouldn't change much when you withdraw since your surface is clean. Zero the deflection.

3. Now you should really check your level. If it is off by, say, a radius of the bubble or more, you want to raise the front (or back, depending on which way it is off) a few turns, hit engage, then lower the back (or front) legs until you hit the surface again. Repeat this until your bubble is level on the surface.

iv) Doing a force curve

1. Now that you are level and on the surface, do a force curve.

2. Master Panel\Force\Force Dist: 10 μm (radio button selected).

3. Master Panel\Force\Velocity: 2 μm/s (radio button selected).

4. Trigger Channel: DeflVolts. Increasing. Relative.

5. Trigger Point: 1.0 V. (It is important that everyone uses the same trigger force for this so that the determined sensitivity is relatively consistent across experiments).

6. Click Single Force.

7. After the curve is completed, click Withdraw.

8. Note there are two withdraw buttons. Since you are not engaged, you cannot click Withdraw in the Sum and Deflection Meter. Click Master Panel\Force\Withdraw to withdraw to get -10.00 Zvoltage.

> *Note: when doing force curves, only either the Start Dist or Force Dist value can be selected at a time, depending on which one has the radio button. Same for the Scan Rate and the Velocity. You want to have Force Dist and Velocity settings obeyed, so make sure the radio buttons are selected for them, otherwise the AFM won't do force curves the way you want it to.*

9. How does it look? Hopefully the baseline is linear parallel and flat.

v) Calibrating an AFM probe

(1) Correcting virtual deflection

(a) Now that you have found the surface, you actually want to leave it again already. Dial the front up say, 100 μms (= ten little 10 μm turns). Now you want to do a full-range force curve with no trigger, to move your probe up and down (only through the air without touching the surface) through the entire z range (which is 40 μm). That's why you want to make sure you are MORE than (40 μm + tip height) from the surface before you do this, or you could crack the tip.

(b) Zero your deflection.

(c) Master Panel\Force\Trigger Channel: None

(d) Click Single Force.

(e) You will see the Z Voltage change as the piezo moves the probe up and down. After the curve is done, you will see the curve pop up in the ForceGraph1:Deflection vs ZSensor window. Hopefully the red and blue lines are linear and not curved.

(f) If you are lucky the blue and red lines are not only linear but flat. If instead they are divergent like a "<" sign, it may mean your cantilever deflection is changing over time due to temperature changes like a thermistor. This is 'thermal drift'. Go get a coffee and come back in ten minutes and see if it is still bad. If so, you may need to re-position the cantilever or get a new one, or it could be that the AFM controller is warming up due to being recently turned off and on (try waiting a bit longer).

(g) When assessing the curve, mind the range of the Y axis. Igor autoscales the axis ranges. If they are nonlinear and you are in air above glass, you may want to troubleshoot this. If they are linear and parallel but not flat, it means that you have a technical artifact from the optical path of the laser diode called 'virtual deflection' that you should now correct for.

(h) Click on the ForceGraph window so it is the current window.

(i) Hit Ctrl-I on the keyboard; a little panel will pop up below the current window. The Click and drag the circle to one end of the baseline. Click and drag the square to the other end of the baseline. You can use either the red (approach) or blue (retract) line, but try to drop both the circle and the square on the same line.

(j) Next go to Master Panel\Force\Cal. and from the dropdown menu that says Set Sensitivity, choose Virtual Defl Line.

(k) If your baseline is curved, you can choose Virtual Defl Poly, but it may be better to figure out what is wrong instead in this case, since the theoretical justification for this correction is somewhat lacking. For force analysis of deep indentations on soft samples, it is very important to have flat baselines. Doing a virtual deflection correction is therefore very important. But it is undoubtedly much more preferable to have flat baselines in the first place without the need for this type of correction (either poly OR linear). The software is subtracting a line or polynomial from your data to make it look flat. Using polynomial corrections can result in weird, wrong, force curves if the curve is performed outside the range that was used for the fit. .

(l) When in Open-Loop, the ramp voltage of the piezo is linear, but since the piezo is non-linear, then the piezo velocity is non-linear, and since the hydrodynamic drag is proportional to the velocity, this produces non-linear hydrodynamic drag, which empirically seems to be responsible for the wedge-shaped non-triggered full-range force distance curves. Switch to Closed-Loop Mode or try a slower approach velocity to reduce the effect. As of June '12, the extended Z-head in our setup has some non-linear virtual deflection that Asylum does not yet understand (https://support.asylumresearch.com/forum/showthread.php?1288-virtual-deflection-correction&highlight=).

(m) That being said, the magnitude in deflection of the correction is roughly 0.1% the magnitude of the force curve. Given that the calibration is rarely better than 10%, the virtual deflection correction should not be a worry, except when it hinders your ability to determine the contact point accurately, or in the case where it is important that all of your curves to trigger at exactly the same force.

(n) Now do the force curve again. If your force curve is in air above the glass, it will probably look very noisy. That's just because Igor zoomed in on the deflection axis because it is flat now. You can change the axis range to what it was, to verify that it is flat. (How?)

(o) Click engage. Make sure the deflection is 0. Change the Trigger Channel to DeflVolts and the Trigger Point to 1.0 V. Using the front wheel on the AFM head, go back down to the surface.

(p) Once you here the ding and have a Z voltage in the center, do another Single Force. You should see that the baseline is flat. If not, go back to the previous step. If so, proceed.

(2) Determining inverse optical lever sensitivity

(a) Do a single force curve on the surface with a long Force Distance (15 or 20 μm).

(b) Use a trigger force of 1 V. Unfortunately even on glass the slope is not linear, at lower forces the slope is less steep, and it straightens out and becomes steeper as you push harder. In order for results to be consistent across different experiments, it is important to fit the same region of the curve each time you get the sensitivity. Fit the steep linear region from about 0.5 V to 1 V.

(c) In the contact region of the curve, left click and drag a square to select the part of the curve where you are pushing against the glass, plus a bit of the baseline. Let go of the mouse and then right click in the selection, and select Expand to zoom in one this region. Ideally because the glass is rigid there should be very little hysteresis and the approach and retract should be very linear and parallel.

(d) There are some changes in the forces at contact and with large soft probes there is in practice a little bit of a steepening and straightening effect as you push harder. Typically if you fit in the 0.2 – 0.5 deflVolt range this part should be nice and straight. If not, you can increase your trigger force a little bit and try again. If you are getting quite nonlinear curves it may mean there is some soft debris on your tip or on the surface and you will have to backtrack (different glass, different probe, new virtual deflection correction, etc.).

(e) Hit Ctrl-I and set the cursors around a straight flat region of the (red) approach curve. Again ideally red and blue are the same and it's all straight and flat. If it is not very flat, try doing another force curve with a higher trigger value.

(f) Main Panel\Force\Cal.\Set Sensitivity: Defl InvOLS.

(g) This sets the number of nm of deflection that correspond to the number of Volts on the photodetector. Therefore this calibration is specific to the particular current position of the laser spot on the back of the cantilever, and any touching of the LDX or LDY wheels, or any changes of the Sum, will invalidate the calibration and require you to do a new invOLS calibration.

(h) The whole reason for calibrating on glass in air is because you need to get invOLS on a rigid surface and it is more accurate to record the thermal noise spectrum in air than in liquid. But this is an intermediate step in finding the cantilever spring constant. The next step is to measure the thermal noise spectrum. Before you measure your cells you will in fact need to get another invOLS in liquid.

(3) Determining spring constant by thermal noise method

(a) From the previous step you just did a force curve on the glass. Click Withdraw.

(b) Now dial the front wheel up ~ 30 μm. Zero the deflection. Master Panel\Thermal click Capture Thermal Data

(c) I collect 100 counts before clicking Stop Thermal Capture.

(d) For LRCH probes change the Zoom Center to ~15 kHz.

(e) Then Initialize Fit. Inspect the fit. Adjust the width and the center until you get a good fit.

(f) Then click Fit Thermal Data.

(g) The software uses your invOLS and your thermal to calculate your spring constant. The spring constant for LRCH probes should be about 150 pn/nm.

(h) When you get your spring constant, click the Lock icon to lock it into the settings for your experiment.

(4) Getting invOLS in liquid

(a) Since your measurements will be in liquid (buffer) which has a different refractive index, your invOLS will be different. Now that you have the spring constant you need to measure the invOLS on glass in liquid. It may be a good idea to use the exact liquid you will measure in, but water should be good enough. If you are doing measurements on glass or plastic with a cell density that is sufficiently low that the probe can indent the substrate, this step can be performed on your sample. It will be more accurate in principle and faster.

(b) Give the front wheel a few turns to raise it up, and remove the AFM head and place it upside down on the table.

(c) Pipette ~ 1ml DI water onto your glass dish.

(d) Pipette a small droplet (~20 μl) onto your cantilever.

(e) Now place the AFM head back on the stage.

(f) You want to have the AFM lamp on and be staring at the Video window while you bring the probe into the liquid. If the cantilever was in sharp focus in air, you will need to refocus the AFM camera to get it in focus in liquid. You will notice that your sum has changed and your laser spot has moved. Check that you do not see any air bubbles stuck to the cantilever, the tip, or the chip. If you do have an air bubble, try raising the probe in and out of the liquid repeatedly and hope the surface tension will pull the bubble off. If this doesn't work, use the edge of a kimwipe to dry off the cantilever holder (without touching the cantilever) and re-wet it. If this doesn't work, you maybe have to remove the cantilever holder and dry it off with nitrogen and re-wet it. Once you are bubble free, proceed.

(g) If you will be measuring at 37 °C, it is probably a good idea to let your liquid equilibrate now. You can watch it warm up (Heater Panel\Data\Live Graph\More).

(h) If the cantilever is whitish in the Video window, or if you have no sum at all, it maybe be deflected because it is not yet in the liquid. As long as you know you are still far from the surface, dial it down until it enters the liquid. It will change appearance and the sum should increase (if the spot is still on the cantilever).

(i) Use LDX and LDY to maximize the sum. The maximum sum in liquid will be considerably lower than in air due to scattering.

(j) Once you have a good sum, hit engage and go down to the surface, again with a set point of 0.1V.

(k) Once it dings, you may hear a beeping noise and see the Z Voltage oscillate wildly. If this happens, simply reduce the integral gain (Master Panel\Main\Integral Gain: 1) to a lower value. Once it stops beeping, you can try sneaking the gain back up and you may be able to bring it back up to 3 without resonating. If not, measuring with a gain of 1 is sufficient.

(l) Do another force curve with 1V trigger, fit the region in the ~0.5V-1V region, and set setnsitivity (DeflVolts).

3) Conducting the measurements

a) Aligning the tip in the confocal volume

i) At this point, if you haven't already done so, (and if you already did, verify that it is still the case) center the AFM probe with respect to the sample stage. [Note: sometimes over time the red dot indicating the tip's position appears to be nudged~2 μm off center. Make sure it is spot on before doing your alignment.] Master Panel\Main\Scan Size: 80 μm. Frame Down. Wait for the Retrace windows to update to the new frame size. Press Stop. Master Panel\Force\Go There\ check Show Markers, check Show Tip, set Spot Number to '0', click Go There. Now the center of your sample scanning stage is centered below the AFM tip.

ii) Once your objective is focused on the gel-liquid interface, hit "Engage" (again, set point 0.1 V) and bring the probe to the gel surface. You should use the eyepiece to see that as you get closer to the surface, the cantilever will get closer to being in focus.

iii) Hopefully/normally you can see the probe in the eyepiece. If not, you should make a note of the current positions of the main stage micrometers (the big ones one the left), because you don't want to get lost and go too far astray, and begin turning them a bit and try to locate the cantilever. Once you find it, bring the end of the cantilever (ie the tip) (approximately) into the crosshairs before continuing to approach. This allows you to make sure that you don't come down on a cell- use the sample stage micrometers (the small ones on the right) to move the sample with respect to the probe and get any cells away from the crosshairs.

iv) You will hear the Ding when your probe is on the surface. You should be able to see the tip (small black dot) on the surface and even see the gel deform. Once you are in contact, hit Master Panel\Force\Withdraw.

v) Now is a good time to check out the gel by doing a force curve. Change the Trigger Channel to Force and set the Trigger to ~ 3-5 nN, with a large force distance (type in 30 um and it will give you what it can).

vi) This will give you a ~few um deep indentation. Hopefully, you will get a nicely shaped curve without any adhesion, not much hysteresis, no wobbles, and a flat baseline. Often you will not be so lucky. If it looks good, proceed. If not, you should troubleshoot here before going further. You may have a gel that is especially sticky, or isn't properly polymerized. You may have already gotten debris all over the tip, which ruins the force response. You may need to re-correct the virtual deflection at this point. Especially if you had deflection change proportionally (+/-) with Z as you approached- this is a virtual deflection. As always, think about what may have gone wrong, backtrack to the earlier point in this procedure that works correctly, and work forward until you get back to this point before you proceed. Hopefully you don't have to backtrack too far.

vii) Now dial up the front wheel 100 μm.

viii) You need to do this because next you need to unpark the objective scanner in SymphoTime, which could potentially push the sample up into the probe. Hit "UnPark Scanner" in SymphoTime Scan window. The objective will move, the cells will go out of focus, and the cantilever will no longer be in the crosshairs. Note that if your tip had been aligned, and the scanner parked/unparked itself, you would in much the same way, totally lose your alignment. You don't want to waste your time aligning with a parked scanner, because the alignment will be lost before you can use it.

ix) This is a good time to think about your objective scanner's z position. For example if you will be doing YZ scans and you want the gel surface to sit in the middle of the image, set Z = 50 μm now and then focus on the surface using the focus wheel. That way if z ranges 10-90 μm in an 80x80 μm scan, the surface will be halfway down the scan.

x) Now that the tip is centered on the sample stage and the objective scanner is unparked, bring the tip approximately into the crosshairs once again, hit Engage and bring it onto the surface (not onto a cell) until it dings.

xi) Now comes the debatable question of at what height or z-piezo position should you do the fine alignment of the tip. Ideally the tip would move straight up and down in the line of the beam axis and that would make this a non-issue; however the cantilever is at an angle with the piezo stack and the sample surface, so there may be some movement out of the beam axis as you move the tip up and down. (In reality there is not much movement and it does not pose a problem). This would suggest you would do the fine alignment at the exact height where it is most sensitive to get accurate coregistration of force and fluorescence data, which in our case would be the top of the partially embedded cell. But not every cell has the same height, and the gel surface is not even perfectly flat or level, so you have to make a compromise. You could also do the alignment with the tip just barely in contact with the gel. This approach works well because you can see the change in the reflection at the interface. If you do it this way, you can just go to the surface and stop your approach exactly when it dings, without hitting withdraw. Make sure at this point NOT to accidentally move the sample stage

(small micrometers on the right). That would drag the tip through the gel. Make sure in SymphoTime that the shutters in front of both SPADs are CLOSED.

xii) Now it is time to definitively locate the actual point of the tip. To do this, raise the intensity of the AFM lamp quite high. (Try to do this relatively quickly, cells don't like bright lights). You should see the small black dot near the end of the cantilever.

xiii) Turn the eyepiece so your crosshairs are vertical and horizontal.

xiv) Now you want to move the big micrometers on the left (the main stage) and bring that black dot into the upper left quadrant. Depending on which objective you will want it in a slightly different spot. For example, if you are using the 100X objective the dot should be North of the horizontal crosshair by about the width of the cantilever, and West of the vertical crosshair by about half the width of the cantilever. Focus sharply on the black dot.

xv) The only time you should ever use the big micrometers on the right is when you want to move the AFM probe with respect to the objective. Do not accidentally use the big micrometers to move the sample or you will lose your alignment!

xvi) You can turn the lamp down or off.

xvii) Now, you should pull the rod out on the IX71, and turn open the laser shutter (not the detector shutters, just the laser shutter, I.e. the one on the left).

xviii) Look at wxPropView. You will see the laser light, and it should be reflecting off the tip. Note the position of the laser spot stays the same in the camera field of view. Use the big micrometers to move the probe so the tip into this spot. Adjusting the focus and using the lamp and laser together will help. When the laser is shining on the tip, you will get a bright spot that, when you shift the tip position slightly, will have 'lobes' that shine off it at different angles. When the lobes are shining straight at you, you have aligned the tip as much as possible.

xix) Now, hit Main Panel Force\Withdraw. Your tip is aligned in the confocal volume and you are ready to begin poking cells.

b) Doing confocal scans of the sample

i) Now in SymphoTime, getting your scan parameters optimal is important. You want high quality images, but also you need to go reasonably quickly so you can collect data from a good number of cells from each dish. There is a balance between getting a lot of information from each cell (e.g. a 3d z-stack and a full forcemap) and getting good statistics. If the cells aren't too big, a 60 μm X 60 μm scan size, 0.2 s/pixel, 256 x 256 pixels, monodirectional scan, with 20% acceleration and 5 learning loops, seems to be a good compromise. Note: bidirectional is twice as fast, but often introduces artifacts from

the sample vibrating in and out of focus. Try it first and see if it is adequate and it might save a lot of time.

ii) Do an XY scan. In Symphotime\Data Acquisition\Point window Scan Axis Assignment select X/Y Scan. Then in SymphoTime\Data Acquisition\Area window, set position X: 10, Width X: 80, position y: 10, Width Y: 80, 256 x 256 pixels. Options: Accleration 20%, Time per pixel 2 (x 0.2 ms), Learning Loops 5, Monodirectional, OK. Apply. Record.

iii) After your XY scan, perform a YZ confocal scan of the cell. In Symphotime\Data Acquisition\Point window Scan Axis Assignment select Y/Z Scan. Then in SymphoTime\Data Acquisition\Area window, set position X: 10, Width X: 80, position y: 10, Width Y: 80, 256 x 256 pixels. Options: Accleration 20%, Time per pixel 2 (x 0.2 ms), Learning Loops 5, Monodirectional, OK. Apply. Record. Note: If your YZ scan is too high or low, put the Z piezo to 50 μm and then focus on the surface or the region of interest.

c) Doing a co-registered line scan of indentations on the sample

i) Now on the AFM computer, go to Programming>MacroBuilder. On the right hand side, Load>RoryLineMacroYZ40um. You want to setup the filenames for the force curves you will collect associated with the cell you are currently measuring. MasterPanel\Force\Save\BaseName: "cell01_". The file names will have numbers 0000-0019 appended to them in sequence. Then in MacroBuilder hit "Run". This macro will first send the tip to "Point 0". Note that you need to tell the software where Point 0 is, in the first place. If you do a 20 x 20 μm scan and then Force>Go There.Spot Number 0>Pick Point, your Point 0 will be at (10 μm, 10 μm) on the scanner range. If you then do a 80 x 80 μm scan and re-pick Point 0, it will move to (40 μm, 40 μm). It is best to use the latter as your Point 0. Next the macro nudges the probe 19 μm in the -Y direction. Thereafter, it performs a single force curve, and then moves 2 μm in the +Y direction. The parameters you have currently set in the Master Panel\Force menu are the parameters used by the macro. It then continues perfoming a single force curve and moving two um, for a total of 20 times. That is your first curve is at (x=40 μm, y=21 μm) and your last curve is at (40 μm, 59 μm). Finally it nudges back 19 μm in the –Y direction, returning the probe back to Point 0.

ii) Watch the curves. If they don't look good from the beginning, stop the macro by hitting the Run button (it will have a Stop icon above while running) ONCE (you have to wait for the current force curve to complete. Go back to Point zero and look in the eyepiece that you are where you think you are and haven't lost alignment. If so you will need to realign, which means you need new confocal scans too. You want curves with long flat baselines (~10+ μm baselines) and the indentation should be ~5 μm. For the global fit of the young's modulus, you want to fit the 0.25-2.5 μm range of each curve, so each curve needs to be at least 2.5 μm deep. Depending on your spring constant (k~0.15 N/m), a trigger force of ~3-5 nN should be in the right ballpark. Sometimes you get curves if the probe is stuck to something, like a sticky patch of collagen. If so, try dialing

up a few tens of μm, which could pull off anything stuck to the tip. You also need to watch that every curve triggers. Otherwise you will get an incomplete tomogram. If your curve doesn't trigger, it will say "never triggered" in the Untitled window (the command terminal), and the curve will not be plotted in the ForceGraph window. If you are getting good curves, but you get some that don't trigger, you can re-do the force line without re-aligning and re-imaging the cell. Simply stop the macro somewhere on the collagen, so the tip is at, say, (40,21) away from the cell. Then hit engage, go to the surface, and withdraw. Then start the macro over. It will write over any old force curves with the same names and you will get a complete tomogram. When the macro is done, click Master Panel\Force\Withdraw. Verify that you are at point 0. In the eyepiece, verify your alignment was maintained.

iii) Once you get a good set of cell images (XY and YZ) with good alignment and a good set of force curves from it, you have gotten the complete dataset for the cell. You can now pick out a new cell and continue collecting data from your dish. You should keep an eye on the cell morphology. If you are in the right buffer at 37°C with the dish membrane, you should be able to measure for 3 or even 4 hours before needing to begin with a new dish. This should enable you to collect data from ~20 cells from a dish, and a few dishes in a (long) shift. You should also keep track of your Sum and make sure that it does not change by more than a few percent—if it does, you will need to re-do your calibration. It is good practice to re-align the tip between every cell you measure. It will become habitual and only takes a minute. By getting fast at it and doing it every time you will spend less time in the long run and get better data. Make sure you know which tip you used. Record the tip use in the log at Dropbox\group\Big Tips\LRCH Tips.xlsx

d) Shut down and cleanup.

4) Data Analysis

a) Pre-processing

i) Before you begin, you will need ImageJ and MATLAB. Assuming you have access to the Ros lab Group directory on Dropbox, you will also need to download the Matlab force curve analysis working directory from: Dropbox\group\MATLAB Code\2013.07.03 Force Curve Analysis.

ii) In order to perform the analysis, for each cell you will need to inspect the YZ confocal image to identify which curves *0000-*0019 are from (purely) the cell and which are from (purely) the collagen. You should right these down in a log somewhere ahead of time so that you can simply enter the relevant values into your script when you are ready to process the data in matlab.

iii) One relatively easy way to do this is by using a mask in ImageJ. For 512x512 pixel 80x80 um scans and 20 indentations spaced 2 um apart, there is a mask available at D:\Dropbox\group\rory\80x80_512x512_mask.bmp. To use it, Open your YZ bitmap of your cell. Make sure you are using a mask of appropriate dimensions for your scan size and resolution. First, YOU MUST HORIZONTALLY FLIP YOUR YZ IMAGE since left to right on the YZ confocal image corresponds to down-to-up, not up-to-

down, on the sample scanner. To flip it, click on your image, then Image>Transform>Flip horizontally. Now open the mask. Go to Process>Image Calculator…> Set Image 1 to your YZ scan and Image 2 to the mask, and use Operation XOR (other operations may work well enough too), check Create New Window, click OK. Now you will see your image with the locations of the curves clearly identified, assuming the tip was aligned. Now just write down which curves were on collagen and which were on the cell. Do this 'preanalysis' for all of your partially embedded cells. You will also need to record the z positions of the apical cell surface, the basal cell surface, and the collagen surface. You can change it to um if you go to Image>Properties>Unit of length: micrometer, and then fill in the correct pixel width and height (i.e. how many micrometers the pixel width and height are). Click Global if all of your images have the same size and resolution. Then use the mouse to hover over each surface and record the Y value that is listed in the ImageJ window.

iv) Now that you have all of your preprocessing done, you can fit the curves.

b) Curve-fitting in MATLAB

i) Open MATLAB and navigate to the force curve analysis folder on your hard drive, so that it is your working directory. For each of your cells, you should have your 20 curves (e.g. cell01_0000.ibw – cell01_0019.ibw) collected into its own folder on the hard drive.

ii) Run:

```
s = make_line (fdir, cell_indices, coll_indices, cell_top, cell_bot, coll_lev)
```

with fdir the directory containing the 20 curves from your cell, cell_indices should be a vector containing a comma-separated list of the numbers 0-19 of the curves with just the cell, coll_indices should be a vector containing a comma-separated list of the numbers 0-19 of the curves with just the collagen, cell_top the relative position in micrometers of the cell apical surface, cell_bot the relative position in micrometers of the cell basal surface, and coll_lev the relative position in micrometers of the collagen surface. This will create the data structure s containing the ForceCurve objects (s.curves), the path to the directory (s.dir), the curve numbers over the cell (s.cell_indices) and collagen (s.coll_indices), and the z positions of the surfaces (s.cell_top, s.cell_bot, s.coll_lev).

iii) Open the file analyze_line.m in the editor, and enter the correct values for the variables r, theta, nu, type, and max_ind. For LRCH tips, theta=pi/8 (radians). R is listed on the SEM images of each probe in Dropbox\Group\Big Tips.

iv) Then run:

```
[E_cells, E_colls, depth, height_diff_afm, height_diff_optics, height,
E_cell_twolayer] = analyze_line (s)
```

The output variables tell you the cell Young's modulus (E_cells), the Young's modulus of the pericellular collagen (E_colls), the cell protrusion height (height_diff_afm), (height_diff_optics), the cell height (height), and the substrate-corrected cell Young's modulus (E_cell_twolayer).

APPENDIX B

MICROARRAY DATA TABLES

Cell Type	Number of differentially expressed SLC genes
b7e vs g11e	72
b7c vs g11c	68
b7t vs g11t	74
b7et vs g11et	67
b7e vs b7c	5
b7e vs b7t	6
b7e vs b7et	15
g11e vs g11c	12
g11e vs g11t	7
g11e vs g11et	21
g11et vs g11c	25
g11et vs g11c	21
g11et vs g11t	31

Table B1: Numbers of Differentially Expressed SLC Genes

Gene	Cell types	Fold change	Corrected *p*-value
'SLC9A7'	b7e vs g11e	-2.2	3.3E-3
	b7c vs g11c	-2.1	4.0E-2
	b7t vs g11t	-2.2	1.8E-2
	b7et vs g11et	-1.5	9.4E-4
	b7e vs b7et	-1.4	6.5E-4
'SLC9A2'	b7e vs b7et	+1.3	3.1E-3

Table B2: Differential Expression of NHE Genes

Gene	Cell types	Fold change	Corrected *p*-value
'EZR'	b7c vs g11c	+1.4	1.6E-2
	b7t vs g11t	+1.5	1.6E-2
	b7et vs g11et	+1.7	9.3E-3
	b7e vs b7c	+1.3	1.4E-2
	b7e vs b7et	-1.5	7.6E-3
'MSN'	b7e vs g11e	+3.8	1.5E-2
	b7c vs g11c	+3.0	5.9E-3
	b7t vs g11t	+3.3	1.6E-2
	b7et vs g11et	+3.0	5.8E-3
'RDX'	b7e vs g11e	-1.5	3.8E-2
	b7c vs g11c	-1.3	4.6E-2
	b7t vs g11t	-1.4	1.9E-2
	b7et vs g11et	-1.8	7.3E-3
'RHOA'	b7e vs g11e	-2.3	1.4E-3
	b7c vs g11c	-2.3	3.0E-3
	b7t vs g11t	-2.3	8.2E-3
	b7et vs g11et	-2.3	3.6E-3
'RHOB'	b7e vs g11e	-1.8	1.3E-2
	b7c vs g11c	-1.7	3.5E-3
	b7t vs g11t	-2.0	3.8E-3
	b7et vs g11et	-1.3	3.1E-2

Table B3: Differential Expression of ERM-family ABPs, Rho, and Ras Genes

Gene	Cell types	Fold change	Corrected *p*-value
'SPTBN1'	b7e vs g11e	-2.9	3.7E-3
	b7t vs g11t	-1.6	2.4E-3
	b7et vs g11et	+1.8	1.0E-2
	b7e vs b7et	-1.9	9.5E-3
'FLNA'	b7e vs g11e	-1.3	3.2E-2
'FLNB'	b7e vs g11e	-2.0	1.0E-2
	b7e vs b7t	+1.4	2.9E-2
	b7e vs b7et	-1.3	8.0E-3
'DSTN'	b7c vs g11c	+1.6	3.5E-2
	b7t vs g11t	+1.4	2.3E-4
	b7et vs g11et	+2.1	9.0E-3
	g11et vs g11c	-1.5	2.0E-2
	g11et vs g11t	-1.6	1.3E-2

Table B4: Differential Expression of ABPs: Spectrin, Filamins, and Destrin.

Gene	Cell types	Fold change	Corrected *p*-value
'COMT'	b7t vs g11t	-1.5	1.4E-2
	b7t vs g11t	-1.5	2.2E-2
	b7et vs g11et	+1.5	8.0E-3
	b7e vs b7et	-1.6	2.2E-3
	g11e vs g11t	-1.5	4.1E-3
	g11e vs g11t	-1.3	3.6E-2
	g11et vs g11c	-1.5	4.5E-3
	g11et vs g11t	-1.8	2.2E-3
'TUBA1C'	b7e vs g11e	-1.6	6.7E-3
	b7t vs g11t	-1.9	1.4E-2

Table B5: Differential Expression of Genes Involved in Estrogen-dependent Microtubule Stabilization.

Gene	Cell types	Fold change	Corrected *p*-value
'PRKCA'	b7e vs g11e	-1.8	3.7E-3
	b7c vs g11c	-1.8	2.7E-3
	b7t vs g11t	-1.8	6.5E-4
	b7et vs g11et	-1.5	2.5E-3
	g11e vs g11et	+1.3	5.3E-3
	g11et vs g11e	-1.3	5.3E-3
'PRKCH'	b7e vs g11e	-1.4	5.6E-3
	g11e vs g11c	+1.4	2.4E-3
'PRKCI'	b7e vs g11e	-1.4	1.4E-2
'PRKCG'	b7t vs g11t	-1.5	4.5E-2
	b7et vs g11et	-1.5	4.5E-2
'PRKCZ'	b7et vs g11et	+1.4	1.1E-2
'PRKCQ'	g11et vs g11t	-1.3	1.1E-2

Table B6: Differential Expression of Protein Kinase C Isoforms.

Gene	Cell types	Fold change	Corrected *p*-value
'MAPK3'	b7e vs g11e	-2.6	7.6E-3
	b7c vs g11c	-2.5	3.7E-2
	b7t vs g11t	-3.3	4.5E-3
	b7et vs g11et	-2.1	5.3E-3
	g11e vs g11et	+1.6	1.1E-2
	g11et vs g11c	-1.6	1.1E-2
'NFKB2'	b7e vs g11e	-1.4	1.4E-3
'BCL2'	b7t vs g11t	-1.4	3.2E-2
'CDKN1A'	b7e vs g11e	-1.6	2.1E-2
	b7t vs g11t	-1.5	1.6E-2
	b7et vs g11et	+1.8	2.8E-3
	g11e vs g11et	+1.5	9.7E-3
	g11et vs g11c	-1.5	3.0E-3
	g11et vs g11t	-1.5	9.5E-3

Table B7: Differential Expression of Genes Implicated in PKC-α-signaling-based Tamoxifen Resistance.

Gene	Cell types	Fold change	Corrected *p*-value
'PAX2'	b7e vs g11e	+1.7	4.4E-3
	b7c vs g11c	+1.8	3.3E-3
	b7et vs g11et	+1.8	1.3E-2
'NCOA3'	b7e vs g11e	+1.5	1.5E-2
	b7c vs g11c	+1.7	2.6E-2
	b7t vs g11t	+1.5	3.1E-2
	b7et vs g11et	+1.8	6.7E-3
	b7et vs g11et	+1.4	2.9E-2
'ESR1'	b7e vs g11e	-1.5	7.5E-3
	b7t vs g11t	-1.3	2.5E-2
	b7et vs g11et	+1.5	1.0E-2
	g11e vs g11c	+1.3	3.5E-2
	g11et vs g11t	-1.4	6.8E-3
'ESR2'	b7e vs g11e	-2.1	8.2E-3
	b7t vs g11t	-2.7	3.4E-3
	b7et vs g11et	-1.8	1.4E-2

Table B8: Differential Expression of Genes Implicated in ER/EGFR-crosstalk-based Tamoxifen Resistance.